A STUDY OF HYDRODYNAMICS IN THE NORTHERN ARABIAN GULF

A Dissertation

by

DAPENG LI

Submitted to the Office of Graduate and Professional Studies of
Texas A&M University
in partial fulfillment of the requirements for the degree of

DOCTOR OF PHILOSOPHY

Chair of Committee,	Ayal Anis
Committee Members,	Karl Kaiser
	Hui Liu
	Juan J. Horrillo
Head of Department,	Shari Yvon-Lewis

August 2019

Major Subject: Oceanography

ABSTRACT

In this study, we characterize hydrodynamics induced by winds (winter Shamals), tides and baroclinic tides in the Northern Arabian Gulf (NAG) based on observational data.

Winter Shamals (strong, dry, northwesterly winds) are unique surface meteorological phenomena in the NAG. During the Shamal event of 24-26 March, 2013, surface wind stress was observed to increase from 0.01 to 0.11 N/m^2 and was followed by a decrease in relative humidity from 66.6 to 47.2 %. The increase in wind speed and decrease in humidity resulted in a six-fold increase in latent heat loss (from 27.9 to 182.9 W/m^2) at the air-sea interface. Such Shamal events were found to significantly enhance turbulent mixing, as exemplified by a fivefold increase in mean turbulence kinetic energy (TKE) dissipation rates from $2.3x10^{-7}$ to $1.2x10^{-6}$ W/kg, and an almost complete homogenization of the water temperature.

Small-scale (time < 24 h and horizontal length < 10 km) hydrodynamics are significantly influenced by tides in the NAG. During the deployment between 14-28 July, 2017, measurements in the near bottom layer (~1.5-6.5 meter above bottom) showed: (1) semi-diurnal upwelling and downwelling induced by tides, with a maximum vertical speed of ~10 mm/s; (2) positive vertical velocity gradients during the ebb tides, indicating horizontal convergence; (3) quarter-diurnal cycles in TKE dissipation rates, with inequalities between the daily two floods and two ebbs; (4) well-correlated relations between turbulent diffusivity and gradient Richardson number.

Interactions between barotropic tides, stratifications, and varying topography usually generate baroclinic tides. Measurements between 22-29 January, 2013 showed: (1) the maximum isopycnal displacement induced by baroclinic tides was 8 m, ~30 % of the overall water depth of 27 m; (2) the peak baroclinic tidal parameters (baroclinic velocity, pressure anomaly, horizontal kinetic energy, and horizontal energy flux) occurred near the surface and bottom; (3) vertical oscillations of stratified water within the entire water column; (4) most of the time the gradient Richardson number was less than 0.25, suggesting shear instability.

ACKNOWLEDGEMENTS

I would like to express my sincerest appreciations to my committee chair, Dr. Ayal Anis. Without his guidance and support, this work would not have been possible. Dr. Anis is not only my academic advisor but also my life coach. His responsibility and attitudes towards science and life deeply influence me. Words cannot convey how grateful I am to have him as my advisor. I would like to extend my sincere thanks to Mrs. Ruthy Anis. I would never forget all the delicious food you cooked. Thanks also go to my committee members, Dr. Karl Kaiser, Dr. Hui Liu, and Dr. Juan J. Horrillo for their warm encouragements and insightful suggestions.

I would also like to extend my thanks to my lab mates (Fahad Al Senafi, Tariq Al Rushaid, and Sergey Molodtsov). Their company makes my PhD life colorful. Sincere thanks also go to the Chinese squad (Shu Dai, Shanran Tang, and Saijin Zhang). Thanks for letting me become parts of your life. I would always remember all beautiful moments we shared together. I would also like to thank my close friends, Andrew McGuffin and Annie Tamalavage. Thanks for checking on me to make sure I smile every day.

In the end, I would like to express my deepest gratitude to my family. Thanks so much for your love, patience, care and support.

CONTRIBUTORS AND FUNDING SOURCES

Contributors

This study was guided by a dissertation committee including Dr. Ayal Anis [advisor], Dr. Karl Kaiser, and Dr. Hui Liu of the Department of Oceanography, and Dr. Juan J. Horrillo of the Department of Ocean Engineering.

The data used for the dissertation was shared by Dr. Ayal Anis and by Dr. Fahad Al Senafi of the Department of Marine Sciences, Kuwait University. The surface wind and wave measurements presented in Chapter 2 were provided by the Kuwait Meteorological Office. The codes for manipulating measured current velocity were provided by Dr. Ayal Anis.

All other work used for the dissertation was completed by the student independently.

Funding Sources

Graduate study was partially funded by Texas A&M University at Galveston (in the form of a graduate student “Boost” award), the Qatar Research National Foundation (project #7-660-1-124) and the Kuwait Foundation for Advancement of Sciences (project #P21644SE01).

TABLE OF CONTENTS

Page

LIST OF FIGURES

Page

LIST OF TABLES

Page

1. INTRODUCTION

1.1. Background information

The Arabian Gulf (AG) resides between the mainland of Iran and the Arabian Peninsula. It connects the Gulf of Oman through the Hormuz Strait. The AG is a semi-enclosed shallow marginal sea, with the mean water depth of 36 m (Chao et al., 1992). The bathymetry of the AG is asymmetric, with a wide and shallow sea in the south and a narrow and deep sea in the north (Thoppil and Hogan, 2010). Surrounded by the massive desert areas, the climate is arid in the AG. The precipitation rate is around 0.03-0.11 m/yr (Almazroui et al., 2012), less than one tenth of the evaporation rate of 1.3 m/yr (Privett, 1959). The evaporation induced freshwater loss was filled with the water inflow from the Gulf of Oman of the Indian Ocean via the Hormuz Strait (Reynolds, 1993). The limited water exchange with the Gulf of Oman (~321 km^3/yr, Reynolds, 1993) and high evaporation lead to hypersaline water, with salinity estimated to be 38.5 ‰ to 41 ‰ (Al-Muzaini and Jacob, 1996). Based on numerical simulation results, Chao et al. (1992) found cyclonic circulation patterns in the AG consisted of two components: one current that moves southeast in the southern AG near the Saudi Arabian coast; and one current that flows northwest in the northern AG next to Iran.

Strong northwest wind events, locally referred to as Shamals, often occur in the AG with a typical duration of 3-5 days (Aboobacker et al., 2011). During Shamal events, significant increases in surface wind speed and decreases in humidity have been observed (Al Senafi and Anis, 2015). The combinations of high wind speed and low

humidity are found to cause a net surface heat loss of more than 1000 W/m^2 (Thoppil and Hogan, 2010). Winter Shamals are often associated with dust storms. During 22-23 February 2010, Abdi Vishkaee et al. (2012) documented a Shamal induced dust storm event, which resulted in a horizontal visibility of less than 1 km in the northwest Iran. The significant wind and heat loss during winter Shamals are found to impact hydrodynamics in the AG. Based on the model results, Thoppil and Hogan (2010) reported: (1) enhanced convective mixing driven by Shamal induced surface heat loss; (2) a cooling of sea surface temperature up to 10 °C in the NAG. The increase in mixing intensity and decrease in temperature may impact local flora and fauna communities (Cavalcante et al., 2016).

Tides are an important dynamical process in the continental shelf sea, driving periodic surface oscillations and current movements (Steele et al., 2009), inducing turbulent mixing (Thorpe, 2007), and affecting sediment transports near the bottom (Scully and Friedrichs, 2007). They are generated by the combined forces of the Earth, the Moon, and the Sun (Pond and Pickard, 1983). The AG is an energetic tidal region, with tidal range larger than 1 m everywhere (Reynolds, 1993). Based on current velocity measurements in the western AG, John (1992) found tides to be primarily controlled by four tidal constituents (O1, K1, M2, and S2). In the NAG, our measurements showed that tidal ranges and currents could reach up to 1.7 m and 0.5 m/s, respectively, during spring tides. Given the importance of tides in the NAG, it is expected that tides are likely to impact both the hydrodynamics and the marine ecosystem.

Baroclinic tides (internal waves with tidal frequencies) are ubiquitous phenomena in the interior of the ocean (Steele et al., 2009). They typically occur in stratified water when barotropic tides proceed over varying topography (Rayson et al. 2011). Similar to barotropic tides which drive surface elevations, baroclinic tides can induce internal vertical oscillations. The isopycnal displacements due to baroclinic tides can be greater than 200 m in the continental shelf break (Steele et al., 2009). Such movements are found to affect the vertical distributions of chemical parameters in the ocean (Pai et al., 2016). Based on the significance of tides in the NAG, it is expected that baroclinic tides are likely to occur and affect hydrodynamics in that area. To the best of our knowledge, no published studies on baroclinic tides in that region have been found, which motivates us to explore these phenomena.

1.2. Research questions

Due to the lack of comprehensive oceanographic measurements, hydrodynamics induced by winds (winter Shamals), tides and baroclinic tides in the NAG still remain unclear. Here, we will specifically look into answering the following main questions:

1) How does the NAG physically respond to winter Shamals? Are the effects of winter Shamals only limited to the surface or present within the entire water column?
2) In the NAG, what are the roles of tides on the hydrodynamics, in particular, turbulent mixing near the bottom? How do tidal currents and mixing vary during the neap-spring cycles?

3) Do baroclinic tides exist in the NAG? If so, what are the dynamical features of them?

1.3. Outline of the dissertation

This dissertation consists of five chapters. Chapter 2, titled "Physical response of the NAG to winter Shamals", addresses the first question raised in section 1.2 based on observational data. During the field deployment between 19 January to 19 April, 2013, a total of four winter Shamals were encountered, affecting hydrodynamics in the NAG. In the results section, we examine the variabilities of surface wave, current velocity, turbulent mixing and thermal structure during one particular strong Shamal event on 24-26 March, 2013. In the discussion and conclusions section, we summarize the statistics of all four winter Shamals and discuss the possible implications of winter Shamals on the marine ecosystem.

Chapter 3, titled "Neap-spring variability of tidal dynamics in the NAG", addresses the second research question in section 1.2 using field measurements. In the results section, we characterize the variabilities of current velocity and turbulent mixing during the neap-spring cycle of 14-28 July, 2017. In the discussion and conclusions section, we examine (1) the relation between turbulent diffusivity and gradient Richardson number; (2) the energy budget of tidal power inputs and local turbulent dissipation.

Chapter 4, titled "Observation of baroclinic tides in the NAG", addresses the third research question in section 1.2 based on the field deployment from 19 January to 19 April, 2013. In the results section, we present comprehensive observational results of

one-week (22-29 January, 2013) as a representative of baroclinic tides in the NAG. In the discussion and conclusions section, we summarize the analysis results of three-month current velocity measurements and discuss the potential impacts of baroclinic tides on marine ecosystem.

Chapter 5 summarizes the major findings of each chapter.

2. PHYSICAL RESPONSE OF THE NORTHERN ARABIAN GULF TO WINTER SHAMALS

2.1. Introduction

The Arabian Gulf (AG), covering a geographic region between 24° N to 31° N and 48° E to 57° E, is an extensive shallow marginal sea branching off the Arabian Sea via the Hormuz Strait. The estimated surface area and volume of the AG are approximately 239,000 km^2 and 8630 km^3 with average and maximum water depths of 36 m and 100 m, respectively (Chao et al., 1992). Located in the subtropical high pressure regions, the climate in the AG is characterized as hot and arid. The excess of evaporation (1.44 m/yr, Privett, 1959) over precipitation (0.11-0.19 m/yr, Marcella and Eltahir, 2008) leads to formation of hypersaline water (Nezlin et al., 2010) with salinity ranging from 38.5 ‰ to 41 ‰ (Al-Muzaini and Jacob, 1996). For horizontal length scales of ~10 km, the hydrodynamics in the AG are significantly influenced by tides (Azizpour et al., 2016). Using our 3-months field measurements as an example, harmonic analysis shows that tides account for 86 % of surface elevation energy and 97 % of total current energy. Basin-scale circulation is reported to be composed of two elements: (1) a current that proceeds southeast along the Saudi Arabian coast (Zhao and Ghedira, 2014), and (2) a northwest current that flows along the Iranian coast from the Strait of Hormuz (Chao et al., 1992). The water exchange between the AG and the Indian Ocean occurs through the Strait of Hormuz. The estimated inflow and outflow rates are 2696 km^3/yr and 2375 km^3/yr (Reynolds, 1993), resulting in a residence time of 3-5 years (Al-Muzaini and

Jacob, 1996). Given the limited water exchange through the Hormuz Strait and numerous oil and gas drilling stations, marine hazards such as oil and chemical spills, as well as algal blooms have been frequently reported across the AG (Moradi and Kabiri, 2012; Richlen et al., 2010). For example, a disastrous red tide event in 2008 posed severe threats to shorelines, fishery, coral reef community and fresh water supply (Zhao et al., 2015). As such, the AG is likely to be a sensitive and vulnerable ecosystem to both anthropgenic and significant natural events such as Shamals.

A unique, but not uncommon, meteorological phenomena in the AG are Shamals (Rao et al., 2003; Vinod Kumar et al., 2014). Shamals are strong northwest wind events which can last up to 3-5 days (Aboobacker et al., 2011). Based on a study that analyzed 40 years surface meteorological measurements in the Northern AG (NAG), Al Senafi and Anis (2015) found the average occurrence of Shamals are 10 events per year, with an increasing frequency of 1.63 Shamal days per year from 1973 to 2012. The winter Shamals are usually associated with the passage of cold fronts over the AG (Aboobacker et al., 2011), with typical wind speeds from 15-20 m/s (Thoppil and Hogan, 2010). Perhaps the most unique feature of winter Shamals is the extremely low humidities associated with them due to their travel over arid areas before reaching the AG. Combined with high wind speeds, winter Shamals can intensify evaporation and thus result in significant net heat loss (up to 1000 W/m^2) at the air-sea interface (Thoppil and Hogan, 2010). Severe dust storm events are frequently associated with winter Shamals, as exemplified by desert dust transport over Iraq and Iran shortly after a Shamal event between 22-23 February, 2010 (Abdi Vishkaee et al., 2012). During that event, the

average visibility dropped sharply to 1 km and lasted for 1-2 days (Abdi Vishkaee et al., 2012).

The substantial change in surface meteorological conditions driven by Shamals is expected to affect the hydrodynamics in the AG: El-Sabh and Mutry (1989) developed a two-dimensional model and found that sea level changes induced by Shamal systems may reach up to several meters. Utilizing the Hybrid Coordinate Ocean Model, Thoppil and Hogan (2010) found that winter Shamal events generated a northwest current of 0.25-0.3 m/s near the coast of Iran and affected water transport through the Hormuz Strait. In addition, significant surface heat loss induced by these strong wind events resulted in a decrease in sea surface temperature (SST) of up to 10 ºC (Thoppil and Hogan, 2010). In summer, Shamal-induced large scale eddies with a diameter of 52 km were simulated from the off-shore islands of Iran to the shoreline of the United Arab Emirates, leading to possible instability of the circulation in the AG (Cavalcante et al., 2016).

Due to limited availability of observations, previous studies relied on numerical model simulations of the AG's response to Shamal forcing (Cavalcante et al., 2016; El-Sabh and Mutry, 1989; Thoppil and Hogan, 2010). At this time observational based studies are still scarce, and the work reported here is a first attempt to characterize the NAG's physical response to winter Shamals using field measurements. Results of this work should offer an improved understanding of both the temporal and vertical variabilities of hydrodynamics (current velocities, thermal structure, and turbulent mixing) driven by severe meteorological events, such as Shamals. This paper is

structured as follows: data and methods are presented in section 2.2 and 2.3, results are described in section 2.4 followed by discussion and conclusions in section 2.5.

2.2. Data

2.2.1. Surface meteorological data

Surface meteorological parameters were collected from a station located on a pier at Qarooh Island (28º 82' N, 48º 78' E; red triangle in Figure 2.1), off the coast of Kuwait, from 19 January to 19 April, 2013. The nominal height of the meteorological sensors was approximately 7 m above mean sea level. Measured parameters included wind speed and direction (Young marine wind sensor model 05106), air temperature and relative humidity (Onset temperature/relative humidity smart sensor model S-THB-M002), barometric pressure (Onset barometric pressure smart sensor model S-BPB-CM50), rain rate (Texas Electronics tipping bucket model TE 525), incoming long-wave radiation (Kipp & Zonen pyrgeometer model CG3), and incoming short-wave radiation (Apogee pyranometer model PYR-PA). Surface meteorological parameters were measured at 2-minute intervals and then averaged and logged every 10 minutes. Unfortunately, due to faulty logger hardware, air temperature and relative humidity data were not recorded until March 03, 2013 and winds were not recorded throughout the whole experiment. These data gaps were filled by observations from the Kuwait Meteorological Office (KMO) Qarooh station located at a distance of ~10 m away from our own meteorological station. The observed wind (Vaisala wind sensor model WS425), air temperature/relative humidity (Vaisala humidity and temperature probes model

HMP45A & HMP45D) provided by the KMO were measured at 1-minute intervals and then averaged and logged every 10 minutes.

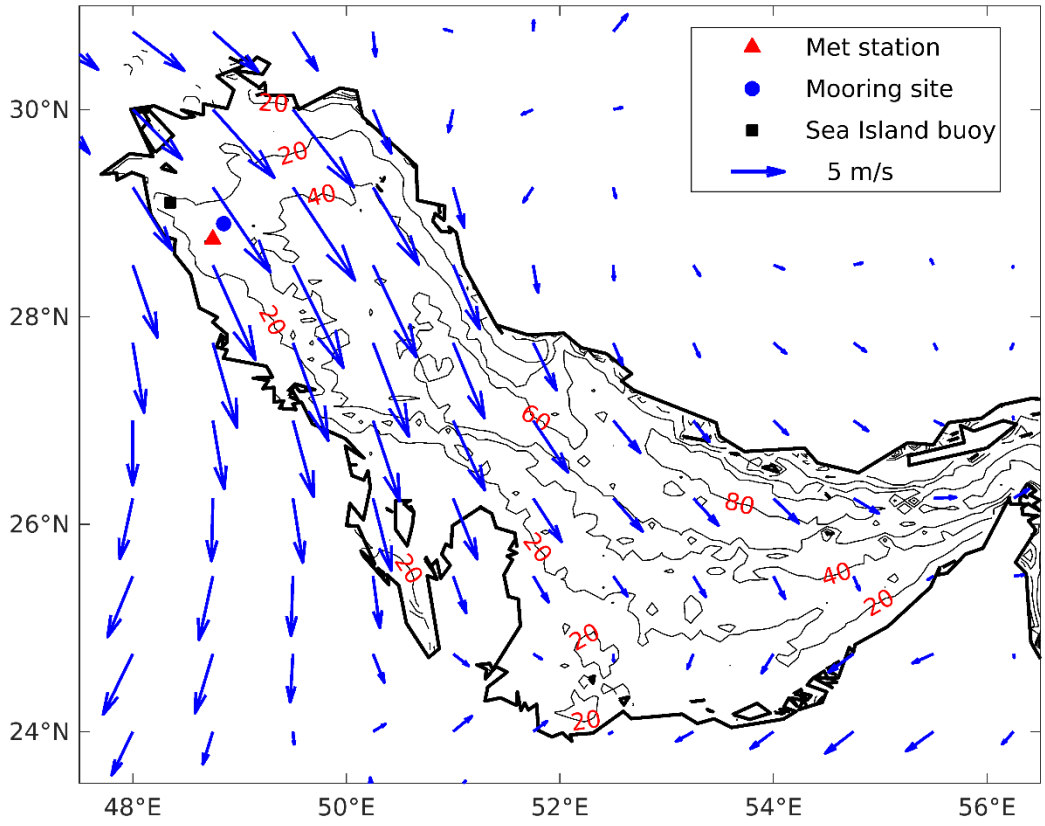

Figure 2.1 Geographic locations of the meteorological station (red triangle), mooring deployment site (blue circle), and the KMO Sea Island buoy (black square). Depth contours (thin black lines at 20 m depth intervals) of the AG and surface winds (blue arrows) during the first steady Shamal wind period on 25 March, 2013 at hour 0000 UTC are shown as well. Wind data was acquired from the European Center for Medium-Range Weather Forecasts (ECMWF).

Surface wind stress and individual heat flux components were computed from the observed surface meteorological data sets using the Coupled Ocean–Atmosphere Response Experiment (COARE) algorithms (Fairall et al., 2003). The net surface heat flux, J_q^0, was calculated by summing the four heat flux components:

$$J_q^0 = J_q^{SW} + J_q^{LW} + J_q^L + J_q^S$$

where J_q^{SW} is the net short-wave radiation corrected for albedo, J_q^{LW} is the net long-wave radiation, J_q^L is the latent heat flux, and J_q^S is the sensible heat flux (Anis and Singhal, 2006). Sign convention is positive for upward heat flux (out of the sea).

2.2.2. Mooring data

Hydrodynamical parameters were collected from an instrumented tight mooring deployed approximately 2 nautical miles northeast of Qarooh Island (28º 51' N, 48º 48' E, nominal water depth 27m; blue circle in Figure 2.1). Instruments on the mooring included two Conductivity, Temperature, Depth (CTD; RBRconcerto) sensors, an acoustic Doppler velocimeter (ADV; Nortek Vector), twenty four thermistors (Onset HOBO water temperature Pro v2 data logger), and a bottom-mounted upward looking acoustic Doppler current profiler (ADCP; Nortek 1 MHz Aquadopp). The “eyes” of the ADCP were 0.3 meters above bottom (MAB) and the blanking distance of the ADCP was 0.2 m. Instruments and their sampling details are summarized in Table 2.1.

Table 2.1 Meters above bottom (MAB), measured parameters, and sampling intervals of the instruments. Nominal water depth at the mooring site was 27 m.

MAB	Instruments	Measured parameter	Sampling interval (s)
8, 21	CTD	*C, T, P*	20
[0.1-22.4][a]	Thermistor	*T*	200
18	ADV	*V, P*	210
0.3	ADCP	*V, P*	180

T is temperature, *C* is conductivity, *P* is pressure, and *V* is velocity.

[a] 24 thermistors span 0.1 to 22.4 MAB with mean vertical separations of ~1 m.

The ADV beam velocities were recorded in bursts of 512 data points with a sampling frequency of 16 Hz. Bursts intervals were 210 s. Two data quality controls were applied to ADV beam velocities before data analysis: (1) velocities were rejected if signal correlation was less than 50 %, or signal-to-noise ratio was less than 4 db (Lien and D'asaro, 2006; Sato et al., 2014); (2) velocity spikes were identified using the Generalized Extreme Studentized Deviate outliers function (Rosner, 1983) and replaced using the Expectation Maximization algorithm (Schneider, 2001). The processed beam velocities of the ADV were then converted to earth (ENU) coordinate velocities. ADCP velocity profiles were recorded in earth coordinates and each profile contained 40 vertical bins with a bin size of 0.5 m. Each velocity profile was an average over 36 s with profile intervals of 180 s.

Given the significance of tides in the NAG, here we used residual surface elevations and currents to study the Shamal induced hydrodynamics. The residual surface elevation (current) is defined as the difference between measured and tidal surface elevations (currents). Residual currents were then rotated to along-shore and cross-shore directions. The positive along-shore velocity (v) was defined as 25º west of north and the positive cross-shore velocity (u) was defined as 25º north of east.

2.2.3. Ancillary data

Surface wave heights and periods were provided by the KMO from marine station Sea Island buoy (29º 7' N, 48º 18' E, black square in Figure 2.1). The nominal water depth at the Sea Island buoy location was 31 m. Surface waves were recorded by a bottom-mounted, upward looking, acoustic wave and current profiler (AWAC; Nortek 600 Khz). The center "eye" of the AWAC was 0.5 MAB. For the wave measurements, burst sampling was used with an interval of 1 hour. Each burst contained 1024 measurements sampled at 1 Hz. Surface wave heights and periods were computed from the power spectra of both the pressure and the acoustic surface tracking by the vertical (center) beam. In addition, to characterize the spatial pattern of Shamal winds, surface wind velocities for the entire AG were acquired from the European Center for Medium-Range Weather Forecasts (ECMWF) and are presented in Figure 2.1. The time chosen is 25 March, 2013 at hour 0000 UTC, the time when the strong and steady Shamal winds occurred. The spatial resolution of ECMWF wind data is 0.75º x 0.75º.

2.3. Methods

2.3.1. Shamal definition

In this study, we follow the definition of Shamal events given in Al Senafi and Anis (2015): a single Shamal event consist of at least two consecutive Shamal days, with each Shamal day defined as a day when WNW-N winds blow for more than three hours a day with hourly mean wind speeds not less than 9.85 m/s. Shamal-free days refer to the two days before (Pre-Shamal) and after (Post-Shamal) Shamal events. Based on this definition, a total of four winter Shamals were encountered during our field experiment. In the results section (section 2.4), we present detailed observations during Shamal #4 (24-26 March, 2013), when the largest increase in surface wind stress and latent heat flux occurred. Statistics of all four winter Shamals are summarized in the discussion and conclusions section (see section 2.5).

2.3.2. Turbulence kinetic energy dissipation rates

Turbulence kinetic energy (TKE) dissipation rates, ϵ, were estimated from the ADV velocity spectra computed from the ADV's vertical velocity due to it's lower noise level (by a factor of ~10) compared to the horizontal velocities. Since the ADV was moored, mooring motions and/or surface waves may possibly contaminate the velocity spectra (e.g. Sato et al., 2014; Trowbridge and Elgar, 2001). The ADV was moored in the vertical (z) direction. Pitch and roll angles recorded the rotation around the horizontal (x and y) axes. Here we used the standard deviation of the ADV's pitch and roll to quantify their variability around the horizontal axes. During all four winter Shamals, only a very

slight increase (less than 2º) was observed from the standard deviation of ADV's burst measurements of pitch and roll (Figure 2.2). In order to use velocity data uncontaminated by mooring motions, we first examined the slope of the velocity spectra within the inertial frequency subrange. The spectra of homogeneous and isotropic turbulence at sufficiently high Reynolds numbers and in statistical equilibrium is predicted to follow a -5/3 slope in the inertial subrange (Kolmogorov, 1968). We followed Sato et al (2014), who accepted velocity spectra if the slope within the inertial frequency subrange (0.2-1.0 Hz in their case) was within ±36 % of -5/3 (-2.27, -1.07), but limit our acceptance of spectra slope within the inertial frequency subrange (0.8-2 Hz) to ±30 % of -5/3 (-2.17, -1.17). We then visually examined individual spectra to further ensure quality before calculating ϵ. To account for wave effects, the kinematic model proposed by Trowbridge and Elgar (2001) was employed to estimate ϵ from the spectra:

$$P_{ww}(\omega) = \frac{12}{55}\alpha\epsilon^{\frac{2}{3}}V^{\frac{2}{3}}\omega^{-\frac{5}{3}}I(\frac{\sigma}{V},\theta)$$

$$I(\frac{\sigma}{V},\theta) = \frac{1}{\sqrt{2\pi}}(\frac{\sigma}{V})^{\frac{2}{3}}\int_{-\infty}^{+\infty}(x^2 - 2\frac{V}{\sigma}\cos(\theta)\,x + \frac{V^2}{\sigma^2})^{\frac{1}{3}}e^{-\frac{x^2}{2}}dx$$

where $P_{ww}(\omega)$ is the two-sided power spectral density of the vertical velocity component, ω is the angular frequency, V is the magnitude of the current velocity, α is the Kolmogorov constant taken as 1.5, σ is the standard deviation of the horizontal velocities, θ is the angle between current and wave directions, and x is an integration variable. Before and after winter Shamals, most of the ϵ were below the ADV noise level which allows to resolve ϵ if above 10^{-7} W/kg. To prevent overestimation of mean ϵ

before, during, and after the Shamal event, a background (constant) value of 10^{-10} W/kg (e.g. Anis and Singal, 2006) was used to fill in ϵ below the noise level.

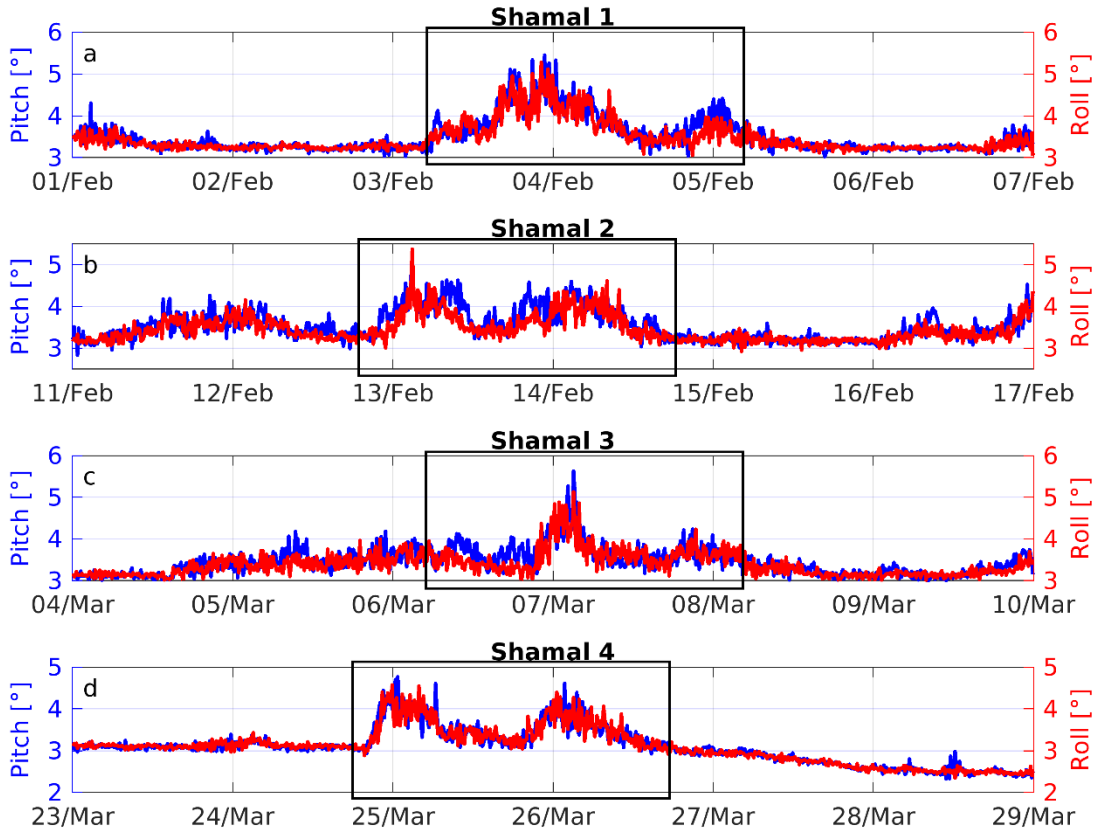

Figure 2.2 Standard deviation of ADV's burst measurements of pitch (blue) and roll (red) during four winter Shamals. Pitch and roll were measured by ADV each burst with a sampling frequency of 1 Hz. The boxes mark the occurrence of winter Shamal events.

2.3.3. Power inputs from wind and surface buoyancy flux

The power input from wind, P_w, was estimated as:

$$P_w = \tau U_s$$

where τ is the surface wind stress, computed using COARE algorithms (Fairall et al., 2003), and U_s is the surface drift current (Thorpe, 2007). In this study, the surface drift current, which consists of both wind-driven and wave-driven currents (Cheng and Mitsuyasu, 1992), is estimated to be 3.1 % of the surface wind speed (Wu, 1983).

The power input from surface buoyancy flux, P_b, was calculated as:

$$P_b = \frac{g\alpha_t h J_q^0}{C_p}$$

where g is the gravitational acceleration, α_t is the thermal expansion coefficient for water, h is the water depth, J_q^0 is the net surface heat flux, and C_p is the specific heat capacity of sea water (Huang and Jin, 2006). Note that the power from surface buoyancy flux only contributes to mixing during convective conditions, i.e. when surface buoyancy flux is positive, resulting mainly from surface heat loss.

2.3.4. The gradient Richardson number

The gradient Richardson number, Ri, used below to estimate the relative importance of mechanical and density effects in the water column, was computed as (e.g. Thorpe, 2007):

$$Ri = \frac{N^2}{S^2}$$

$$N^2 = -\frac{g}{\rho_w}\frac{d\rho_w(z)}{dz}$$

$$S^2 = (\frac{\partial U}{\partial z})^2 + (\frac{\partial V}{\partial z})^2$$

where N^2 is the buoyancy frequency squared, S^2 is the velocity shear squared, ρ_w is the local mean density of seawater, $\rho_w(z)$ is the density of seawater as a function of depth, z is the vertical coordinate (positive up), and U and V are the E-W and N-S velocities, respectively, measured by the ADCP. For steady, two-dimensional, inviscid, non-diffusive, horizontal flow, instability can occur only if the gradient Richardson number is smaller than 0.25 in the flow (Thorpe, 2007). Thus, here we compared the measured Ri to 0.25 in the data analysis (see section 2.4.4).

A gradual decrease in salinity measured by the two CTDs was noticed after the first week of deployment, most likely resulting from biofouling. During this week the mean vertical differences of temperature and salinity measured by the CTDs were 1.08 °C and 0.09 PSU, respectively, suggesting that temperature was the main contributor to the density and thus to stratification. Thus, a constant salinity value of 42 PSU was used in our study period (23-29 March, 2013). The use of constant salinity may have introduced an error no larger than 0.01% in the density and an error of ~19 % in the buoyancy frequency squared estimates. Furthermore, the error introduced by using a constant salinity value is expected to be smaller during winter Shamals when complete mixing throughout the water column was observed (see section 2.4.4).

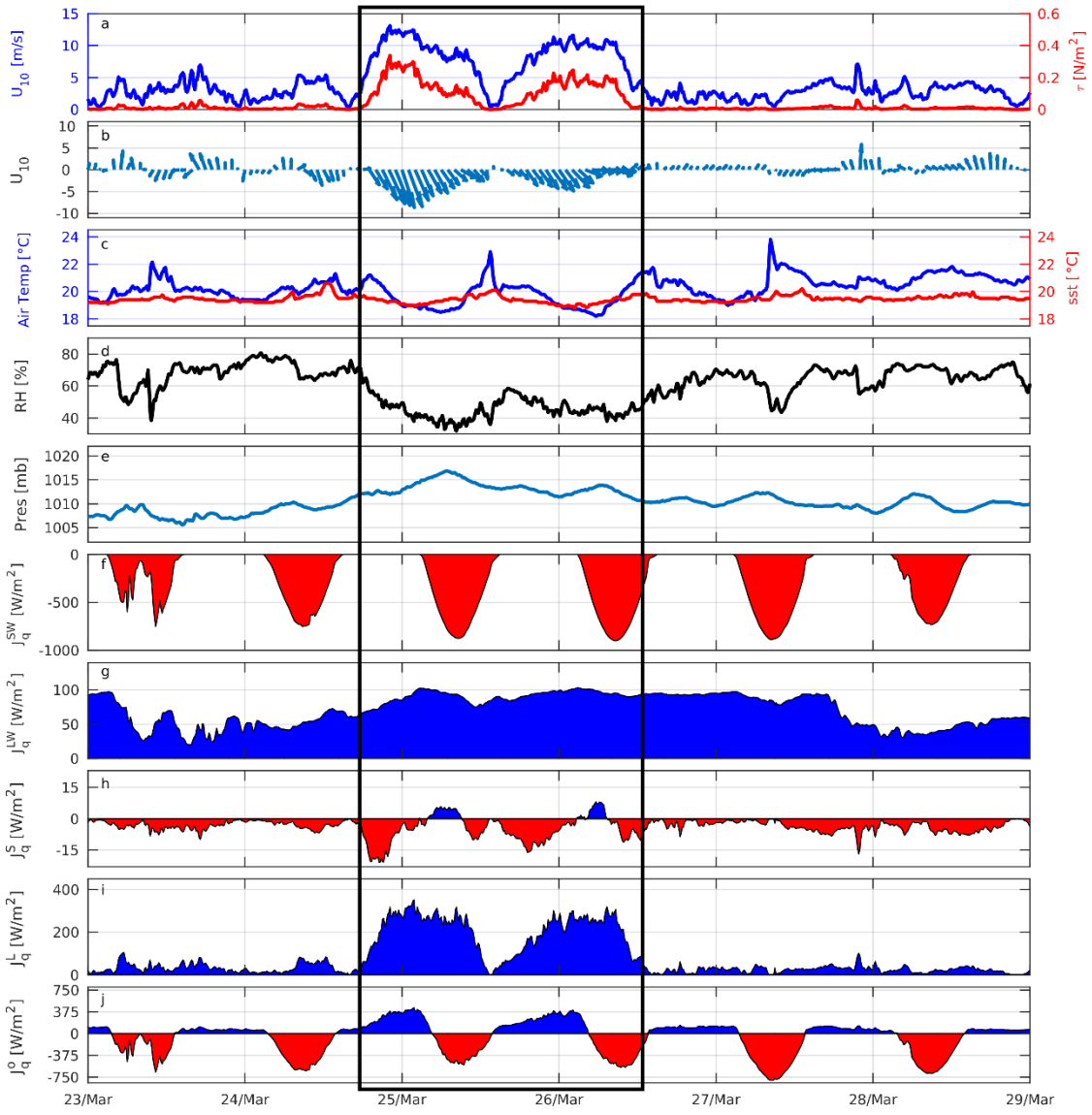

Figure 2.3 Surface meteorological parameters from 23-29 March, 2013, top to bottom: (a) wind speed at 10 m above sea level (blue) and wind stress (red), (b) wind vectors at one-hour intervals, (c) air temperature (blue) and sea surface temperature (red), (d) relative humidity, (e) barometric pressure, (f) short-wave radiation, (g) long-wave radiation, (h) sensible heat flux, (i) latent heat flux, (j) net heat flux. In (f)–(j), sign convention is positive (negative) for upward (downward) heat flux (see section 2.2.1); blue and red shaded areas represent cooling and heating of the water column. The box marks the Shamal event of 24-26 March, 2013.

2.4. Results

2.4.1. Surface meteorological conditions

The Shamal event included two separate strong northwest wind periods (Figure 2.3 a). The first steady Shamal wind period, with mean wind speed and stress of 11.8 m/s and 0.26 N/m^2, respectively, occurred between hour 2100, 24 March, and hour 0300, 25 March (UTC). Winds gradually decreased during the daytime of 25 March and reached their second steady peak between hour 2200, 25 March, and hour 0800, 26 March. The mean wind speed and stress during the second steady Shamal wind period were 10.2 m/s and 0.18 N/m^2. Wind directions during the Shamal were dominantly northwest while variable wind directions were observed during the Shamal-free periods (Figure 2.3 b). Both air temperature and SST displayed clear diurnal cycles, increasing during daytime due to heating by incoming short-wave radiation and decreasing at night due to net heat loss from the surface. The ranges of air temperature and SST were 18.2-23.8 °C and 18.8-20.6 °C, respectively. During the Shamal, the mean relative humidity decreased from 66.6 to 47.2 % (Figure 2.3 d). The barometric pressure reached two peaks of 1017 and 1014 mb, corresponding to the two peaks in wind speed (Figure 2.3 e). The net short-wave radiation followed the diurnal cycle, reaching a maximum of 900 W/m^2 at noon, 26 March (Figure 2.3 f). Latent heat flux and long-wave radiation contributed the largest heat loss terms throughout the experiment (Figure 2.3 g, i) with the latent heat flux also exhibiting the largest variability compared to the other heat flux components throughout the Shamal. The increase in wind speed and decrease in humidity resulted in a significant latent heat loss of 182.9 W/m^2, compared to 27.9 W/m^2 during Shamal-free

conditions. Sensible heat flux contributed the least to the overall heat flux, varying from -20.9 to 8.1 W/m^2 (Figure 2.3 h). The largest net heat loss of 442 W/m^2 was observed during the first steady Shamal wind period on 25 March (Figure 2.3 j).

2.4.2. Surface waves, surface elevation, and current velocities

Wave periods ranged from 1.3 to 4.7 s between 23–29 March, implying that wind waves were dominant in the NAG during this time (Figure 2.4). During the night of 24–25 March, both wave height and period reached a maximum of 1.2 m and 4.7 s corresponding to the first steady Shamal winds. As the second steady Shamal winds set in during the night of 25-26 March, wave height and period reached their second peak of 0.8 m and 4.3 s, respectively. After the passage of the Shamal, the wave height and period decreased to ~0.4 m and ~2.7 s.

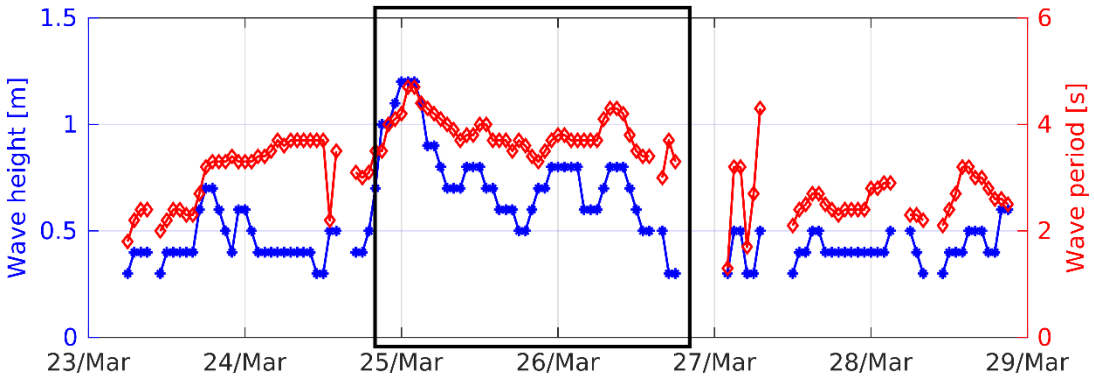

Figure 2.4 Surface wave heights (blue) and wave periods (red) from 23-29 March, 2013. The box marks the Shamal event of 24-26 March, 2013.

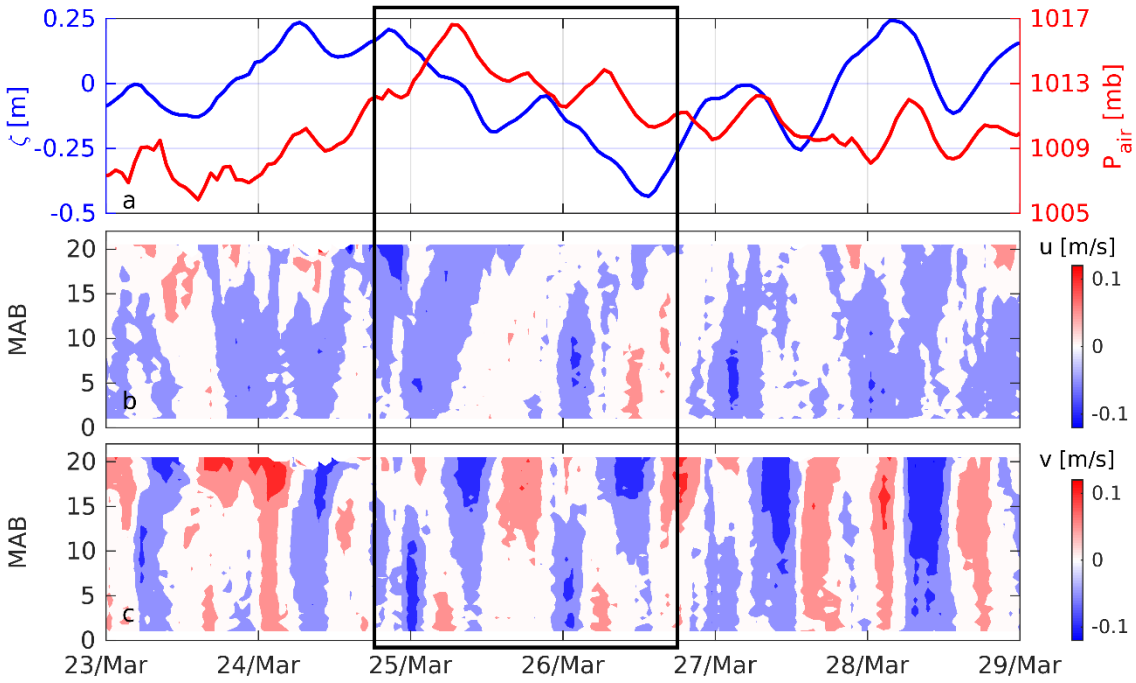

Figure 2.5 (a) residual surface elevation (blue) and barometric pressure (red), (b) cross-shore residual currents, (c) along-shore residual currents. The box marks the Shamal event of 24-26 March, 2013.

The increase in barometric pressure associated with the passage of the Shamal was followed by a gradual decrease in the residual surface elevation from +0.2 to -0.4 m (Figure 2.5 a; see definition in section 2.2.2). Residual current velocities ranged from -0.1 to +0.1 m/s between 23–29 March (Figure 2.5 b, c). Along-shore residual velocities show higher amplitudes and variabilities than the cross-shore component, indicating that the general flow was mainly oriented along the bathymetry, parallel to the shore. The Shamal affected both the cross and along shore velocity structures. In the cross-shore direction (Figure 2.6 a), offshore currents were observed from 10 to 20.5 MAB during

the Pre-Shamal period. The maximum offshore current speed was ~0.03 m/s at 20.5 MAB. During the Shamal, onshore currents were observed between 15.5 to 20.5 MAB. Partial recovery of the velocity structure to Pre-Shamal conditions was observed after the Shamal event, with offshore currents between 12 to 20.5 MAB. In the along-shore direction (Figure 2.6 b), northwest (positive along-shore) currents were observed from 1 to 20.5 MAB during the Pre-Shamal period. Current speed gradually increased from the bottom to 20.5 MAB. During the Shamal event, a decrease in northwest currents was observed within the water column. The maximum decrease of 0.05 m/s occurred at 20.5 MAB. After the Shamal event, partial recovery of the velocity structure to Pre-Shamal conditions was observed with northwest currents increasing in velocity between 6 to 20.5 MAB.

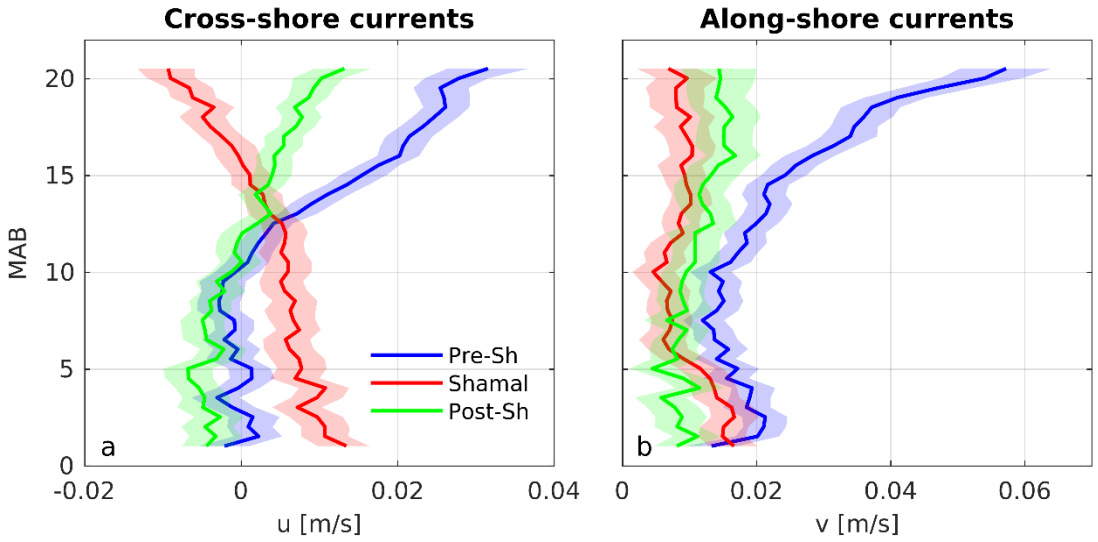

Figure 2.6 Vertical profiles of (a) residual cross-shore currents and (b) residual along-shore currents averaged over Pre-Shamal, Shamal, and Post-Shamal periods. Shaded area denotes the 95 % bootstrap confidence intervals.

2.4.3. Surface power inputs and thermal structure

Two peaks in P_w and P_b were observed corresponding to the two Shamal wind periods (Figure 2.3 a, Figure 2.7 a). Throughout the Shamal event, the increase in wind speed resulted in a substantial increase in P_w from 1.0×10^{-3} to 3.5×10^{-2} W/m^2. The mean P_b increased from 1.4×10^{-3} to 3.9×10^{-3} W/m^2, resulting from the increase in heat loss at the surface driven by the Shamal winds. During the Shamal event, the wind contribution to the energy available for mixing was about one order of magnitude larger compared to the contribution from the surface buoyancy flux.

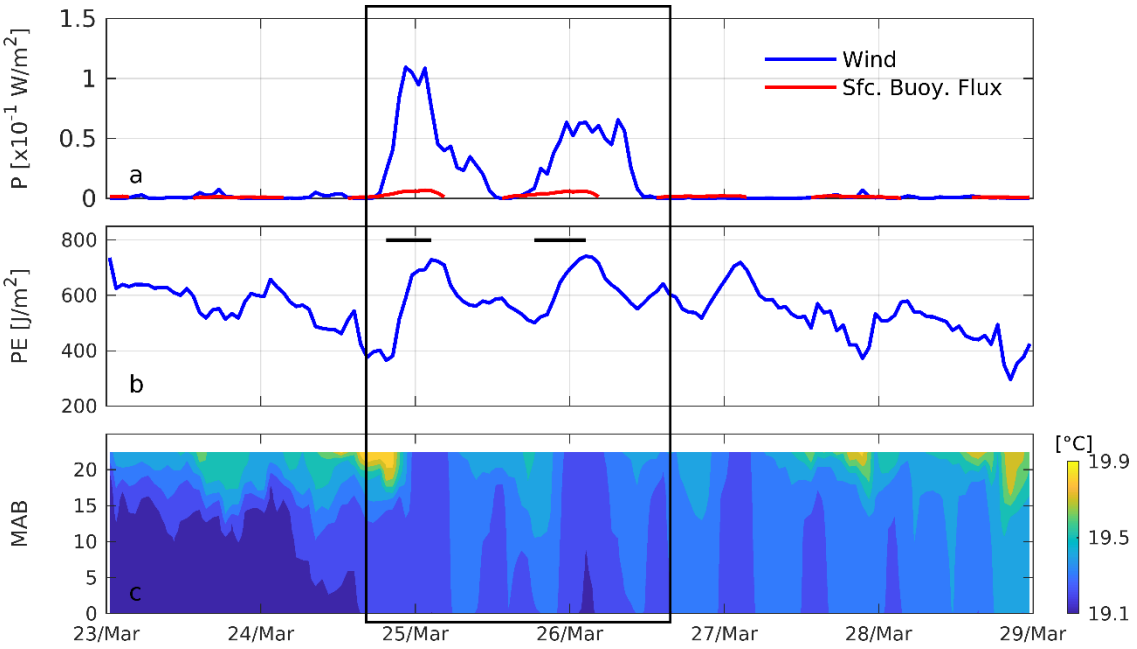

Figure 2.7 (a) Power inputs from wind and surface buoyancy flux, (b) potential energy (PE) of the whole water column, (c) water temperature. In (a), we only presented power inputs from surface buoyancy flux during convections, which were resulting mainly from surface heat loss (see section 2.3.3). The two horizontal black lines in (b) denote the increases in PE during the two Shamal wind periods. To compute the PE of the whole water column, we chose the bottom as the level of zero PE. Since only the changes in PE are of interest, we subtracted a constant value of 3.7×10^6 J/m^2 from the PE to show the variability. The box marks the Shamal event of 24-26 March, 2013.

The potential energy ($\mathrm{PE} = \int_0^h \rho_w(z) g z dz$) of the whole water column was observed to increase during the two Shamal wind periods (Figure 2.7 b). During the first Shamal wind period (denoted by the first horizontal black line in Figure 2.7 b), the PE increased by 364 J/m^2. The wind energy input was 2132 J/m^2 during that period. According to Hsu et al. (1982), 29 % of the wind energy is expected to be absorbed by wind waves. Here,

the remaining wind energy (1514 J/m^2) was larger than the observed increase in PE (364 J/m^2), suggesting that Shamal winds may possibly account for this increase in PE. During the second Shamal wind period (denoted by the second horizontal black line in Figure 2.7 b), the wind energy input, after accounting for the loss to waves, was 885 J/m^2, almost four times the observed increase in PE of 240 J/m^2, i.e. similar to the ratio during the first Shamal wind period.

Water temperature ranged from 19.1 to 19.9 ^{o}C during the study period (Figure 2.7 c). During the Pre-Shamal periods, the mean vertical temperature difference was ~0.4 ^{o}C between the upper and lower parts of the water column (Figure 2.8 a). Cooling was observed in the upper water column (~17-22 MAB) during the Shamal, with a maximum temperature decrease of ~0.2 ^{o}C at 22 MAB (Figure 2.8 a). Two complete homogenizations of water temperature were observed corresponding to the two steady Shamal wind periods (Figure 2.7 c). Shortly after the passage of the Shamal, during the early morning of 27 March (Figure 2.7 c), the vertical temperature profile was still homogeneous likely the result of favorable convective conditions at that time. Recovery of the thermal structure to Pre-Shamal conditions occurred later during the daytime of 27 March. Average over the Post-Shamal period show a vertical temperature difference of ~0.2 ^{o}C between the upper and lower parts of the water column (Figure 2.8 a).

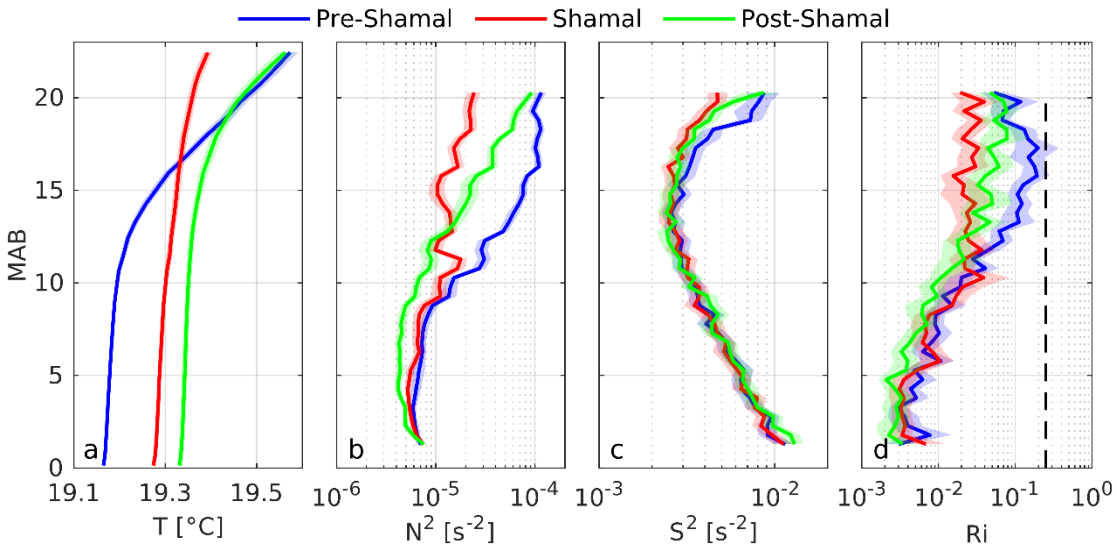

Figure 2.8 Vertical profiles of (a) water temperature, (b) buoyancy frequency squared, (c) velocity shear squared, and (d) the gradient Richardson number, averaged over Pre-Shamal, Shamal and Post-Shamal periods. The broken black line in (d) denotes the gradient Richardson number of 0.25. Shaded area denotes the 95 % bootstrap confidence intervals.

2.4.4. Turbulent mixing

During the Pre-Shamal periods, the water-column was stratified mainly in the upper half (10 to 20.5 MAB) with N^2 ranging between 10^{-5} to 10^{-4} s^{-2} while in the lower half N^2 was lower by an order of magnitude (~10^{-6} s^{-2}, Figure 2.8 b, Figure 2.9 a). Vertical shear of horizontal velocity was higher in the bottom boundary layer (within ~5 MAB) with S^2 values on the order of 10^{-2} s^{-2}, decreasing to 10^{-3} s^{-2} in the upper water column (Figure 2.9 b). The minimum occurred at mid-depth (~14 MAB; Figure 2.8 c). Stable conditions, with Ri values greater than 0.25, were observed at several instances in the upper water column (Figure 2.9 c). Although relatively calm surface meteorological

conditions dominated the Pre-Shamal period (Figure 2.3), the mean Ri was less than 0.25 in most of the water column (Figure 2.9 c), suggesting that the water column was already pre-conditioned before the Shamal event.

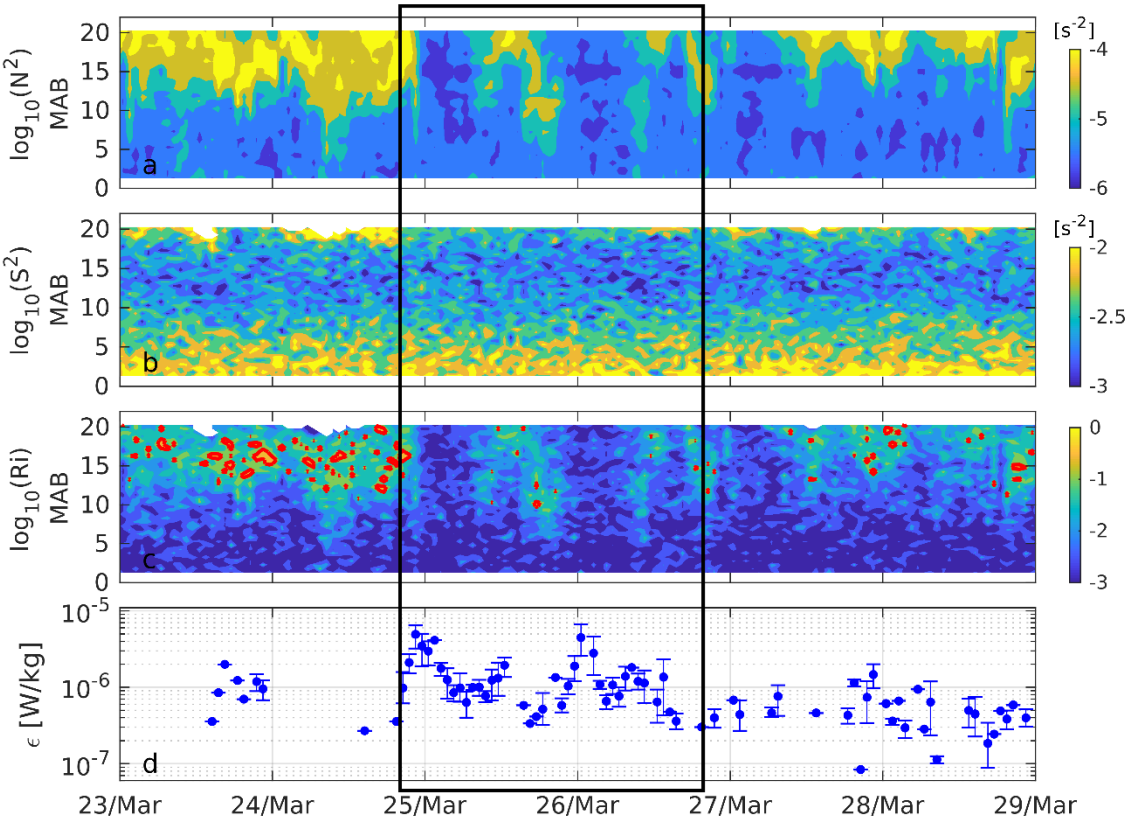

Figure 2.9 (a) buoyancy frequency squared, (b) velocity shear squared, (c) gradient Richardson number. Red contours denote gradient Richardson number of 0.25, (d) TKE dissipation rates estimated from the ADV measurements at 18 MAB. Vertical bar denotes the 95 % bootstrap confidence intervals. The box marks the Shamal event of 24-26 March, 2013.

The arrival of the first Shamal winds during the night of 24 March appeared to completely erase the stratification in the upper water column, resulting in a decrease in N^2 from ~10^{-4} to ~10^{-6} s^{-2} followed by a decrease in Ri from ~10^{-1} to ~10^{-3} (Figure 2.9 a, c). During daytime of 25 March, when the Shamal winds gradually decreased and short-wave radiation heated the surface (Figure 2.3 a, j), weak stratification ensued resulting in an increase in N^2 from ~10^{-6} to ~10^{-5} s^{-2}. During the night of 26 March, the second Shamal winds re-erased this weak stratification which was followed by a decrease in Ri in the upper water column. After the passage of the Shamal, both N^2 and Ri in the upper water column increased back to their Pre-Shamal levels (Figure 2.9 a, c).

Two peaks in ϵ were observed at 18 MAB corresponding to the two steady Shamal wind periods (Figure 2.3 a, Figure 2.9 d). During the first and the second steady Shamal winds periods, the measured mean ϵ values were 2.9x10^{-6} W/kg (95 % bootstrap confidence interval of 2.2x10^{-6}, 3.5x10^{-6} W/kg) and 2.7x10^{-6} W/kg (95 % bootstrap confidence interval of 1.9x10^{-6}, 3.8x10^{-6} W/kg), respectively. Analysis of average ϵ values for the Shamal-free and Shamal periods revealed a five-fold increase in the measured values from 2.3x10^{-7} to 1.2x10^{-6} W/kg.

2.5. Discussion and Conclusions

Winter Shamals are extreme but common meteorological events in the AG. In this study, the physical response of the NAG to winter Shamals was investigated using surface meteorological and moored oceanographic observations recorded from 19 January-19 April, 2013. A total of four winter Shamals were encountered during the

deployment. Measurements during one particular Shamal event, the event of 24-26 March, 2013, have been chosen and were presented here since it exhibited the largest increase in surface wind stress and latent heat flux (see Table 2.2).

2.5.1. Effects of Shamals on surface meteorology and wave

Surface meteorological measurements during the four winter Shamals showed an average increase in wind speed of 4.6 m/s, an increase in barometric pressure of 3.2 mb, and a decrease in relative humidity of 12.8 % (Table 2.2). This appears to be consistent with the recent findings reported by Al Senafi and Anis (2015) in a study that analyzed 40 years surface meteorological measurements in the NAG. Due to the strong winds and low humidity associated with winter Shamals, the latent heat flux showed higher variability than other heat flux components, with an average increase from 56.8 to 188.1 W/m^2 during the four Shamals (Table 2.2). This is similar to results reported by Thoppil and Hogan (2010) based on analyzing the objectively analyzed air-sea fluxes during winter Shamals. In addition, Shamal events may also affect the net short-wave radiation due to dust storms which are likely to be associated with Shamals. Based on 40 years of meteorological measurements, Al Senafi and Anis (2015) found a correlation of 0.42 (95 % bootstrap confidence intervals of 0.30 0.62) between the number of dust storm events per year and the number of Shamal days per year. During our field deployment, only one Shamal event (Shamal #3, 06-08 March, 2013) coincided with dust storms. This dust storm event lasted for one day (06 March, 2013) and resulted in a decrease from 168 to 73 W/m^2 in the daily averaged short-wave radiation. Dust storm events driven by

Shamals were also reported by Abdi Vishkaee et al. (2011) and Abdi Vishkaee et al. (2012).

Table 2.2 Variability of surface meteorological parameters. Values in parenthesis are averages over Shamal-free periods (two days before and after each Shamal event, see section 2.3.1).

	Time (year: 2013)	Wind speed (m/s)	Wind stress (N/m^2)	Relative humidity (%)	Barometric pressure (+1000 mb)	Latent heat flux (W/m^2)
Shamal #1	03-04 Feb.	10.1 (3.3)	0.19 (0.02)	53.0 (65.9)	21.7 (17.6)	185.6 (46.0)
Shamal #2	13-14 Feb.	8.5 (5.6)	0.14 (0.06)	58.9 (67.7)	15.6 (11.4)	160.0 (66.5)
Shamal #3	06-07 Mar.	9.3 (5.2)	0.16 (0.05)	49.5 (59.9)	13.5 (12.7)	223.9 (86.8)
Shamal #4	24-26 Mar.	7.5 (2.8)	0.11 (0.01)	47.2 (66.6)	13.1 (9.3)	182.9 (27.9)
Averages of four Shamals		8.8 (4.2)	0.15 (0.03)	52.2 (65.0)	15.9 (12.7)	188.1 (56.8)

During winter Shamals, surface wave heights and periods were found to increase from 0.58 to 0.82 m, and from 3.6 to 4.2 s, respectively (Table 2.3). The small increase in surface wave heights and periods is limited by the relatively small fetch associated with the north-northwesterly winds of Shamals in this region. In a study that examined extreme waves in Kuwait territorial water, Neelamani et al. (2007) reported that waves

generated by northerly winds were controlled mainly by the shallow bathymetry and the limited fetch length.

Table 2.3 Variability of surface waves, surface power inputs (from wind stress and buoyancy flux), and measured TKE dissipation rates during four winter Shamals. Measured TKE dissipation rates was obtained from an ADV at 18 MAB in nominal water depth of 27 m. Values in parenthesis are averages over Shamal-free periods (two days before and after each Shamal event). Variability of TKE dissipation rates during Shamal event #1 is not presented since less than 7 % of velocity spectra demonstrated a clear Kolmogorov -5/3 law (Kolmogorov, 1968).

	Wave height (m)	Wave period (s)	P_w ($x10^{-3}$ W/m^2)	P_b ($x10^{-3}$ W/m^2)	ϵ ($x10^{-7}$ W/kg)
Shamal #1	0.78 (0.49)	3.83 (3.75)	67.6 (3.2)	4.4 (1.8)	N/A
Shamal #2	0.78 (0.72)	3.91 (4.05)	43.4 (15.6)	3.6 (2.0)	9.1 (4.2)
Shamal #3	0.99 (0.64)	5.30 (3.69)	56.8 (10.7)	4.5 (2.2)	10.9 (4.3)
Shamal #4	0.75 (0.43)	3.82 (2.84)	34.8 (1.0)	3.9 (1.4)	12.1 (2.3)
Averages of four Shamals	0.82 (0.58)	4.21 (3.62)	50.7 (7.6)	4.1 (1.9)	10.7 (3.6)

2.5.2. Shamal effects on turbulent mixing

The increases in surface wind stress and heat loss driven by winter Shamals were found to increase turbulent mixing (Figure 2.10). Based on the measurements of the ADV at 18 MAB, averages over winter Shamals show an increase in ϵ from $3.6x10^{-7}$ to

1.1×10^{-6} W/kg between Shamal-free and Shamal periods (Table 2.3). During winter Shamals, the mean power input from winds was 5.1×10^{-2} W/m^2, one order of magnitude larger than the power input from surface buoyancy flux (Table 2.3). Using an average wind power input of ~5×10^{-2} W/m^2 measured during the winter Shamals and a nominal water depth of 25 m (water mass of ~25,000 kg/m^2) at our observational site, the energy dissipated throughout the water column is ~2×10^{-6} W/kg. Using our estimated value of ϵ (~1.1×10^{-6} W/kg) as the representative value for energy dissipation in the water column implies that the wind energy input is largely dissipated locally. In other words, an apparent local, roughly steady-state, balance between wind energy input and turbulence mixing appears to exist during Shamal events.

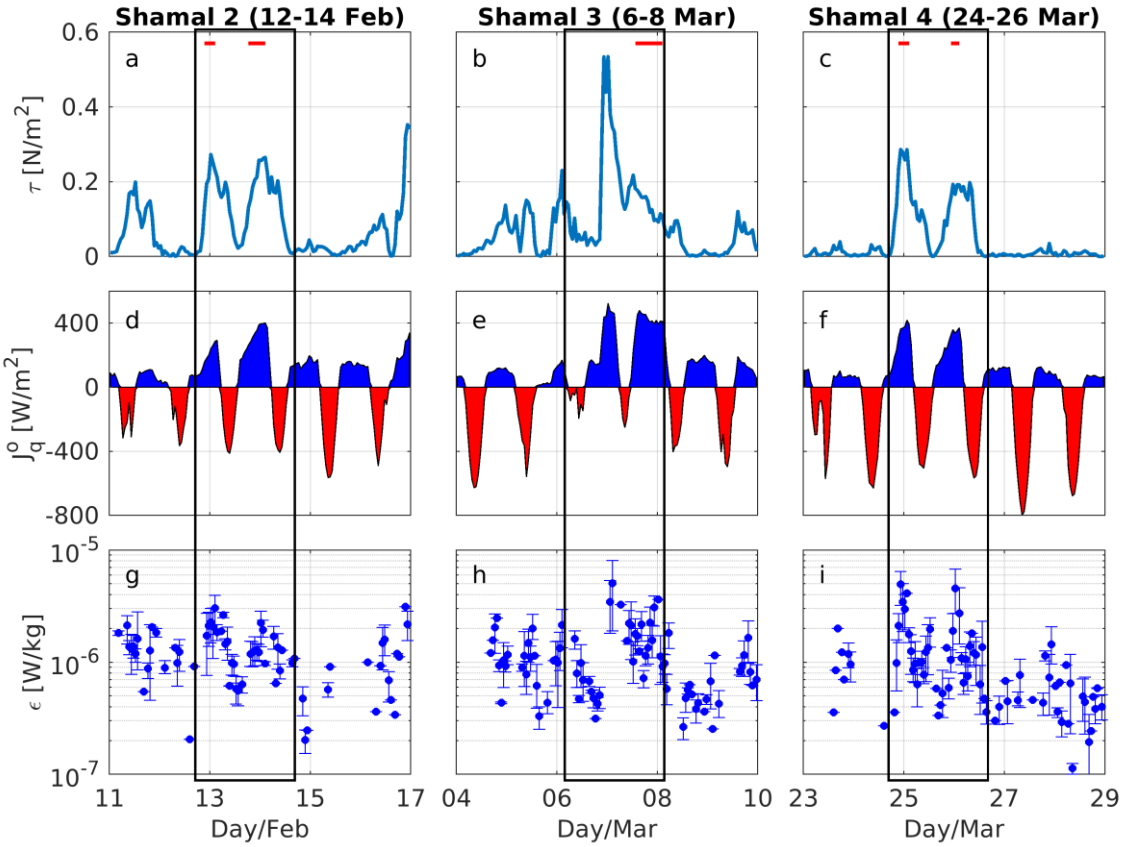

Figure 2.10 Time series of wind stress ((a)-(c)), net surface heat flux ((d)-(f)), and measured TKE dissipation rates ((g)-(i)) during Shamal #2 – #4. Red horizontal lines at the top of (a)-(c) represent the steady Shamal wind periods, i.e. steady surface winds stress and heat loss. Steady Shamal wind periods lasted ~13 hrs for each Shamal event. Blue/red shaded areas in (d) – (f) denote cooling/heating of the water column. Vertical bars in ((g)-(i)) denote the 95 % bootstrap confidence intervals. Time series of surface meteorological forcing and TKE dissipation rates during Shamal #1 are not shown due to the absence of TKE dissipation rates estimates.

During winter Shamals, surface wind stress, buoyancy loss (convection) and breaking surface wave (see section 2.5.1) are likely the main causes for enhanced mixing in the relatively shallow NAG. Next we examine the relative importance of these three

forcing mechanisms on turbulent mixing. (a) Surface wind stress: in the near-surface shear layer induced by surface wind stress, ϵ is expected to follow the law of the wall. In this case the TKE dissipation rate may be estimated as $= u_*^3/\kappa z$, where $u_* = \sqrt{\tau/\rho_w}$ is the surface friction velocity, τ is the surface wind stress, κ is von Kármán's constant taken as 0.41, and z is the distance from the sea surface (Thorpe, 2007). During steady Shamal wind periods (periods of both steady surface wind stress and heat loss denoted by the red horizontal lines in Figure 2.10 a-c), the average ratio of wall layer predicted values to the measured values of ϵ is about 0.41 (Figure 2.11 b, e).

(b) Convection: for turbulent mixing in the ocean driven by convection, ϵ was found to be approximately 0.8 of the surface buoyancy flux $J_b^0 = g\alpha_t J_q^0/C_p\rho_w$ (Anis and Moum, 1992). During the steady Shamal wind periods, J_b^0 accounts only for ~0.1 of the measured ϵ (Figure 2.11 c, f), implying that J_b^0 has a relative small contribution to mixing. This appears to be consistent with estimations of the Monin-Obukov length scale, $L_{MO} = u_*^3/\kappa J_b^0$, which characterizes the relative importance of surface wind stress and buoyancy flux to mixing in the water column (Dorrestein, 1979; Thorpe, 2007). L_{MO} marks a depth beneath/above which buoyancy contributes more/less than the wind stress to turbulent mixing. During steady Shamal wind periods, the mean values of L_{MO} was 65 m (95 % bootstrap confidence interval of 53, 79 m), which is much larger than the water depth (27 m) at our mooring site. This suggests wind stress contributes more on turbulent mixing than surface buoyancy flux in the entire water column.

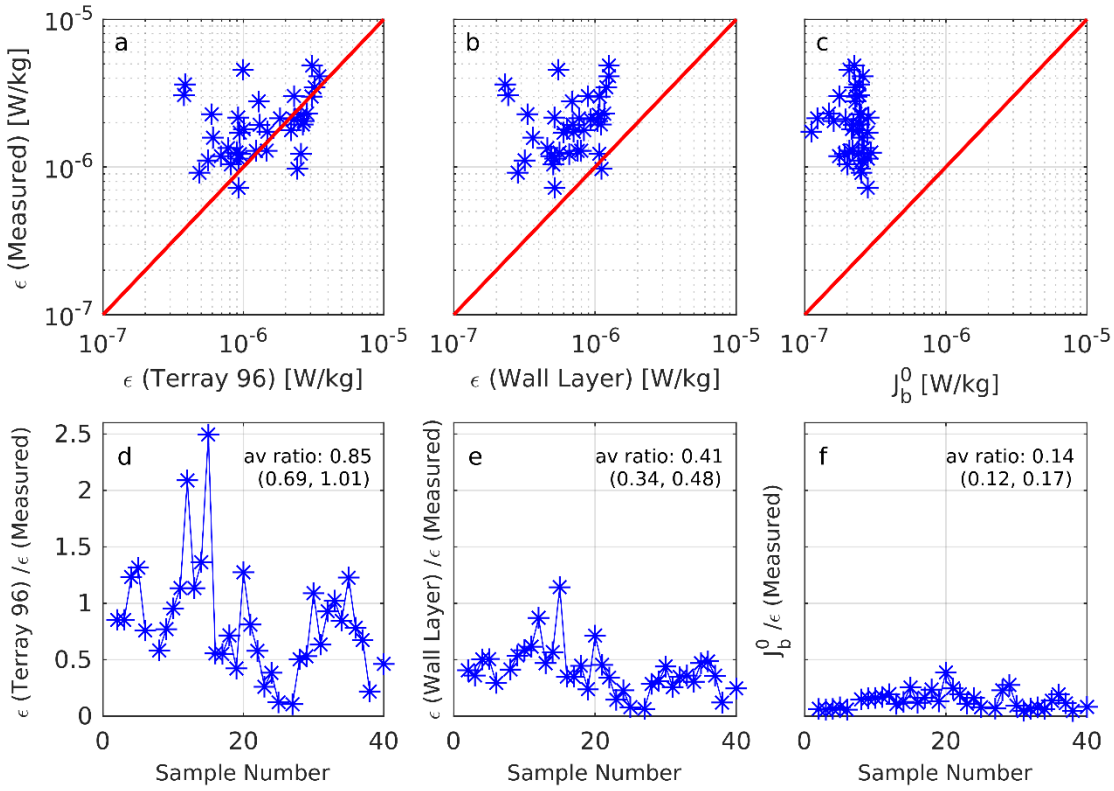

Figure 2.11 Upper row: scatter plots of measured ϵ (y-axis) vs. parameterized ϵ (x-axis): (a) Terray et al. (1996) parametrization, (b) law of the wall (Thorpe, 2007) parameterization, (c) surface buoyancy flux parameterization. The slope of the red lines in (a)-(c) is equal to 1. Lower row plots show the ratio between the parameterized ϵ and the measured ϵ values (y-axis) vs sample number. The texts in (d)-(f) are the averaged ratio and 95 % bootstrap confidence intervals.

(c) Surface waves breaking: we follow Terray et al. (1996) who divided the water column into three layers: a surface layer (from the surface down to a breaking depth, Z_b), an intermediate layer (between Z_b and a transition depth, Z_t), and a wall layer (beneath Z_t). Z_b and Z_t are defined as: $Z_b = 0.6H_s$, $Z_t = 0.3\kappa c H_s/u_*$, where H_s is the

significant wave height, and c is the effective wave phase speed. During the steady Shamal winds periods, our measurements at ~9 m beneath the surface were positioned inside the intermediate layer, where ϵ is parameterized as $\epsilon = (Z_t/z)u_*^3/\kappa z$ (Terray et al., 1996, Equation 13). This parameterization, with a mean ratio of 0.85 between parameterized and measured ϵ (Figure 2.11 a, d), does fit our measurements better than both the wall layer and/or the surface buoyancy flux parameterizations.

Based on (1) a close fit between measured ϵ and parametrized ϵ based on wave breaking; (2) L_{MO} estimations, and (3) higher surface power inputs from the wind than buoyancy flux (one order of magnitude difference, Table 2.3), we suggest that turbulent mixing during winter Shamals observed during this study, was mainly driven by breaking surface wave and wind shear production.

2.5.3. Possible implications of Shamals on the ecosystem

Based on the observed effects of winter Shamals on the hydrodynamics, it is expected that Shamal events are likely to have important impacts on the ecosystem in the AG. This is likely to occur through a two-fold effect: (1) elevated turbulent mixing levels, as reported in this study, are likely to enhance vertical fluxes of nutrients (Lalli and Parsons, 1993) from the seabed into the euphotic zone; (2) Shamals are frequently associated with severe dust storms (Abdi Vishkaee et al., 2012) and thus provide a likely vehicle for fertilization of the waters with iron (Husar et al., 1997; Nezlin et al., 2010). Both of these Shamal associated mechanisms may possibly contribute to significant increases in phytoplankton biomass. In addition, the sudden changes in water

temperature during Shamals could affect environmentally sensitive fauna such as coral communities (Cavalcante et al., 2016). Therefore, it would be of interest for future efforts to investigate the ecological processes (e.g. possible algal blooms and survival of coral larvae) in conjunction with the physical processes, resulting from Shamal events in the AG.

3. NEAP-SPRING VARIABILITY OF TIDAL DYNAMICS IN THE NORTHERN ARABIAN GULF

3.1. Introduction

Tides refer to the periodic rise and fall of sea surface, driven by the combined gravitational forces of the Earth, Moon and Sun. The intensity of tides depends on the relative positions of the Earth, Moon and Sun, the weakest tides occurring during neap periods when the Moon and Sun are perpendicular to each other. During spring periods the Moon and Sun are aligned, tidal elevations and velocities become intensified (e.g. Shi et al, 2011, Figure 1). One lunar period (29.53 days) will include two such neap and spring tidal cycles.

The neap-spring variabilities are of major importance to turbulent mixing in the ocean. Based on measurements in the Western English Channel, Sharples et al. (2001) found the bottom of thermocline to be eroded by enhanced turbulent mixing during spring tides. Given that the tidal power inputs are proportional to the velocity speed cubed (Thorpe, 2007), a double increase in current speed from neap to spring tides would increase the tidal power by a factor of 8. According to the definition given by Simpson and Sharples (2012), tidal mixing fronts occur where tidal stirring balances the buoyancy inputs from surface heating. The variations in tidal stirring during the neap-spring cycles appeared to shift tidal mixing fronts by ~10-20 km (Simpson and Sharples, 2012). In addition, neap-spring variabilities have significant impact on the marine ecosystem. Shi et al (2011) analyzed 8-year satellite ocean color data and concluded that

the neap-spring tidal cycles impact both optical properties and water turbidity in China's coastal areas. Using a 1-D numerical model, Sharples (2007) found the spring-neap tidal cycles to affect the near bottom organic carbon flux.

The Arabian Gulf (AG) is a shallow body of water residing between the Iranian coasts and the Arabian Peninsula, with a surface area of 2.39×10^5 km^2 and a volume of 8.63×10^3 km^3 (Reynolds, 1993). The mean water depth of the AG is ~36 m, with a maximum depth of 100 m occurring near the Strait of Hormuz (Chao et al., 1992). Surrounded by vast desert areas, the climate of the AG is arid with evaporation and precipitation rates estimated to be 1.44 m/yr (Privett, 1959) and 0.11-0.19 m/yr (Marcella and Eltahir, 2008), respectively. The total river discharge is ~1.1×10^2 km^3/yr, which translates to ~0.46 m/yr when averaged over the area of the AG (Reynolds, 1993). The loss of fresh water due to evaporation is replenished through water exchange with the Indian Ocean through the Strait of Hormuz (Reynolds, 1993). The high evaporation rate combined with water exchange with the Indian Ocean result in hypersaline water (salinity ~38.5-41 ‰, Al-Muzaini and Jacob, 1996) and reverse estuary circulations (Swift and Bower, 2003). The circulations in the AG can be simplified as two components: (1) a northwest current moving along the coast of Iran from the Strait of Hormuz; (2) a southeast current propagating along the southern AG (Chao et al., 1992, Figure 3.1 a). Due to the restricted water exchange through the Strait of Hormuz combined with numerous oil and gas explorations, the AG is subject to the impacts of marine hazards such as oil spills (Proctor et al., 1994) and harmful algal blooms (Zhao and Ghedira, 2014). Using the red tides in 2008 as an example, Richlen et al. (2010)

reported that this catastrophic event impacted fisheries, destroyed coral reef communities, and affected desalination plants in the AG.

Tides are important physical mechanisms driving current velocities and surface elevations in the AG (Reynolds, 1993). Based on observations conducted from November 2012 to January 2013, Azizpour et al. (2016) reported that: (1) current velocities in the Strait of Hormuz are mainly controlled by tides; (2) M2 and K1 are the most significant semi-diurnal and diurnal tidal constituents. John (1992) analyzed current measurements in the western AG and found that M2, S2, O1 and K1 are the four dominating tidal constituents. The significance of tides in the Northern AG (NAG) has also been observed by Sheppard (1993), who reported a difference in surface elevation of up to 4 m during spring tides off the northern coast of Kuwait. Based on the comprehensive oceanographic measurements collected during the research expedition between February to June, 1992, Reynolds (1993) suggested that tides are important for vertical mixing in the AG.

Due to the scarcity oceanographic observations in this region, the understanding of tidal dynamics, and in particular tidal mixing, is still lacking. The objective of this work is to (1) provide the first comprehensive observational results of tidal dynamics in the NAG; (2) characterize neap-spring variabilities of current velocities and near bottom turbulent mixing; (3) provide a better understanding of the role of tides in the hydrodynamics in the NAG. This paper is structured as follows: sections 3.2 and 3.3 describe the data and the methodology, section 3.4 summarizes the results and is followed by a discussion and conclusions in section 3.5.

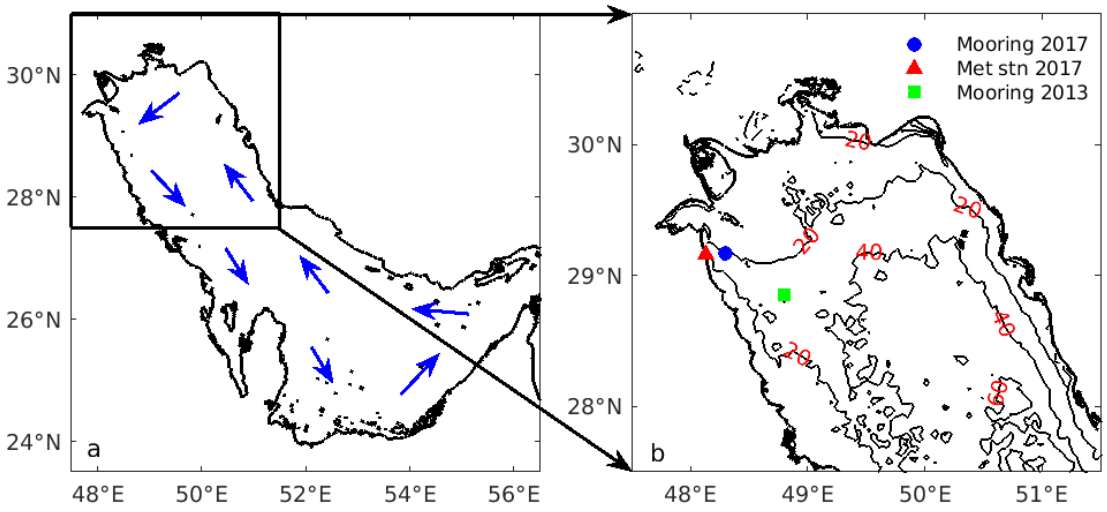

Figure 3.1 (a) schematics of the general circulation in the AG. This figure was adapted from Figure 7, Chao et al. (1992). (b) depth contours of the NAG. Blue dot and red triangle show the mooring location and the surface meteorological station during the deployment from 14-28 July, 2017. The green square denotes the mooring location during the deployment from 19 January to 19 April, 2013.

3.2. Data

3.2.1. Field experiment

Oceanographic and surface meteorological parameters were collected during a field experiment from 14 to 28 July, 2017. Oceanographic parameters were recorded from a mooring deployed at 29° 10.30' N, 48° 09.54' E (blue dot in Figure 3.1 b), approximately 3 km offshore of Kuwait's coastline. The nominal water depth at the mooring site was 23 m. The mooring was equipped with seven temperature loggers (three RBR solo T, three RBR solo T fast, and one RBR Duet) and one, upward-looking, acoustic Doppler

current profiler (ADCP; Nortek Signature 1000 kHz) mounted on a bottom frame. Measurement details of the moored instruments are summarized in Table 3.1.

Table 3.1 Meters above bottom (MAB), measured parameters and sampling frequency of the moored instruments. The nominal water depth at the mooring site was 23 m.

MAB	Instruments	Measured parameters	Sampling frequency [Hz]
19	RBR solo T	Temperature	2
16	RBR solo T fast	Temperature	16
14	RBR solo T fast	Temperature	16
12	RBR solo T fast	Temperature	16
10	RBR solo T	Temperature	2
8	RBR solo T	Temperature	2
0.7	RBR Duet T/D	Temperature	16
0.7	Nortek Signature 1000	Velocities, pressure	8

Surface meteorological parameters were recorded by a station on the coast (29° 09.85' N, 48° 07.69' E, red triangle in Figure 3.1 b), ~3 km from the mooring. The meteorological sensors suite was at a nominal height of 9 m above sea surface and included sensors for measurement of air temperature and relative humidity, wind speed and direction, barometric pressure, and incoming short-wave radiation and long-wave radiation. Measurements were taken every 2 sec and then averaged and logged at 1 min

intervals. Wind data between 21 to 23 July 2017 is missing due to a problem with power supply to the anemometer of our station. For this period, we used wind measurements provided by the Kuwait Meteorological Office station 11 (29.0° N, 48.2° E). From the measured surface meteorological parameters, we calculated surface wind stress and individual surface heat flux components using the Coupled Ocean–Atmosphere Response Experiment (COARE) parameterizations (Fairall et al., 2003). The net surface heat flux, J_q^0, is the sum of the four individual surface heat flux components: the net short-wave radiation corrected for albedo; the net long-wave radiation; the sensible heat flux and the latent heat flux (Anis and Singhal, 2006). In this study, upward (downward) surface heat flux is defined as positive (negative) value.

3.2.2. ADCP data

The ADCP used for this study, a Nortek Signature 1000 kHz, is a broadband five-beam ADCP with four slanted beams and one vertical beam, used here in the High Resolution (HR) mode. For all five beams, beam velocities were recorded using burst measurements. Each burst contained 1800 samples with a sampling rate of 8 Hz, and burst intervals of 360 s. For the four slanted beams, 35 vertical bins were used with a bin size of 0.5 m. For the vertical beam, a total of 114 vertical bins were used with a bin size of 0.05 m. Erroneous velocities were noticed in the first 10 bins of the vertical beam, possibly due to interference from the bottom frame. To avoid possible contamination, data used here starts from the 3rd bin of the four slanted beams, and the 15th bin of the vertical beam. Measurements of the four slanted beams covered 1.8-17.8 meters above

the bottom (MAB), and the vertical beam covered ~1.5-6.5 MAB. Nominal water depth at the mooring site was 23 m. Based on the measurement range of the vertical beam, we define a near bottom layer (NBL) as the layer spanning 1.5-6.5 MAB.

Data quality control was applied before final analysis as follows: for the four slanted beams, velocities were rejected if signal correlation was less than 50 % or signal amplitude was less than 25 dB; for the vertical beam, velocities were rejected if signal correlation was less than 60 % or signal amplitude was less than 25 dB. These thresholds were chosen based on personal communications with Nortek engineers. In addition, velocity spikes were detected using the Grubbs' outliers test (Grubbs, 1969) and replaced by the Expectation Maximization Method (Schneider, 2001). Bursts were discarded if more than 90 % of velocities were flagged as bad in that burst. Lastly, the velocities collected by the four slanted beams were converted to earth coordinate velocities and then rotated to cross/along shore velocities. The cross shore velocities (V_c) are defined as parallel to 17° north of east, and the along shore velocities (V_a) are defined as parallel to 17° west of north.

3.2.3. Supporting data

An additional data set was used in this study to support the results. It included surface elevations and current velocities measured by a bottom-mounted upward looking ADCP (Nortek 1 MHz Aquadopp) at 28° 51' N, 48° 48' E (green square in Figure 3.1 b) from 19 January to 19 April, 2013. Comparison of the two deployments (July 2017 and January-April 2013) shows that spectra of surface elevations and horizontal velocities

were similar (Figure 3.2) between the two datasets substantiating the representativeness of the surface elevation and current velocity measurements made in summer 2017.

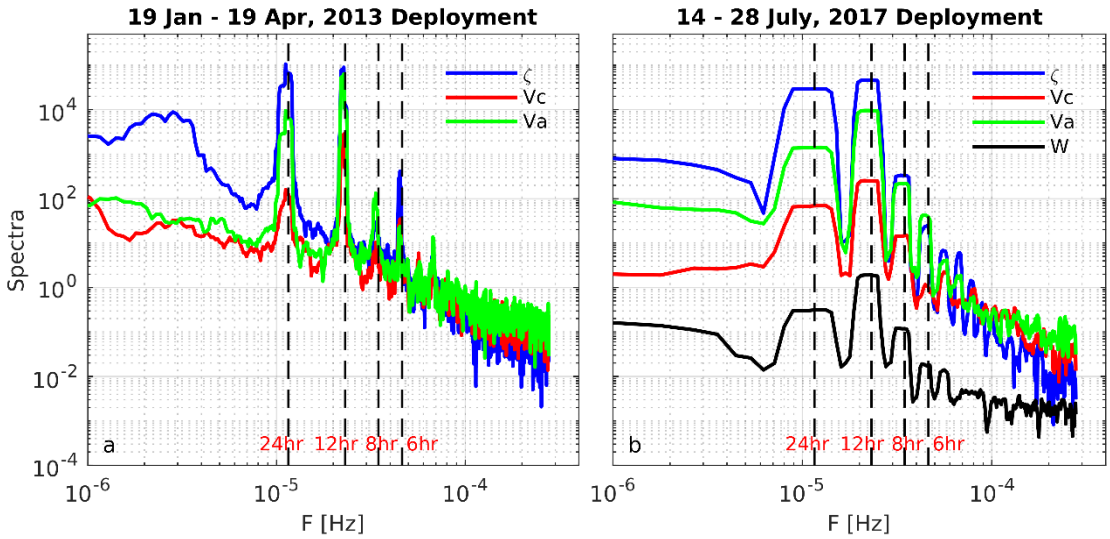

Figure 3.2 (a) spectra of surface elevation (ζ), vertically averaged cross-shore velocity (V_c), and along-shore velocity (V_a) during the 19 January–19 April, 2013 deployment. (b) spectra of ζ, vertically averaged V_c, V_a and vertical velocity (W) during the 14–28 July, 2017 deployment. Vertical dashed lines (left to right) represent periodicities of 24, 12, 8, 6 hr. The units for surface elevation and velocity spectra are m^2/Hz, and $(m/s)^2$/Hz, respectively. Spectra in (a) and (b) were estimated using the multitaper method (Thomson, 1982), with the number of discrete Fourier transform points equal to the number of samples. The flat peaks in (b) are the result of the frequency resolution, $1/T$, being defined by the total measurement duration T (here ~14 days).

3.3. Methods

3.3.1. Buoyancy frequency and gradient Richardson number

The buoyancy frequency squared, N^2, was estimated as:

$$N^2 = -\frac{g}{\rho_o}\frac{d\rho(z)}{dz}$$

where g is the gravitational constant, ρ_o is the mean water density, $\rho(z)$ is the water density as a function of depth, and z is the vertical coordinate. To compensate for the lack of salinity measurements on the mooring, we used salinity collected from a Conductivity and Temperature (RBR XR-420 CT) logger and a Conductivity, Temperature, Depth (RBR XR-420 CTD) logger deployed ~1.4 km from the mooring between 11-28 July, 2017. The CT and CTD were moored at 12.5 and 16 MAB, both within the relatively weak thermocline (Figure 3.3 a). A gradual decrease in salinity recorded by CT was observed after 17 July, 2017, likely due to biofouling. Based on the measurements of the CT and CTD before 17 July, we derived a linear salinity-temperature relation (S = 59.44 - 0.52T, where S and T are the salinity and temperature, respectively, Figure 3.3 b) and applied it to our data. Error analysis shows that using the inferred salinity underestimates N^2 by ~32 % on average (Figure 3.3 c).

The gradient Richardson number, Ri, was estimated as:

$$Ri = \frac{N^2}{S^2}$$

Where $S^2 = (du/dz)^2 + (dv/dz)^2$, is the squared shear of horizontal velocity, where u and v are the E-W and N-S velocity components, respectively. For two-dimensional stratified shear flows, instability can occur only if Ri is smaller than 0.25 (Howard,

1961; Miles, 1961). For three-dimensional stratified shear flows, the formal stability (see Abarbanel et al., 1984 for definition) requires Ri to be larger than 1 (Galperin et al., 2007). Here we follow Simpson and Sharples (2012) and use $Ri = 1$ as a threshold for the occurrence of fluid instability.

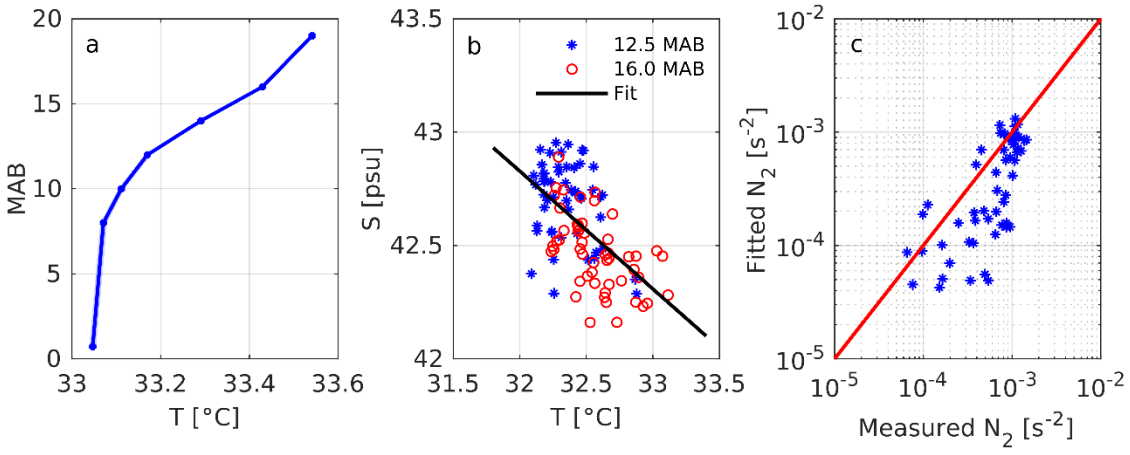

Figure 3.3 (a) Mean and 95 % bootstrap confidence intervals of water temperature during the deployment. The 95 % bootstrap confidence intervals (shown as shaded areas in (a)) are almost invisible due to the small difference. (b) scatter plot of temperature and salinity measured by the CT (12.5 MAB) and CTD (16.0 MAB) at the nearby mooring before 17 July, 2017, after which biofouling is suspected to have affected salinity values. The black line denotes a linear fit between salinity and temperature, given by S = 59.44 - 0.52T. (c) scatter plot of buoyancy frequency squared estimated from measured temperature and salinity (x-axis) and buoyancy frequency squared estimated from measured temperature and fitted salinity, S = 59.44 - 0.52T (y-axis).

3.3.2. Turbulent kinetic energy (TKE) dissipation rates

Visual examination of velocity spectra estimated from the four slanted beams of the Signature ADCP, revealed that only a relative small number of spectra showed a clear -5/3 energy cascade (see below) due to the limit imposed by the instrument's noise level. Thus, for estimation of ε we used only spectra estimated from velocities measured in HR mode along the vertical beam of the Signature.

For Reynolds number ($Re = Ud/\nu$, where U and d are the velocity and length scale of flows, and ν is the molecular viscosity) larger than 10^7, velocity spectra of isotropic and homogeneous turbulence follow a -5/3 energy cascade in the inertial subrange:

$$S(f) = \alpha\epsilon^{\frac{2}{3}}(\frac{2\pi}{V})^{-\frac{2}{3}}f^{-\frac{5}{3}}$$

where $S(f)$ is the power spectral density of the vertical velocity, $\alpha = 0.71$ is the Kolmogorov constant for transverse velocity spectra, V is the horizontal speed and f is the frequency (Kolmogorov, 1968; Thorpe, 2007). The inertial frequency subrange was taken as 0.1-1 Hz based on visual inspection of the velocity spectra. We follow Sato et al. (2014), who used velocity spectra to calculate ϵ if the spectral slope in the inertial subrange was within ±36 % of -5/3 (-2.27, -1.07), however we do impose a tighter limit of ±30 % of -5/3 (-2.17, -1.17) for a slope to be acceptable.

3.3.3. Turbulent diffusivity

Here we estimate turbulent diffusivity (K_ρ) following the parameterizations outlined by Shih et al. (2005). Based on the values of $\epsilon/\nu N^2$, Shih et al. (2005) proposed three

mixing regimes - diffusive, intermediate, and energetic - for K_ρ estimations. During the deployment, more than 95 % of $\epsilon/\nu N^2$ values were larger than 100 in the NBL. This indicates that the NBL at the mooring site belonged to the energetic mixing regime where turbulent diffusivity can be parameterized as $K_\rho = 2\nu(\epsilon/\nu N^2)^{0.5}$. It is worthy to note that the canonical parameterization ($K_\rho = \Gamma\varepsilon/N^2$, where Γ is the mixing efficiency, typically taken to be 0.2) proposed by Osborn (1980) overestimates turbulent diffusivity in our scenario. A comparison between the two different parameterizations is presented in section 3.5.

3.4. Results

3.4.1. Background surface meteorological conditions

Relatively calm surface meteorological conditions prevailed during the deployment, with an average wind speed and stress values of 3 m/s and 8.7×10^{-3} N/m^2, respectively (Figure 3.4 a). The net surface heat flux followed a consistent diurnal cycle pattern (Figure 3.4 b) and from 15 to 28 July, 2017, the net surface heat flux input amounted to 1.8×10^6 J/m^2 heating the entire water column.

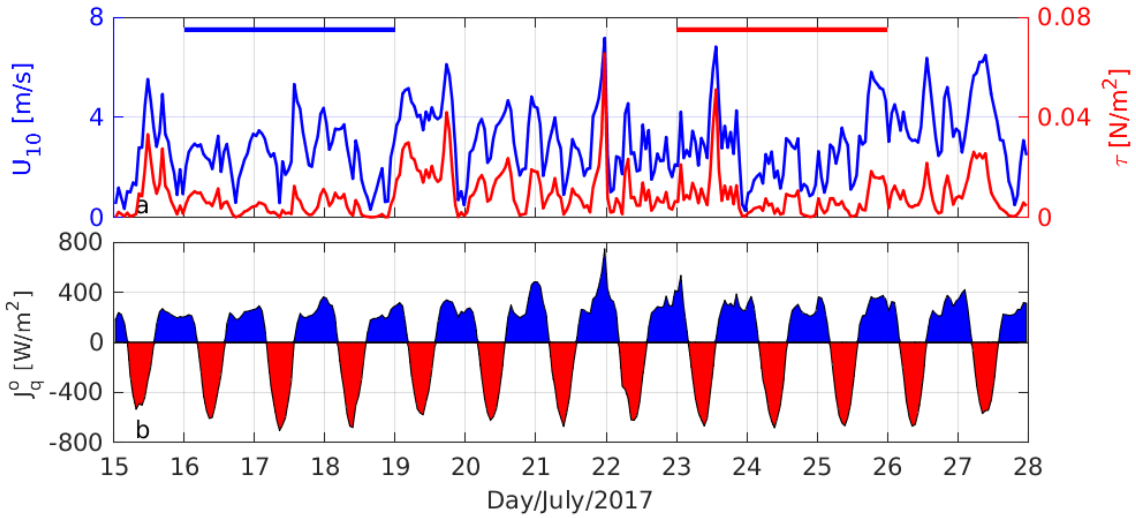

Figure 3.4 (a) surface wind speed and stress, (b) net surface heat flux. Blue and red horizontal lines in the top of panel (a) denote the neap and spring tide periods.

Table 3.2 Amplitudes (A), Greenwich phase lags (θ), and energy fractions (%) of the five major tidal constituents for surface elevation (ζ), cross-shore velocity (V_c) and along-shore velocity (V_a). Values of A, θ, and energy fractions are estimated from the harmonic analysis (for details see Codiga, 2011). Amplitudes are in m for surface elevation and in m/s for velocities. Phase lags are in degrees. Surface elevation and current velocity were measured from 19 January to 19 April, 2013 (see section 3.2.3).

Tidal constituents	Period (hr)	ζ			V_c			V_a		
		A	θ	%	A	θ	%	A	θ	%
M2	12.42	0.37	234	35.5	0.07	93	75.2	0.31	143	70.7
S2	12.00	0.15	288	5.7	0.03	150	14.3	0.13	204	12.7
K1	23.93	0.36	267	34.2	0.01	113	2.4	0.11	179	9.3
O1	25.82	0.29	212	20.8	0.01	25	1.5	0.08	127	4.6
N2	12.66	0.07	197	1.2	0.01	60	1.8	0.05	111	2.0

3.4.2. Surface elevations and current velocities

Surface elevations and current velocities were observed to be strongly influenced by tides in the NAG. Harmonic analysis of data from a 3-month deployment (19 January to 19 April, 2013; see section 3.2.3) suggests that tides account for 88 % variance of surface elevations, and 96 % variance of current velocity. The variance of surface elevations and current velocities were concentrated at the semi-diurnal and diurnal frequencies, with additional, relatively, low peaks at periodicities of 6 and 8 hr (Figure 3.2). Amplitudes, phase lags and relative contributions of the five principal tidal constituents are summarized in Table 3.2. Classification of the tides at the mooring site might be done using the form ratio, F (e.g. Pond and Pickard, 1983): $F = (A_{K1} + A_{O1}) / (A_{S2} + A_{M2})$, where A_{K1}, A_{O1}, A_{S2}, and A_{M2} are amplitudes of tidal constituents K1, O1, S2, and M2. The computed form ratio of 1.2, suggests mixed, primarily semi-diurnal, tides in the NAG.

Different tidal ranges were observed between the daily two high and low waters (Figure 3.5 a), consistent with the classifications of tides (mixed, primarily semi-diurnal, tides) in the NAG. The inequalities seemed to intensify from neap to spring tides. Between 22–26 July, 2017, a particular large tidal range close to 3 m was observed during daily ebbs (denoted by inverted triangles atop Figure 3.5 a). The strong ebb tides appeared to enhance horizontal speeds (see below) and turbulent mixing (see section 3.4.3) in the NBL. When progressing from neap to spring tides, the daily tidal ranges gradually increased from ~1.5 to ~3 m.

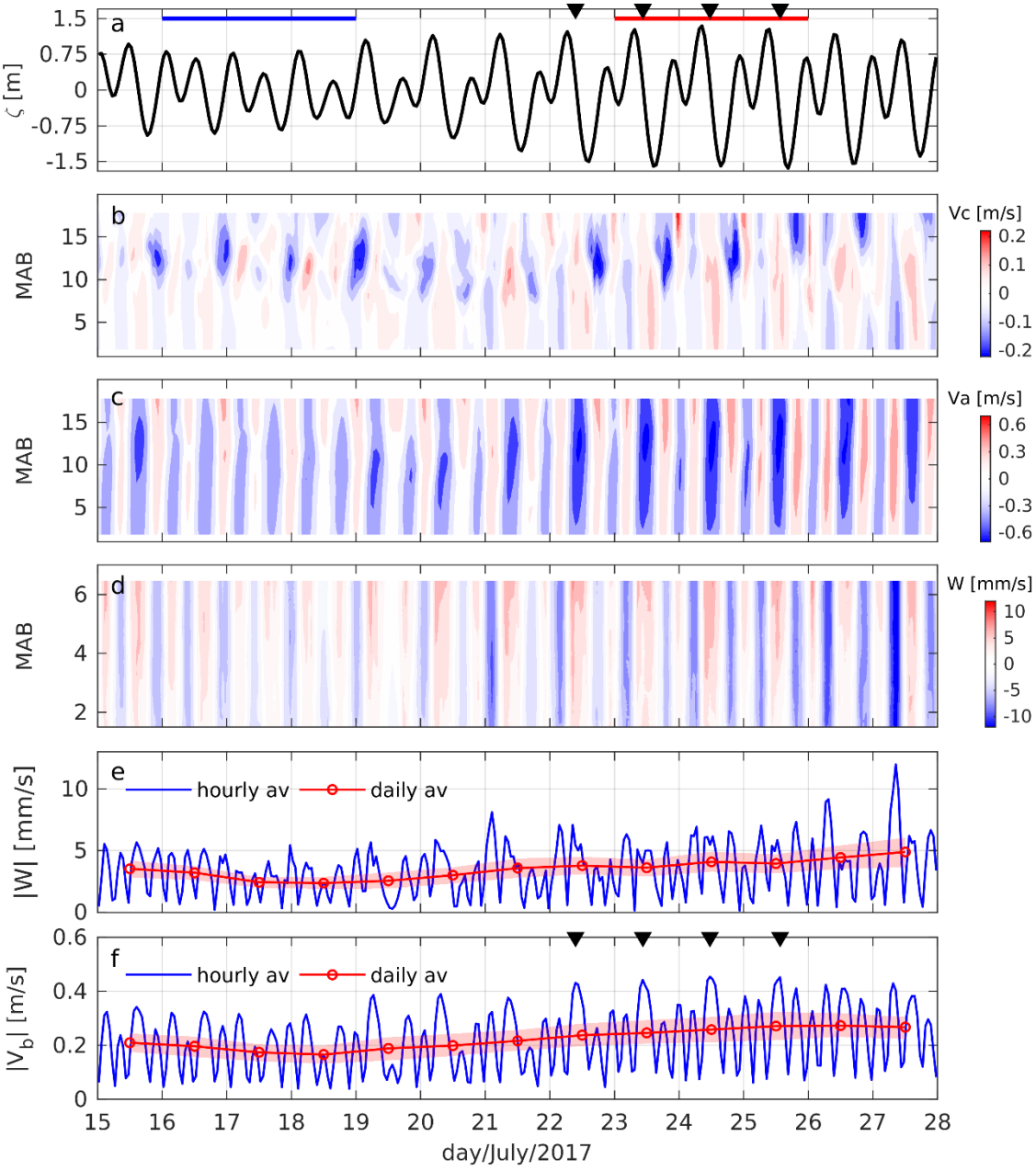

Figure 3.5 (a) surface elevations, (b) cross-shore velocities, (c) along-shore velocities, (d) vertical velocities, (e) vertical speeds averaged over the NBL, (f) horizontal speeds averaged over the NBL. Blue and red horizontal lines in the top of panel (a) denote neap and spring tides. The inverted triangles denote the occurrence of particularly large tidal ranges (a) and horizontal speeds (f) during daily ebbs between 22–26 July, 2017.

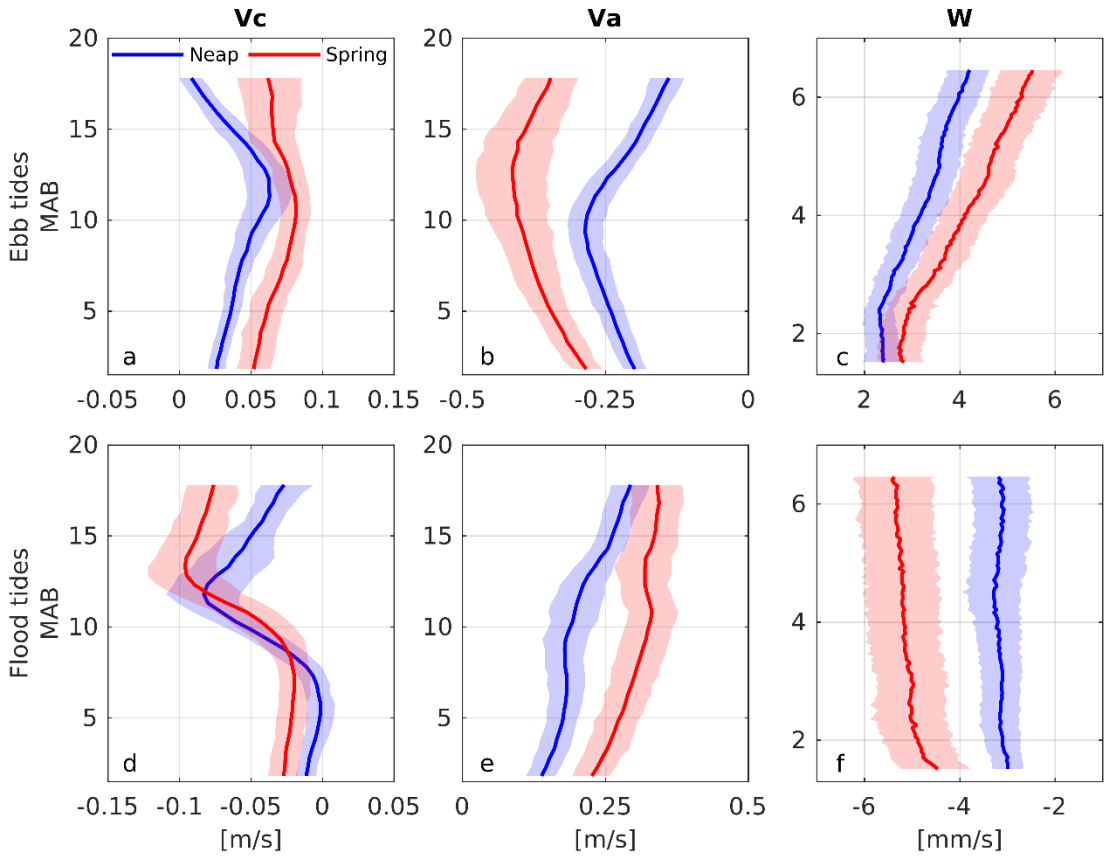

Figure 3.6 Comparison of velocity profiles for neap and spring tides. Velocity profiles were averaged over ebb and flood periods, respectively. Blue (red) lines in (a) – (c) are velocity profiles averaged over 6 ebb tides during neap (spring) tides. Blue (red) lines in (d) – (f) are velocity profiles averaged over 6 flood tides during neap (spring) tides. (a) and (d) are cross-shore velocities, (b) and (e) are along-shore velocities, and (c) and (f) are vertical velocities. Shaded areas denote the 95 % bootstrap confidence intervals.

Larger variabilities and amplitudes were observed in the along-shore velocities than in the cross-shore velocities (Figure 3.5 b, c), with a maximum along-shore velocity of ~0.6 m/s, triple that of the cross-shore velocity (~0.2 m/s). For the cross-shore velocities, onshore and offshore flows were observed during flood and ebb tides, respectively

(Figure 3.6 a, d). For the along-shore velocities, positive along-shore (northwest) currents occurred during flood tides, while negative along-shore (southeast) currents occurred during ebb tides (Figure 3.6 b, e). For both cross-shore and along-shore currents, velocity speeds were higher during spring tides than during neap tides. From neap to spring tides, the mean horizontal speeds increased from 0.2 to 0.3 m/s (Figure 3.7 a).

Semi-diurnal upwelling and downwelling were observed in the NBL, with a maximum vertical speed of ~10 mm/s (Figure 3.5 e). The variance of vertical velocities was concentrated in the diurnal and semi-diurnal bands, consistent with the surface elevations and horizontal currents (Figure 3.2 b). Further harmonic analysis for the deployments showed that tides accounted for 77 % of vertical current energy. During flood and ebb tides, downwelling and upwelling were observed in the NBL, respectively (Figure 3.6 c, f). During the flood tides, vertical velocities were almost homogeneous (Figure 3.6 f), while during the ebb tides, vertical velocities increased upwards ($\partial W/\partial z > 0$, Figure 3.6 c). The continuity equation, $\partial U/\partial x + \partial V/\partial y = -\partial W/\partial z$, then dictates that $\partial U/\partial x + \partial V/\partial y < 0$ during ebb tides, namely horizontal flow convergence.

The horizontal speeds show quarter-diurnal cycles in the NBL, with different amplitudes and durations between the two daily floods and ebbs. Between 22–26 July, 2017, a particularly strong horizontal speed (speed larger than 0.4 m/s) event was found daily (denoted by inverted triangles atop Figure 3.5 f), corresponding to the large tidal

ranges (~3 m) during daily ebbs (Figure 3.5 a). The strong horizontal speed events appeared to enhance turbulent mixing in the NBL (see section 3.4.3).

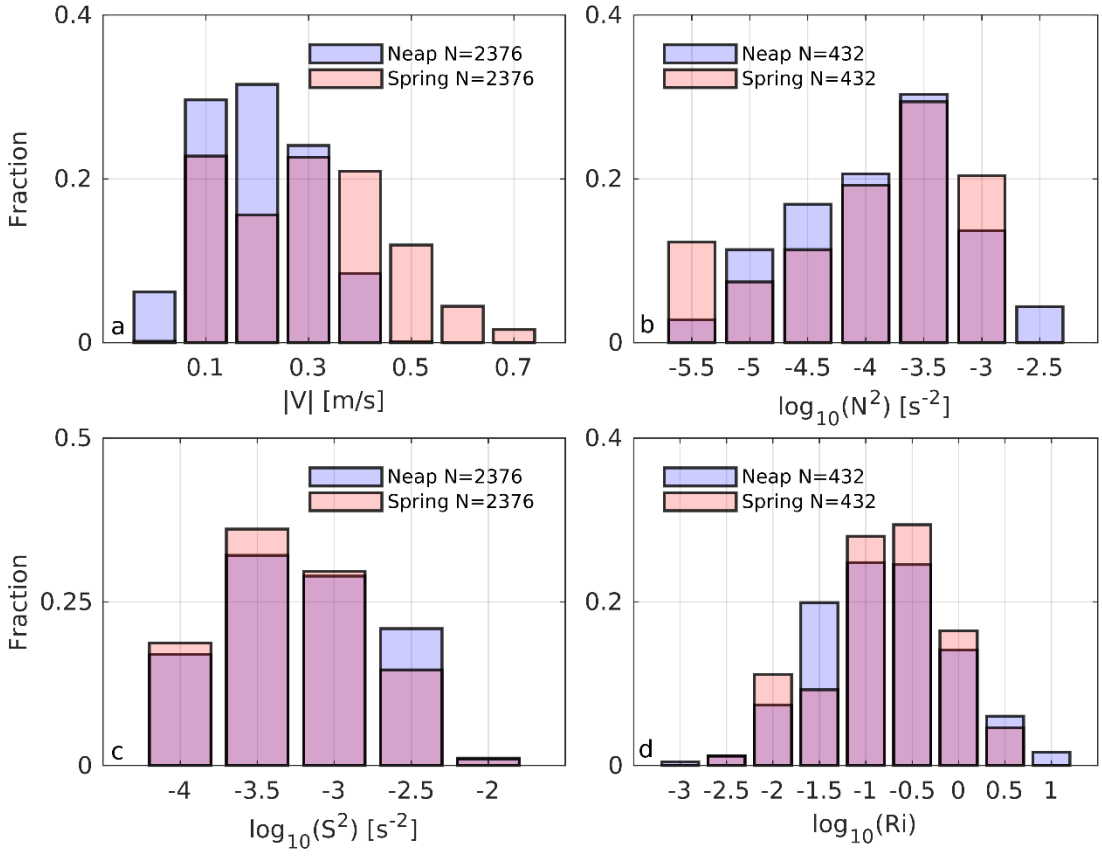

Figure 3.7 Relative distributions of (a) horizontal speed, (b) buoyancy frequency squared, (c) velocity shear squared, and (d) gradient Richardson number throughout the entire water column during neap and spring tides. The number of samples N is shown in the legend.

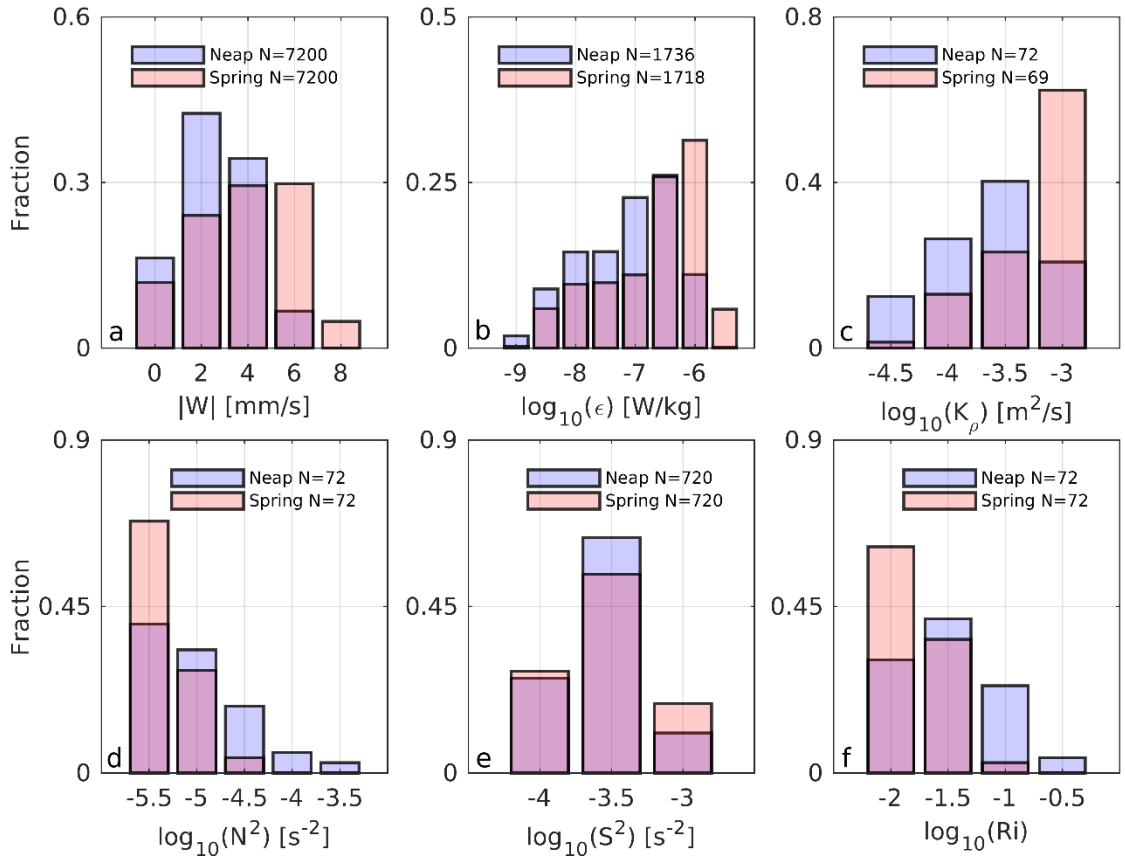

Figure 3.8 Relative distributions of (a) vertical speed, (b) TKE dissipation rates, (c) turbulent diffusivity, (d) buoyancy frequency squared, (e) velocity shear squared, and (f) gradient Richardson number in the NBL during neap and spring tides. The number of samples N is shown in the legend.

Both the horizontal and vertical speeds increased when progressing from the neap to spring tides (Figure 3.5 e, f). Comparison between the neap and spring tides shows an increase in the mean horizontal speed from 0.18 to 0.26 m/s, and an increase in the mean vertical speed from 2.7 to 3.8 mm/s (Figure 3.8 a, Table 3.3).

Table 3.3 Variability of current speeds and mixing parameters (within the whole water column and in the NBL) during neap and spring tides. Values in brackets are 95 % bootstrap confidence intervals.

		Neap tides (16-19 July, 2017)	Spring tides (23-26 July, 2017)
Entire water column	$\|V\|$ [m/s]	0.20 (0.19 0.20)	0.30 (0.30 0.31)
	N^2 [1/s^2]	3.5×10^{-4} (3.0×10^{-4} 4.0×10^{-4})	3.1×10^{-4} (2.7×10^{-4} 3.4×10^{-4})
	S^2 [1/s^2]	1.1×10^{-3} (1.1×10^{-3} 1.2×10^{-3})	0.9×10^{-3} (0.9×10^{-3} 1.0×10^{-3})
	Ri	5.5×10^{-1} (4.5×10^{-1} 6.9×10^{-1})	4.1×10^{-1} (3.6×10^{-1} 4.8×10^{-1})
NBL	$\|V_b\|$ [m/s]	0.18 (0.17 0.19)	0.26 (0.25 0.27)
	$\|W\|$ [mm/s]	2.7 (2.7 2.8)	3.8 (3.8 3.9)
	N^2 [1/s^2]	2.1×10^{-5} (1.3×10^{-5} 3.0×10^{-5})	5.5×10^{-6} (4.5×10^{-6} 6.8×10^{-6})
	S^2 [1/s^2]	3.3×10^{-4} (3.1×10^{-4} 3.4×10^{-4})	3.6×10^{-4} (3.4×10^{-4} 3.8×10^{-4})
	Ri	5.4×10^{-2} (3.9×10^{-2} 7.6×10^{-1})	1.9×10^{-2} (1.6×10^{-2} 2.3×10^{-2})
	ϵ [W/kg]	2.2×10^{-7} (2.1×10^{-7} 2.4×10^{-7})	5.6×10^{-7} (5.3×10^{-7} 5.9×10^{-7})
	K_ρ [m^2/s]	3.8×10^{-4} (3.0×10^{-4} 4.6×10^{-4})	7.0×10^{-4} (6.1×10^{-4} 8.0×10^{-4})

3.4.3. Stratification and turbulent mixing

From 15 to 28 July, 2017, water temperature ranged from 32 to 34.5 °C (Figure 3.9 a), with a mean vertical temperature difference of ~0.5 °C over 19 m (Figure 3.3 a). The relatively weak vertical temperature gradients resulted in N^2 values in the range of 3×10^{-6} to 3×10^{-3} s^{-2}, and a diffuse thermocline ($N^2 > 3\times10^{-4}$ s^{-2}) located in the upper water column between ~12-17.5 MAB (Figure 3.9 b). S^2 ranged from 10^{-4} to 10^{-2} s^{-2} at the mooring site, with the strongest shear (S^2 ~10^{-2} s^{-2}) oscillating between ~9-16 MAB

(Figure 3.9 c). The relatively large velocity shear, in comparison to the buoyancy frequency, resulted in Ri values smaller than 1 during most of the deployment (Figure 3.9 d).

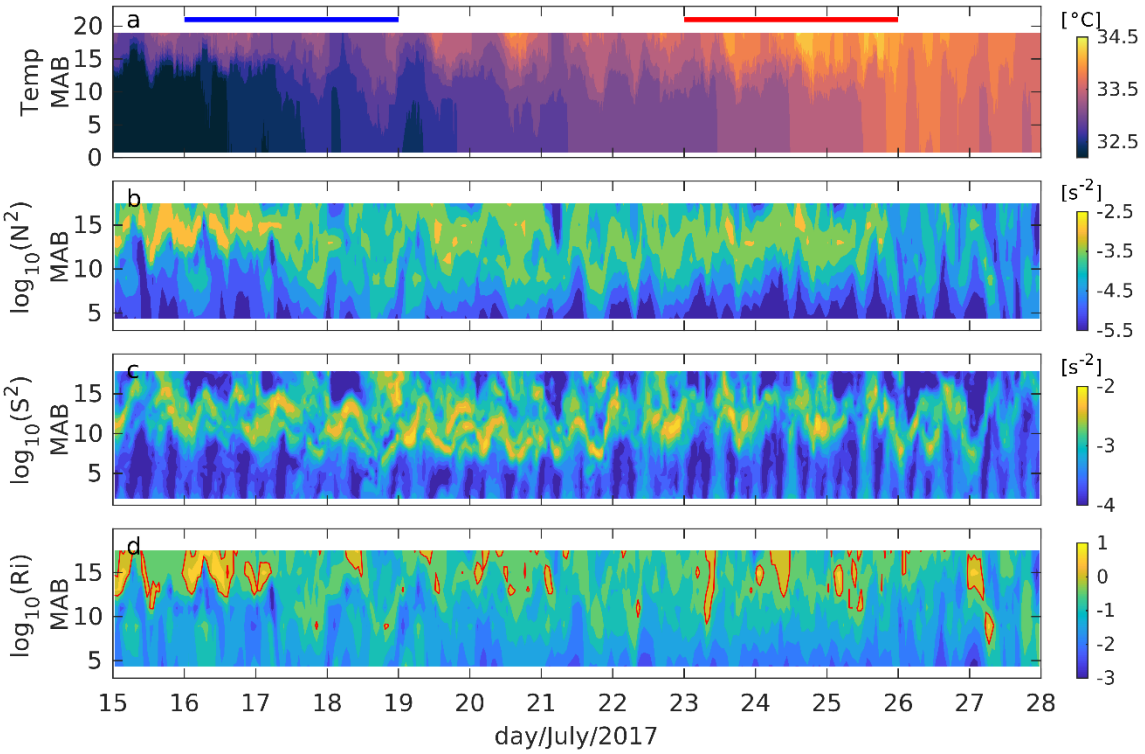

Figure 3.9 Contour plots of (a) water temperature, (b) buoyancy frequency squared, (c) velocity shear squared, and (d) gradient Richardson number during the deployment. Red contour lines in (d) mark gradient Richardson number values of 1. Blue and red horizontal lines at the top of panel (a) denote the neap and spring tide periods.

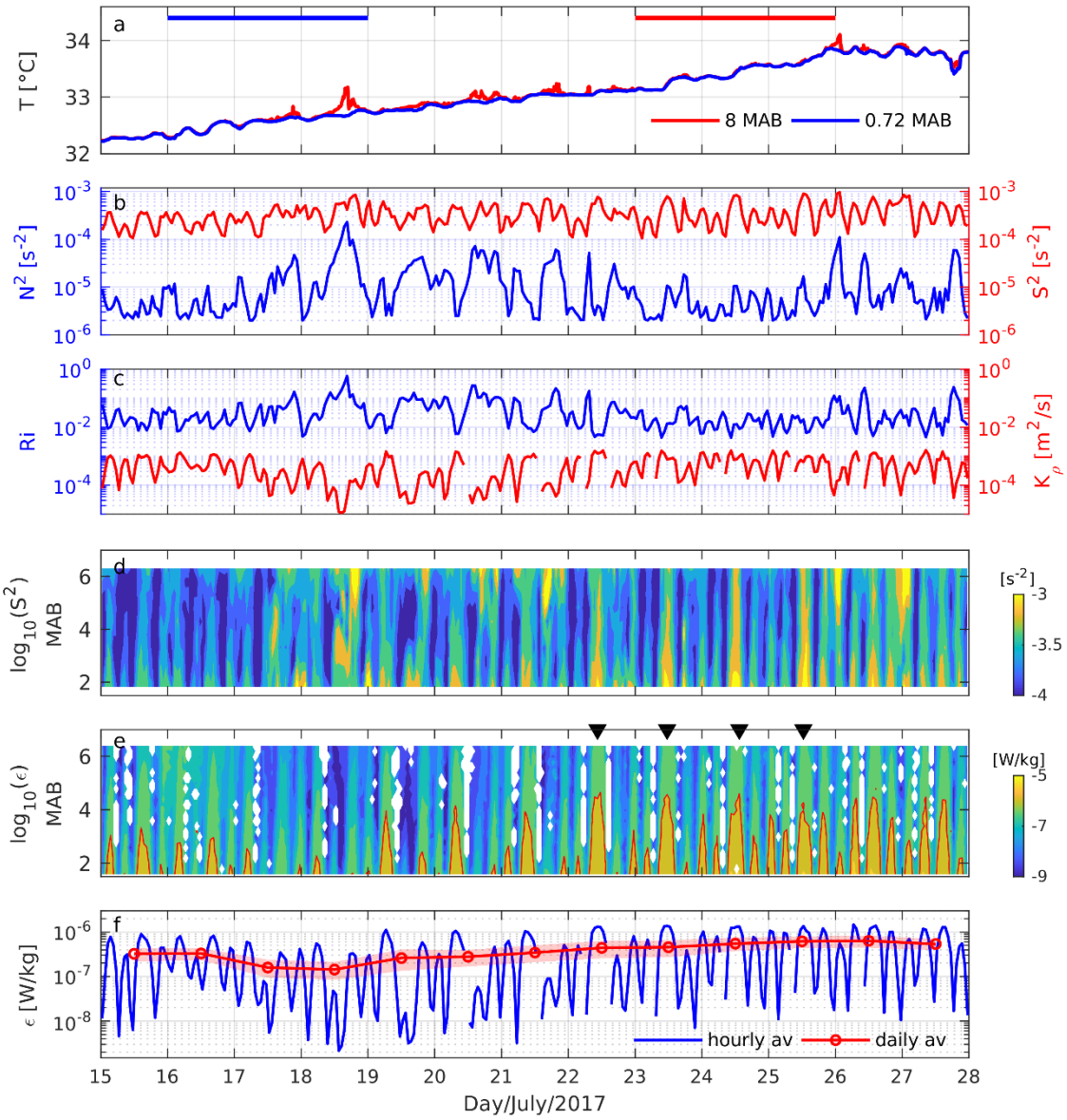

Figure 3.10 Parameters in the NBL: (a) water temperature, (b) buoyancy frequency squared and velocity shear squared, (c) gradient Richardson number and turbulent diffusivity, (d) velocity shear squared contours, (e) TKE dissipation rates contours, and (f) TKE dissipation rates averaged over the NBL. Blue and red horizontal lines at the top of (a) denote neap and spring tides. Buoyancy frequency squared in (b) was estimated based on temperature measurements at 0.72 and 8 MAB. Velocity shear squared in (b) was averaged over 1.8-6.3 MAB. The red contours in (e) represent TKE dissipation rates of 10^{-6} W/kg. The inverted triangles on top of (e) denote the occurrence of particularly strong mixing events between 22–26 July, 2017.

Water temperature was close to homogeneous in the NBL, with infrequent occurrences of small vertical temperature difference (Figure 3.10 a). The weak vertical temperature gradients in the NBL resulted in N^2 values of ~10^{-6}-10^{-4} s^{-2}, one to two orders of magnitudes smaller than the S^2 values of ~10^{-4} s^{-2} (Figure 3.10 b). During the entire deployment, Ri was always smaller than 1 (Figure 3.10 c), suggesting shear instability in the NBL. Examination of Ri and K_ρ showed a well-correlated relation between the two (Figure 3.10 c), with a correlation coefficient of -0.87.

Both ϵ and S^2 show quarter-diurnal cycles in the NBL, with different values and durations between the two daily floods and ebbs (Figure 3.10 d, e). Between 22–26 July, 2017, a particularly strong turbulent mixing event was observed daily (denoted by inverted triangles atop Figure 3.10 e), corresponding to the large tidal ranges (close to 3 m, Figure 3.5 a) and large horizontal speeds (greater than 0.4 m/s, Figure 3.5 f) during ebb tides.

From neap to spring tides, higher variabilities of N^2 and Ri were observed in the NBL than in the entire water column, as can be seen from both the vertical profiles (Figure 3.11 a-c) and the relative distributions (Figure 3.7 b-d, Figure 3.8 d-f). Using N^2 as an example, comparisons between the neap and spring tides show that N^2 decreased by a factor of 4 (from 2.1x10^{-5} to 5.5x10^{-6} s^{-2}) in the NBL, compared to only a slight decrease (from 3.5x10^{-4} to 3.1x10^{-4} s^{-2}) in N^2 averaged over the entire water column (Table 3.3). The decrease in N^2 from neap to spring tides is closely associated with the increase in turbulent mixing in the NBL (Figure 3.11 d). Further comparison between the

neap and spring tides shows an increase in mean ϵ values from 2.2x10^{-7} to 5.5x10^{-7} W/kg, and an increase in mean K_ρ values from 3.8x10^{-4} to 7.0x10^{-4} m^2/s (Table 3.3).

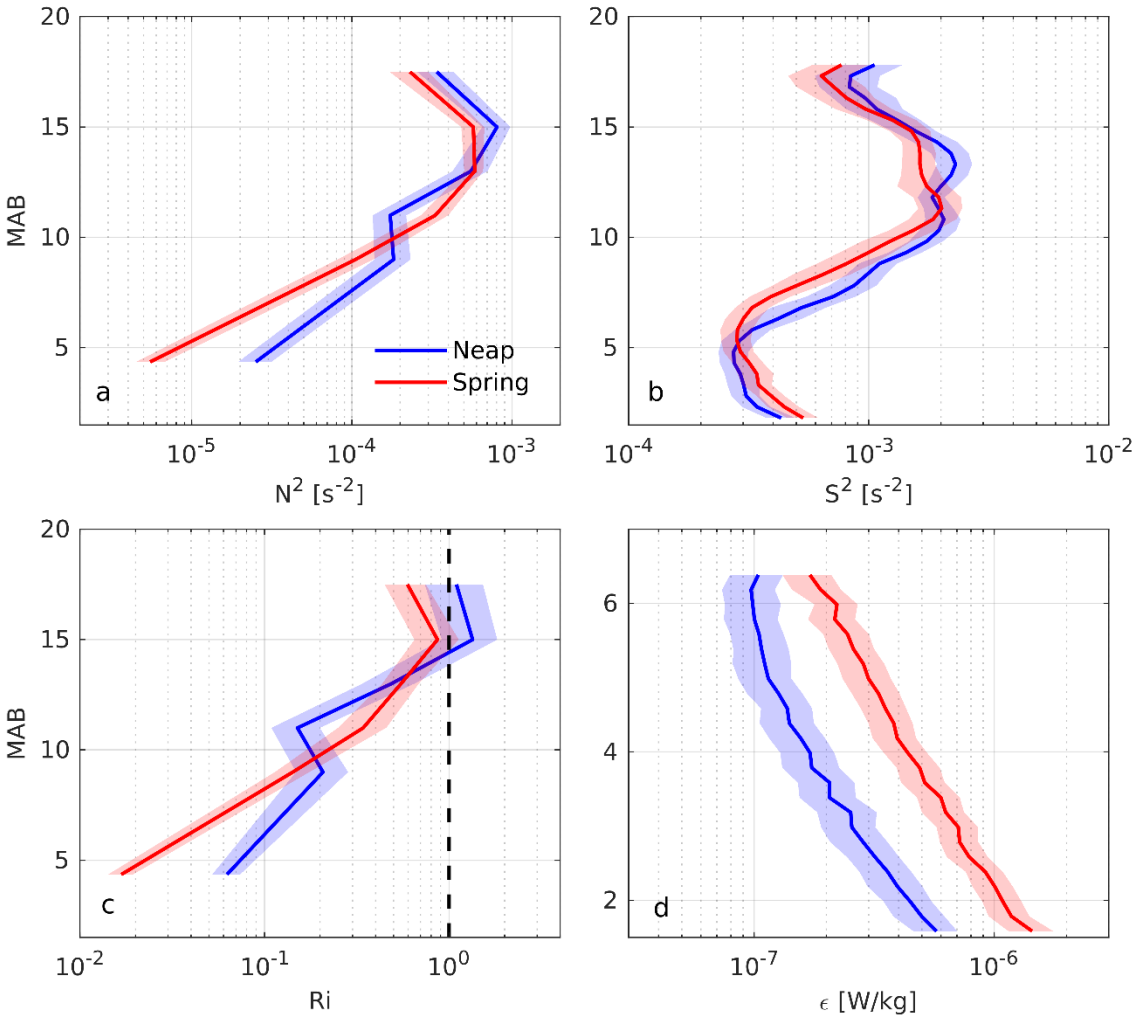

Figure 3.11 Vertical profiles of (a) buoyancy frequency squared, (b) velocity shear squared, (c) gradient Richardson number, and (d) TKE dissipation rates averaged over the neap and spring tide periods. Shaded areas denote the 95 % bootstrap confidence intervals.

3.5. Discussion and conclusion

In this study, we characterized the neap-spring variabilities of current velocities and turbulent mixing based on field measurements. The results described above are discussed in the next subsections.

3.5.1. Vertical velocities in the NBL

During the deployment periodic upwelling and downwelling were observed in the NBL with a maximum vertical speed of ~10 mm/s (Figure 3.5 d, e). Harmonic analysis for the whole deployment shows that the vertical velocities in the NBL were mainly induced by tides, with most of the energy concentrated in the semi-diurnal and diurnal frequencies (Figure 3.2 b). Progressing from neap to spring tides, the mean vertical speed in the NBL gradually increased from 2.7 to 3.8 mm/s (Table 3.3).

Analysis of the vertical velocity profiles revealed (1) downwelling during flood tides, with an almost homogeneous vertical velocity profile (Figure 3.6 f); (2) upwelling during ebb tides, with a positive vertical velocity gradient ($\partial W/\partial z > 0$, Figure 3.6 c). During flood tides, the averaged vertical velocity in the NBL was -3.8 mm/s (95 % bootstrap confidence interval of -3.5, -4.1 mm/s), ~15 % larger than the averaged vertical velocity of 3.3 mm/s (95 % bootstrap confidence interval of 3.1, 3.5 mm/s) during ebb tides. However, since ebb tides last ~15 % longer than flood tides, this yields a close vertical balance of volume fluxes between flood and ebb tides. During ebb tides, the positive vertical velocity gradient suggests horizontal convergence as required from

flow continuity. This may have further implications for the horizontal transports of sediments, nutrients, and waterborne pollutants in the NBL.

3.5.2. Turbulent mixing

At the mooring site, the entire water column appeared to be weakly stratified - the maximum vertical temperature difference of only ~1 °C over 19 m - even though the observations took place in the second half of July. A likely explanation of the observed weak stratification might be made using the tidal mixing front theory proposed by Simpson and Sharples (2012). Based on field measurements in the shelf seas of the western United Kingdom, Simpson and Sharples (2012) found that mixing intensities in the water column were associated with both the water depth and the tidal currents. Based on this observation they proposed a parameter, h/U^3 (h is water depth and U is the surface current speed during spring tide), as a criteria for different mixing regimes (Table 3.4). At our mooring site, the water depth and surface currents during spring tides were 23 m and 0.5 m/s, respectively, yielding a $\log_{10}(h/U^3)$ value of ~2.3 and indicating a transitional region (Table 3.4).

Table 3.4 Criteria for different mixing regimes following Simpson and Sharples (2012). h is the water depth and U is the surface current speed during spring tides.

	well-mixed regimes	transitional regimes	strongly stratified regimes
$\log_{10}(h/U^3)$	< 1.5	~ 1.9	> 3

Estimating K_ρ is of key importance for turbulent fluxes (Thorpe, 2007). Instead of a single parametrization for K_ρ ($K_\rho = \Gamma\varepsilon/N^2$, where Γ is the mixing efficiency, typically taken to be 0.2) as suggested by Osborn (1980). Shih et al. (2005) proposed three mixing regimes - diffusive, intermediate, and energetic - for K_ρ estimations. In our case of a weakly stratified NBL, comparisons between the two methods show that the ratio between the estimates based on Osborn's (1980) and Shih et al.'s (2005) model are 21 (95 % bootstrap confidence interval of 19, 23). The large inconsistency appears to result from values of the mixing efficiency (Γ) used by Osborn (1980). $\Gamma = 0.2$ appears to be largely valid in the intermediate mixing regimes (e.g. ocean thermocline) but was found to overestimate K_ρ in the energetic mixing regime (Shih et al., 2005), which is the case for the NBL in our scenario.

Both methods for K_ρ above require measurements of ϵ, which are often limited or simply unavailable. Here we tried to establish a parameterization of K_ρ as a function of Ri for the NBL. Relating K_ρ to mean flow properties such as Ri provides a convenient method for turbulent modeling (Forryan et al., 2013; Large et al., 1994; Peters et al., 1988). Due to the presence of strong velocity shear (Figure 3.10 b), we adopted a similar power function approach, $K_\rho = aRi^b$ (a and b are coefficients to be determined), to that used by Peters et al. (1988) in their parametrization of K_ρ in the upper shear layer (23-81 m beneath the surface). A fit of K_ρ to Ri yielded $K_\rho = 10^{-5}Ri^{-1\pm0.03}$ for Ri in the range of 10^{-3} to 10^{-1} (Figure 3.12). Comparison between our and Peters et al. (1988) parameterizations showed K_ρ decays much faster with increasing Ri in Peters et al.

(1988) relations than ours (Figure 3.12). For a decrease in K_ρ from ~10^{-3} to ~10^{-5} m^2/s, Peters et al. (1988) relation only required an increase in Ri from ~0.2 to ~0.4, while our relation showed an increase in Ri from ~10^{-3} to ~10^{-1}. The inconsistency may result from the different ranges for Ri (0.25-0.4 in their case, and 10^{-3}-10^{-1} in our scenario), mainly due to the difference in stratifications.

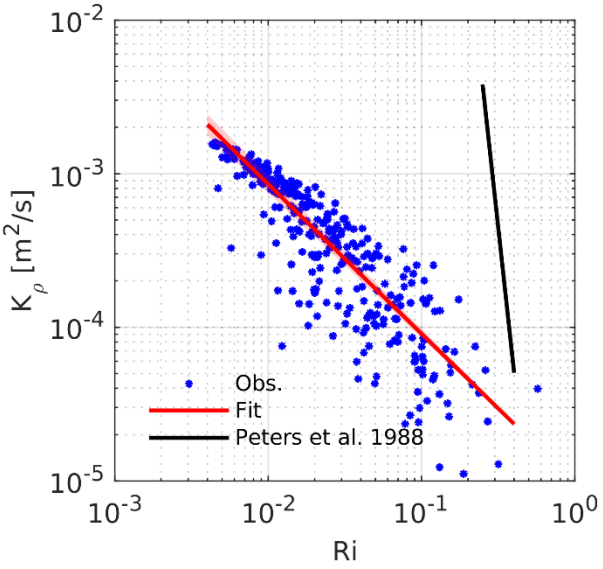

Figure 3.12 Scatter plot of turbulent diffusivity vs. gradient Richardson number in the NBL. The red solid line denotes the fit of turbulent diffusivity to gradient Richardson number. The black solid line represents the parameterization of Peters et al. (1988).

During the deployment, quarter-diurnal cycles were observed in ϵ at the NBL, consistent with results documented by Rippeth et al. (2001) in the Liverpool Bay, Irish Sea. Our measurements further show inequalities in ϵ between the daily flood and ebb tides, corresponding to the asymmetries in current speeds. Although the measurements were conducted in the NAG, this finding is likely to be applicable to other regions of tidal asymmetries commonly reported in shallow water environments (Li and Zhong, 2009; MacCready and Geyer, 2010; Shao et al., 2018).

Progressing from neap to spring tides, an increase in ϵ and K_ρ from 2.2×10^{-7} to 5.6×10^{-7} W/kg and from 3.8×10^{-4} to 7.0×10^{-4} m^2/s, respectively, was observed to follow the decrease in stratification in the NBL from 2.1×10^{-5} to 5.5×10^{-6} s^{-2}. The enhanced turbulent mixing and vertical currents (see section 3.5.1) during spring tides may facilitate sediment pumping (Scully and Friedrichs, 2007) and organic carbon fluxes (Sharples et al., 2001) at the bottom.

3.5.3. Wind and tidal power inputs

Winds and tides are the only two external power sources for mechanical mixing in the ocean (Munk and Wunsch, 1998). Here we compared the relative importance of wind and tidal power inputs in the NAG during the observations period. The wind power input, P_w, can be estimated as $P_w = \tau U_s$, where τ is the wind stress, U_s is the drift current speed induced by winds, and taken here as 3.1 % of the wind speed (Thorpe, 2007; Wu, 1983). The tidal power input, P_t, can be estimated as $P_t = \rho_0 C_d U_t^3$, where C_d is the bottom drag coefficient, typically taken to be 0.0025 for mud and sand bottoms

(Gross and Nowell, 1983), and U_t is the tidal velocity (Taylor, 1919). The measured velocity was used here to represent the tidal velocity, U_t, since tides account for 96 % variance of the current velocity (see section 3.4.2).

During the deployment, the mean wind power input (1.1×10^{-3} W/m^2) was found to be one order of magnitude smaller than the mean tidal power input of 2.6×10^{-2} W/m^2 (Figure 3.13 a). The tidal energy dissipated by local turbulent mixing can be estimated as $\rho_0 \iint \epsilon dz dt$, where t is time. Integration over the measured ϵ in the NBL ($E_{NBL} = \rho_0 \int \int_{z_1}^{z_2} \epsilon dz\, dt$, where z_1 and z_2 are 1.5 and 6.5 MAB) show that ~7 % of tidal energy was dissipated locally. If we can assume a constant stress layer beneath the NBL, i.e. from the sea-floor to 1.5 MAB where no estimates of ε were available, then we can utilize the law of the wall with $\epsilon = u_*^3/\kappa z$, where $\kappa = 0.41$ is the von Kármán constant, z is the distance above the sea-floor and u_* is the friction velocity estimated from the measured ϵ at 1.5 MAB ($u_* = \sqrt[3]{\kappa \epsilon|_{z=1.5} z|_{z=1.5}}$). The total energy loss due to turbulent mixing in the constant stress layer was computed as $E_{CSL} = \rho_0 \int \int_{z_0}^{z_1} \epsilon dz\, dt$, resulting in ~32 % of tidal energy loss in this layer (a value of $z_0 = 1$ cm was used for the roughness length based on the value documented by Chriss and Caldwell (1982) for a silt bottom, which is similar to seabed type in our case. If, for simplicity, we assume a constant value for ϵ above the NBL, i.e. between 6.5 MAB and the surface, where no estimates of ϵ were available, we can then estimate the tidal energy loss due to turbulent mixing above the NBL as $E_{ANBL} = \rho_0 \int \int_{z_2}^{z_3} \epsilon|_{z=6.5} dz\, dt$, where $z_3 = 23$ m is the water depth. Integration shows that ~9 % of the tidal energy may have been further dissipated above

the NBL. Thus, in total ~48 % of the tidal energy appears to be dissipated by local mixing within the entire water column (Figure 3.13 b). The rest of the tidal energy is likely to be converted into internal tides and/or to be dissipated remotely (Kang and Fringer, 2012; Nash et al., 2012).

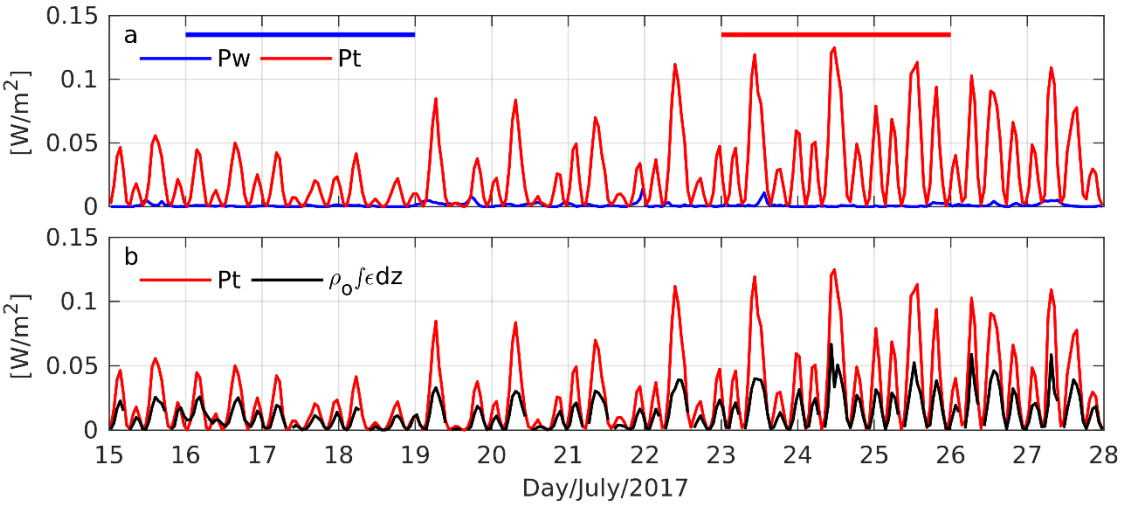

Figure 3.13 (a) wind and tidal power inputs, (b) tidal power input and the power dissipated by turbulent mixing in the entire water column. Blue and red horizontal lines in the top of panel (a) denote neap and spring tides.

4. OBSERVATION OF BAROCLINIC TIDES IN THE NORTHERN ARABIAN GULF

4.1. Introduction

Internal (i.e., baroclinic) tides refer to the vertical oscillations of stratified fluids with tidal frequency. They are ubiquitous dynamical processes in the global ocean, affecting energy cascade (Munk and Wunsch, 1998), turbulent mixing (Thorpe, 2007), and nearshore ecosystems (Woodson, 2018). Baroclinic tides are commonly generated by the interactions between barotropic tides, varying bathymetry and vertical stratifications (Rayson et al., 2011). They can be generated locally (Shroyer et al., 2012) or remotely (Kelly and Nash, 2010). The dual sources of baroclinic tides commonly render baroclinic tides unpredictable (Nash et al., 2012). Once generated, baroclinic tides can develop into higher-frequency motions due to the influence of background environments (Garrett and Kunze, 2007).

Baroclinic tidal currents are often comparable to the barotropic tidal flows, ranging from ~0.1 m/s in the open ocean to 1 m/s in the shallow water (Garrett and Kunze, 2007). Unlike barotropic flows which are independent of depth, baroclinic currents are characterized with rich velocity structures. Based on the 10-month current velocity measurements on the Pacific equator, Weisberg (1987) reported variable M2 tidal currents with depth in the upper water column, compared to approximately uniform M2 tidal currents below 1000 m. The horizontal velocity shear associated with the baroclinic tides can be strong enough to overcome vertical stratification, causing flow instability

and eventually turbulent mixing. For steady, non-diffusive, two-dimensional, and horizontal shear flows, Horward (1961) and Miles (1961) showed flow instability can occur when the gradient Richardson number (ratio between the horizontal velocity shear squared and the buoyancy frequency squared) is smaller than 0.25 in the flow.

Baroclinic tides provide an important pathway for energy cascade in the ocean. During the generation of baroclinic flows, energy is converted from the barotropic tides to the baroclinic tides. Globally speaking, the energy conversation rates for the M2 tides is ~14.5 GW near the continental slope (Thorpe, 2007). The energy contained in the baroclinic tides are then lost to turbulent mixing. Based on the numerical simulation results in the Monterey Bay, Kang and Fringer (2011) found 58 % of baroclinic tidal energy was dissipated locally. Turbulent mixing induced by baroclinic tides seems to impact marine ecosystem (Woodson, 2018). Based on the field measurements in the Florida Keys, Leichter et al. (2003) suggested the variability of nutrient concentrations resulted from turbulent mixing associated with the baroclinic tides.

The Arabian Gulf (AG) is a semi-enclosed shallow body of water surrounded by the Arabian Peninsula and the Iranian coasts. With a mean water depth of 36 m and surface area of 239,000 km^2, the volume of the AG is estimated to be 8630 km^3 (Chao, 1992; Reynolds, 1993). Resided in the subtropical areas, the climate is hot and arid in the AG. The evaporation rate is estimated to be 1.44 m/yr (Privett, 1959), one order of magnitude larger than the estimated precipitation rate of 0.11–0.19 m/yr (Marcella and Eltahir, 2008). The net evaporation in the AG is balanced with the water replenished through the Strait of Hormuz, with a net inflow rate of 321 km^3/yr (Reynolds, 1993). The restricted

water exchange with the open ocean combined with high evaporation rates resulted in hypersaline water in the AG, with salinity in a range of 38.5-41 ‰ (Al-Muzaini and Jacob, 1996). Based on numerical simulation results, Chao et al. (1992) reported cyclonic ocean circulations in the AG: one northwestward current proceeds along the Iranian coast, and one southward current moves along the Arabian coast.

Our study site, the Northern AG (NAG), is characterized as an energetic tidal region. A tidal range of 4 m has been documented by Sheppard (1993) off the coast of Kuwait during spring tides. Using our 3-month measurements as an example, harmonic analysis shows tides account for 86 % of surface elevation energy and 97 % of total current energy. Combined with sloping topography, the strong barotropic tides are expected to create baroclinic tides in the NAG. Therefore, the purpose of this work is to (1) provide observational evidence of baroclinic tides; (2) quantify the dynamics of baroclinic tides in the NAG. This study is structured as follows: data and methods are described in section 4.2. Results are presented in section 4.3, followed by discussion and conclusions in section 4.4.

4.2. Data and methods

4.2.1. Field deployment

Our mooring was deployed at the continental shelf of the NAG between 19 January to 19 April, 2013. The mooring location and details of the instruments are provided in section 2.2.2. In this study we used current velocity measured by one upward-looking,

bottom-mounted acoustic Doppler current profiler (ADCP) and water temperature measured by moored thermistors to examine the dynamics of the baroclinic tides.

4.2.2. Dynamical parameters of the baroclinic tides

Density anomaly (ρ') and isopycnal displacements (ζ) induced by the baroclinic tides can be estimated as:

$$\rho'(z,t) = \rho(z,t) - \bar{\rho}(z)$$

$$\zeta = \frac{\rho'(z,t)}{d\bar{\rho}(z)/dz}$$

where $\rho(z,t)$ is the raw density, $\bar{\rho}(z)$ is the background density estimated by applying 30-hour low pass filter to $\rho(z,t)$ (Rayson et al., 2011). Here we used a constant salinity of 42 PSU to calculate the density of sea water and buoyancy frequency squared (see below). Error analysis shows using a constant salinity would cause ~0.01 % error in the density and ~19 % error in the buoyancy frequency squared estimates. Eich et al (2004) suggested the equation for isopycnal displacement is not applicable under weak density gradient. Thus, here we only used density estimated closest to the surface (20.7 m meters above bottom (MAB), ~6 m depth) and closest to the bottom (0.7 MAB) to calculate ζ.

Baroclinic velocity $\boldsymbol{U}'$ is estimated as:

$$\boldsymbol{U}'(z,t) = \boldsymbol{U}(z,t) - \boldsymbol{U}(z) - \boldsymbol{U_0}(t)$$

where $\boldsymbol{U}(z,t)$ is the measured velocity, $\boldsymbol{U}(z)$ is the background velocity estimated by applying 30 hours low pass filter to $\boldsymbol{U}(z,t)$, $\boldsymbol{U_0}(t)$ is the barotropic velocity calculated

by requiring depth-mean baroclinic velocities are zero, namely $\frac{1}{H}\int_{-H}^{0} \boldsymbol{U}'(z,t)dz = 0$, where H is the water depth (Nash et al., 2005).

Here we used velocity measured closest to the surface (~6.5 m depth) as a representative of the surface value. The small measurement gaps near the surface appear not to affect the baroclinic velocity estimations (Rayson et al., 2011). Baroclinic velocities in earth coordinates were then rotated to cross/along shore directions. The positive cross-shore baroclinic velocities (U_c') is defined as 25° north of east, and the positive along-shore baroclinic velocity (U_a') is defined as 25° west of north.

Pressure anomaly induced by the baroclinic tides, p', can be estimated by:

$$p'(z,t) = p_{sfc}(t) + \int_{z}^{0} \rho'(\hat{z},t) g d\hat{z}$$

where $p_{sfc}(t)$ is the surface pressure inferred by requiring the depth-mean pressure anomaly is zero, namely, $\frac{1}{H}\int_{-H}^{0} p'(z,t)dz = 0$, and g is the acceleration due to gravity (Nash et al., 2005).

Horizontal Kinetic Energy (HKE), Available Potential Energy (APE), and the horizontal energy flux ($\boldsymbol{E}$) driven by the baroclinic tides were estimated as:

$$\text{HKE} = \frac{1}{2}\bar{\rho}(u'^2 + v'^2)$$

$$\text{APE} = \frac{1}{2}\bar{\rho}N^2\zeta^2$$

$$\boldsymbol{E} = \boldsymbol{U}'(z,t)p'(z,t)$$

where N^2 is the buoyancy frequency squared calculated by $N^2 = -\frac{g}{\bar{\rho}}\frac{d\rho}{dz}$ (Nash et al., 2006).

The gradient Richardson number, Ri, was estimated as: $Ri = N^2/S^2$, where S^2 is the horizontal velocity shear squared, calculated by $S^2 = (du/dz)^2 + (dv/dz)^2$. According to Howard (1961) and Miles (1961), the instability of two-dimensional, non-diffusive, horizontal steady shear flow can occur only if $Ri < 0.25$ in the flow. Thus, here we used Ri of 0.25 as the threshold for flow instability.

4.2.3. Study periods

Baroclinic tides were observed from the measured water temperature and current velocities during the entire deployment (19 January to 19 April, 2013). In the results section, we present the observational results from 22–29 January, 2013 as a representative of baroclinic tides in the NAG. Analysis on the 3-month baroclinic velocities is summarized in the discussion and conclusions section.

4.3. Results

4.3.1. Thermal structure, baroclinic velocities and pressure anomaly

During the study period from 22–29 January, 2013, semi-diurnal oscillations of isotherm were observed in the mooring site, as exemplified by the white contour line (denoting water temperature of 17.5 °C) in Figure 4.1 a. In the early morning of 28 January, 2013, ζ reached the maximum of 8 m, ~30 % of the total water depth of 27 m. Time series show opposite trends in ζ and the depth-averaged water temperature (Figure 4.1 b). The depth-averaged water temperature increased (decreased) during the downward (upward) isopycnal movements, with a correlation of -0.6.

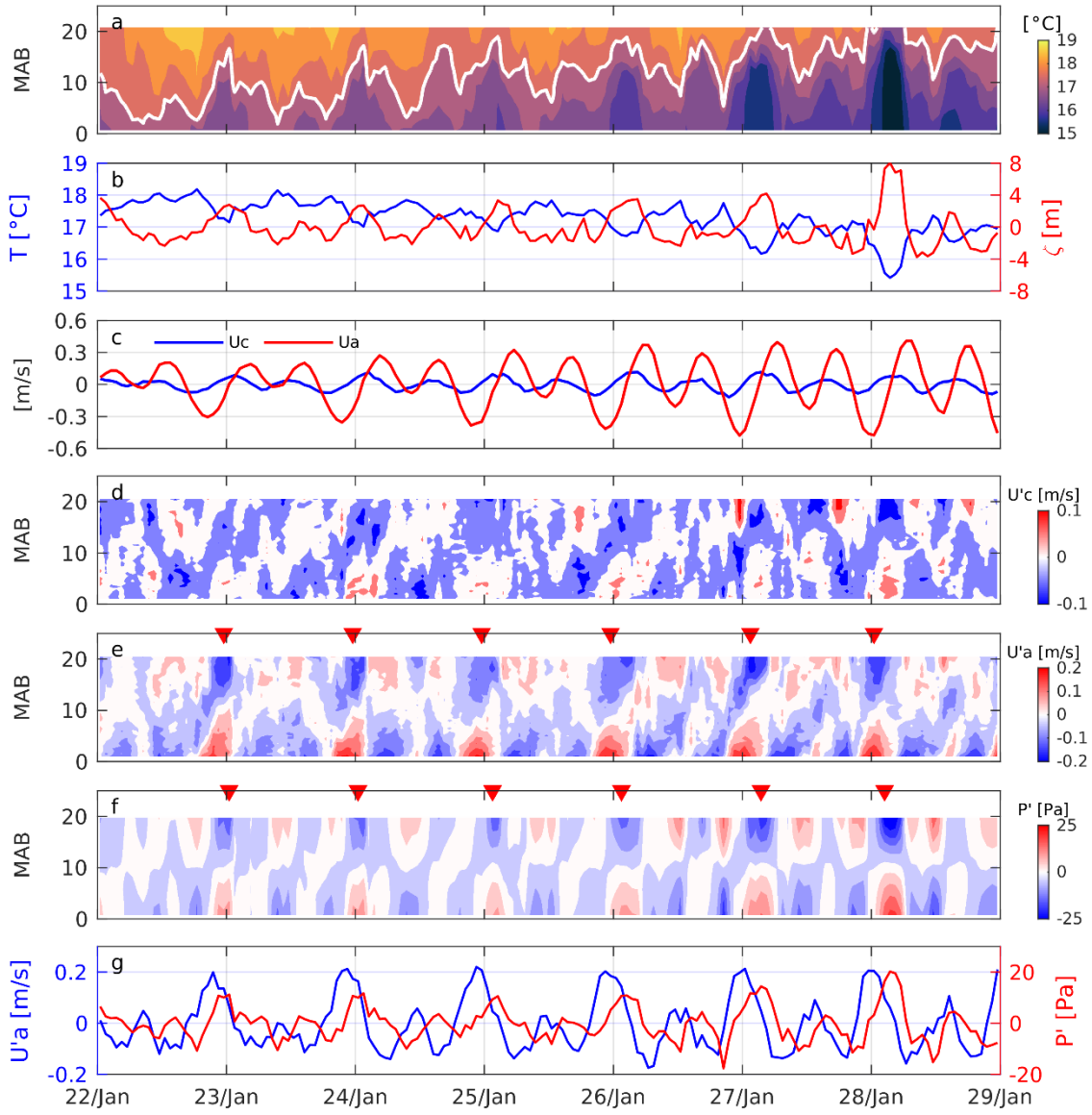

Figure 4.1 (a) water temperature contours, (b) depth-averaged water temperature and isotherm displacement, (c) cross-shore and along-shore barotropic velocities, (d) cross-shore baroclinic velocities, (e) along-shore baroclinic velocities, (f) pressure anomaly, (g) along-shore baroclinic velocity and pressure anomaly at 1 MAB. White contour lines in (a) denote water temperature of 17.5 °C. Red inverted triangles on top of (e) and (f) denote the daily occurrence of strong baroclinic tides.

For both barotropic and baroclinic flows, the velocity amplitudes were larger in the along-shore direction than in the cross-shore direction (Figure 4.1 c, d, e). The large amplitude in U_a' indicated the HKE of the baroclinic tides mainly resulted from U_a'. Baroclinic speeds were comparable to the barotropic counterparts in both cross-shore and along-shore directions. For example, the amplitude of U_a' was 0.2 m/s, ~40 % of the along-shore barotropic speed of 0.5 m/s (Figure 4.1 c, e). During the study period, the mean U_c' and U_a' were almost zero within the entire water column (blue lines in Figure 4.2 a, b).

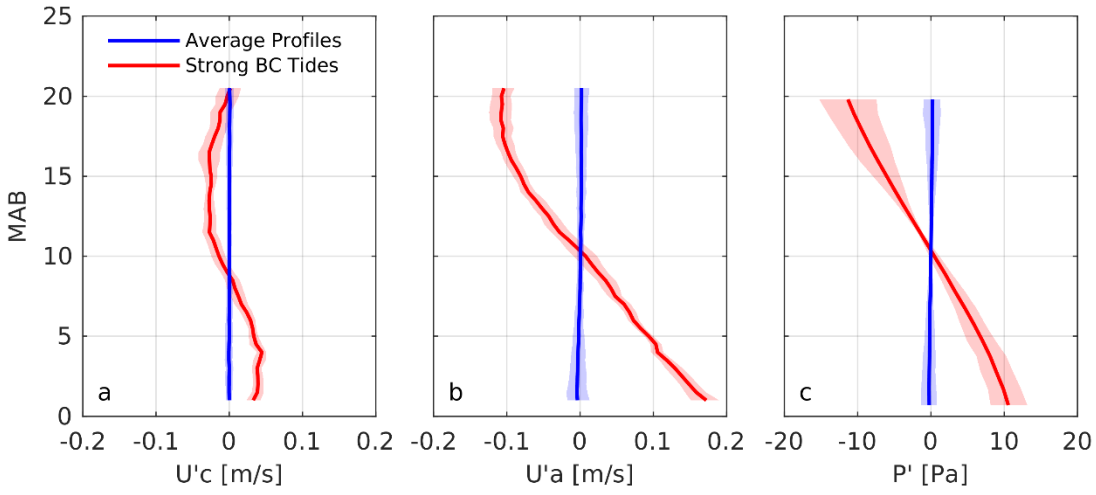

Figure 4.2 Depth profiles of (a) cross-shore baroclinic velocities, (b) along-shore baroclinic velocities, and (c) pressure anomaly. Blue lines are the profiles averaged over the study period between 22–29 January, 2013. Red lines are the profiles averaged over the strong baroclinic tides. The occurrence of strong baroclinic tides is denoted by the red inverted triangles on top of Figure 4.1 e, f. Each triangle stands for 3 hrs. Shaded areas denote the 95 % bootstrap confidence intervals.

Daily occurrence of strong baroclinic flows was observed in U_a' (denoted by the red inverted triangles on top of Figure 4.1 e). The occurrence of strong U_a' was associated with positive ζ (Figure 4.1 b, e). During the strong baroclinic flows, the directions of U_c' and U_a' were different in the upper (10 to 20 MAB) and lower (1 to 10 MAB) half of the water column, suggesting mode one baroclinic tides (see Webb and Pond, 1986). In the cross-shore direction (red line in Figure 4.2 a), offshore and onshore currents were found within the lower and upper water column, respectively (Figure 4.2 a). In the along-shore directions, positive along-shore (northwest) currents were observed in the lower water column with the maximum speed of 0.18 m/s at 1 MAB; negative along-shore (southeast) currents were observed in the upper water column with the maximum speed of 0.1 m/s at ~18 MAB. This resulted in a vertical shear of 0.28 m/s over 17 m for U_a'. Both U_c' and U_a' were 0 m/s at ~10 MAB.

p' ranged from -25 to 25 Pa between 22–29 January, 2013 (Figure 4.1 f). Similar to U_a', peak p' was observed near the surface and bottom with opposite signs. Averages over the study period show p' was almost zero within the entire water column (blue line in Figure 4.2 c). Corresponding to the baroclinic flow (Figure 4.1 e), daily occurrence of strong p' was observed (denoted by the red inverted triangles on top of Figure 4.1 f). Cross-correlation shows a 3-hour delay between U_a' and p' (Figure 4.1 e, f, g). Averages over the strong baroclinic flow show positive p' in the lower half of the water column with the maximum value of 10 Pa at 1 MAB; negative p' in the upper half of the water column with the maximum (negative maximum) value of -10 Pa at 20 MAB (red line in

Figure 4.2 c). This resulted in a vertical pressure difference of 20 Pa over a 19 m water column.

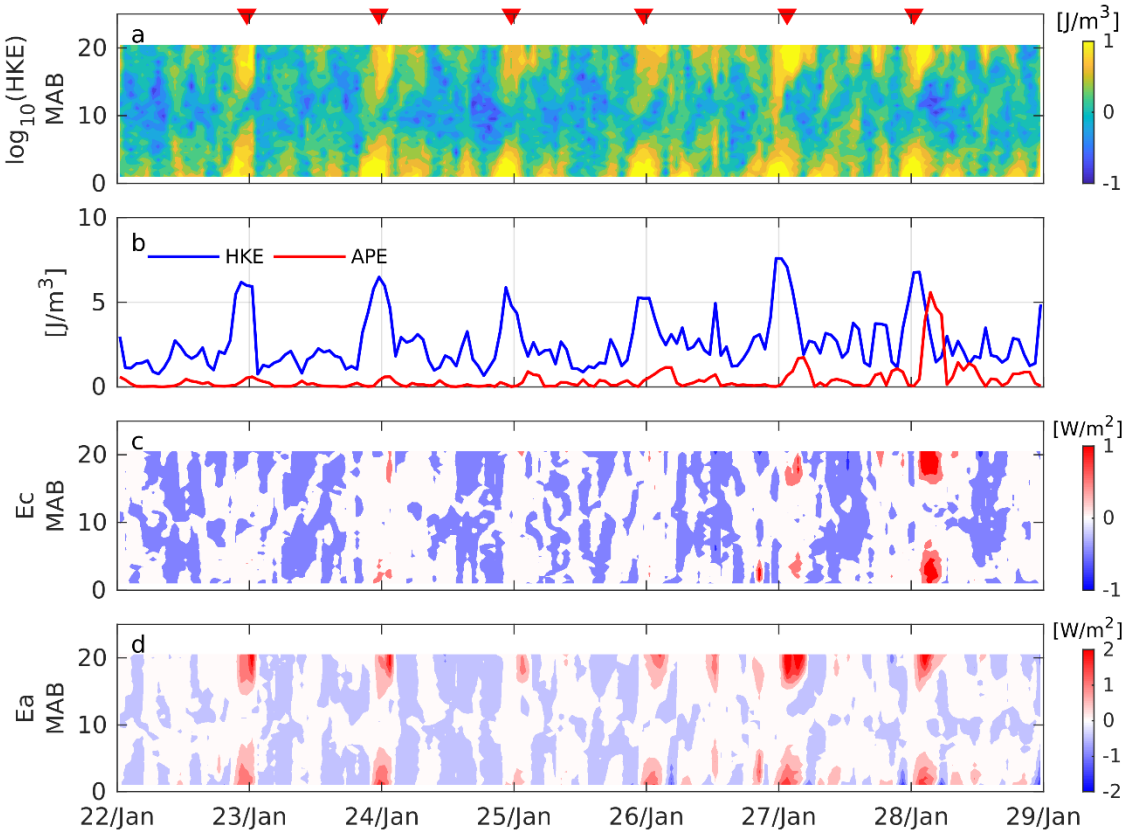

Figure 4.3 (a) HKE contours, (b) depth-averaged HKE and APE, (c) cross-shore baroclinic energy flux, (d) along-shore baroclinic energy flux. Red inverted triangles on top of (a) denote the occurrence of strong baroclinic tides.

4.3.2. Energetics and turbulent mixing

HKE was on the order of 10^{-1} to 10 J/m^3 in the mooring site (Figure 4.3 a). During the study period, the peak HKE occurred near the surface and bottom; while the minimum HKE occurred at 10 MAB (blue line in Figure 4.4 a). Corresponding to the baroclinic velocities (Figure 4.1 e), daily occurrence of strong HKE was observed (denoted by the red inverted triangles on top of Figure 4.3 a). During the strong baroclinic tides, the maximum value of HKE (~18 J/m^3) occurred at 1 MAB (red line in Figure 4.4 a). The mean APE was 0.4 J/m^3 during the study period (Figure 4.3 b). Corresponding to ζ (Figure 4.1 b), APE reached the maximum value of ~5 J/m^3 in the early morning of 28 January, 2013. Daily peaks of APE was observed in the mooring site, lagging behind HKE by ~3 hours (Figure 4.3 b).

Along-shore baroclinic energy flux (E_a) ranged from -2 to 2 W/m^2 (Figure 4.3 d), double the range (-1 to 1 W/m^2) of cross-shore baroclinic energy flux (E_c, see Figure 4.3 c). The large amplitude of E_a suggested a general along-shore propagation of baroclinic tides in the mooring site. During the study period, the mean E_c and E_a were almost zero within the entire water column (blue lines in Figure 4.4 b, c). Corresponding to U_a' (Figure 4.1 e), daily peaks in E_a were observed (Figure 4.3 d), lagging behind U_a' by ~3 hours. During the strong baroclinic tides, both E_c and E_a reached the minimum value of 0 W/m^2 in the middle of the water column at ~11 MAB (red lines in Figure 4.4 b, c). Offshore energy fluxes were observed within the entire water column, with the maximum value of ~0.5 W/m^2 at 20.5 MAB (red line in Figure 4.4 b). Positive along-

shore (northwest) energy fluxes were associated with the strong baroclinic tides, with the maximum of ~1.2 W/m^2 at 20.5 MAB (red line in Figure 4.4 c).

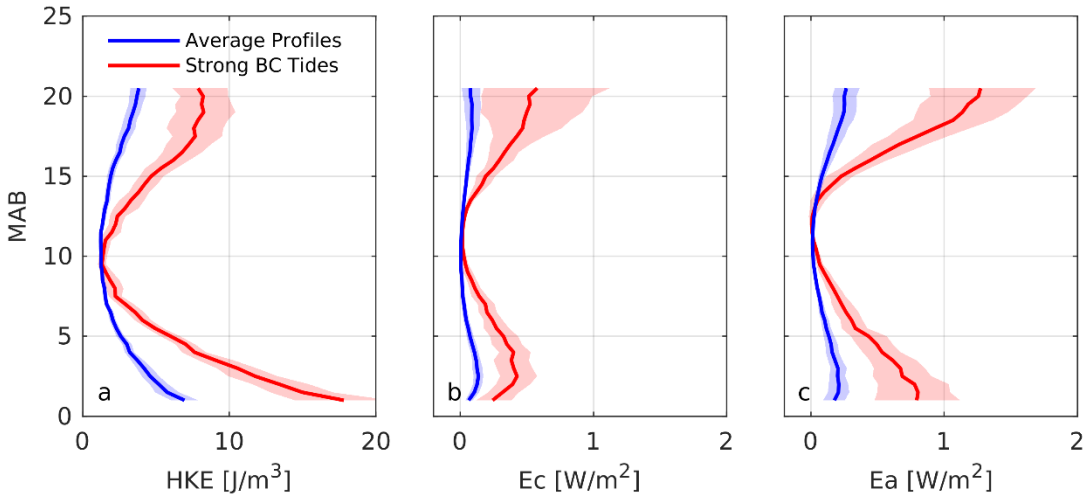

Figure 4.4 Depth profiles of (a) HKE, (b) cross-shore energy flux, (c) along-shore energy flux. Blue lines are the profiles averaged over the study period between 22–29 January, 2013. Red lines are the profiles averaged over the strong baroclinic tides. The occurrence of strong baroclinic tides is denoted by the red inverted triangles on top of Figure 4.3 a. Each triangle stands for 3 hrs. Shaded areas denote the 95 % bootstrap confidence intervals.

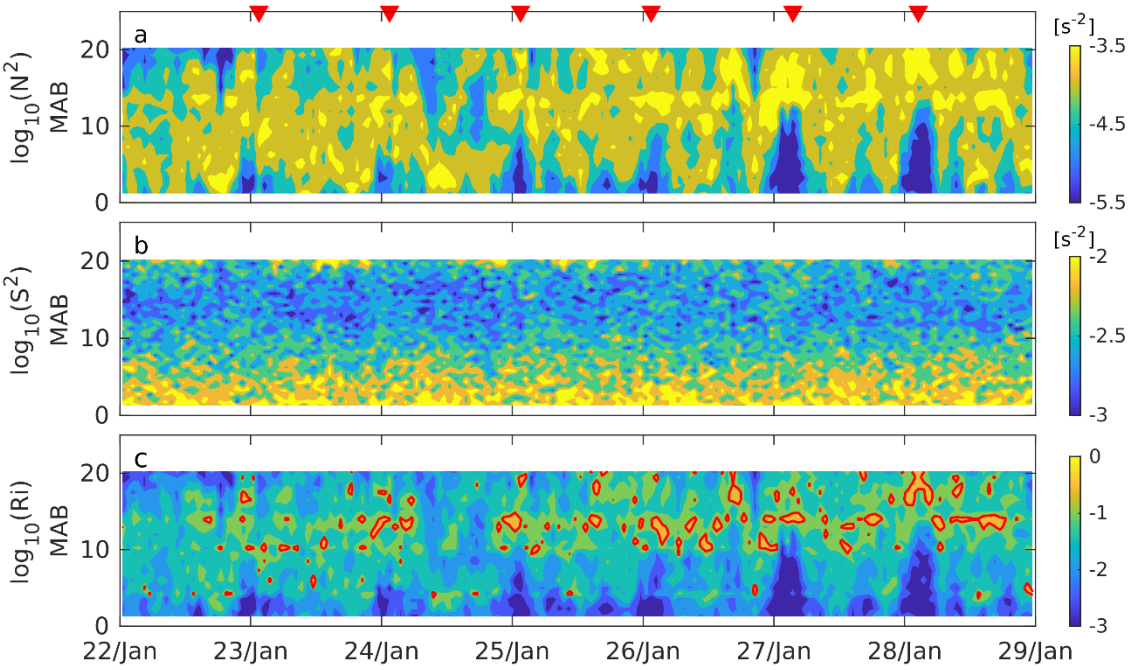

Figure 4.5 Contour plots of (a) buoyancy frequency squared, (b) velocity shear squared, (c) gradient Richardson number. Red inverted triangles on top of (a) denote the occurrence of strong baroclinic tides. Red contours in (c) denote gradient Richardson number of 0.25.

N^2 was on the order of ~10^{-6} to ~10^{-4} s^{-2} in the mooring site, with weakly stratified water (N^2 ~10^{-6} s^{-2}) mainly near the bottom (Figure 4.5 a). Vertical oscillations of the stratified water (N^2 ~10^{-4} s^{-2}) were observed within the entire water column. During the study periods, the maximum N^2 of 3x10^{-4} s^{-2} occurred at 14 MAB, suggesting the location of pycnocline (blue line in Figure 4.6 a). Decreases in N^2 near the bottom were observed daily (denoted by the red inverted triangles on top of Figure 4.5 a), associated with the strong baroclinic tides (Figure 4.1 e). Cross-correlation shows a 2-hour delay

between the increases in U_a' and the decreases in N^2 near the bottom. On average, the strong baroclinic tides resulted in a decrease in near bottom N^2 by one order of magnitude, from ~10^{-4} to ~10^{-5} s^{-2} (Figure 4.6 a).

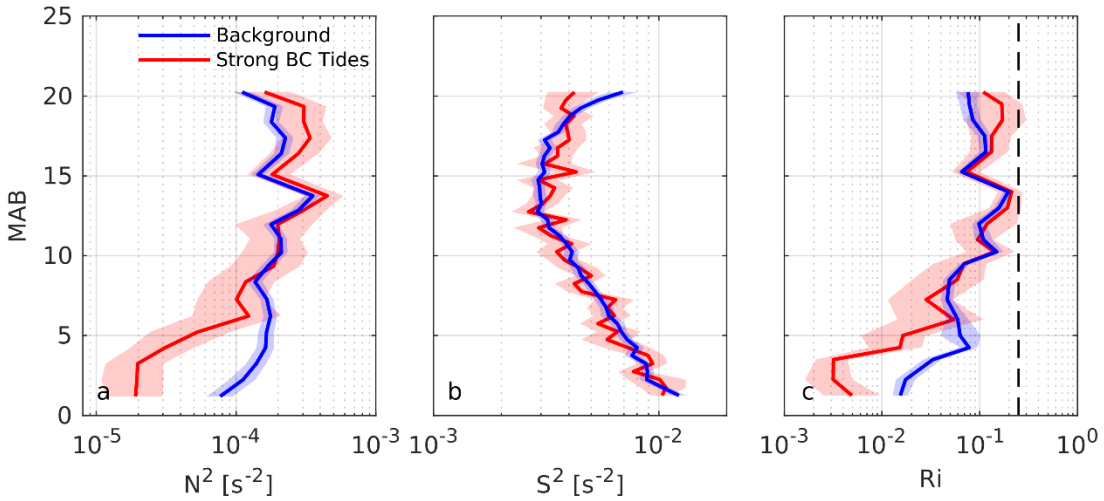

Figure 4.6 Depth profiles of (a) buoyancy frequency squared, (b) velocity shear squared, (c) gradient Richardson number. Blue lines are the profiles averaged over the study period between 22–29 January, 2013. Red lines are the profiles averaged over the strong baroclinic tides. The occurrence of strong baroclinic tides is denoted by the red inverted triangles on top of Figure 4.5 a. Black dashed line in (c) denotes gradient Richardson number of 0.25. Shaded areas are the 95 % bootstrap confidence intervals.

S^2 was one or two orders of magnitude larger than N^2, ranging from ~10^{-3} to ~10^{-2} s^{-2} (Figure 4.5 b). Averages over the study period and the strong baroclinic tides show similar vertical profiles of S^2, with the minimum and the maximum values occurring at

14 and 1 MAB, respectively (Figure 4.6 b). Stable conditions (Ri > 0.25) were occasionally observed in the mooring site, mostly in the upper half of the water column (Figure 4.5 c). Averages over the study periods show Ri was smaller than 0.25 within the entire water column (blue line in Figure 4.6 c), suggesting flow instability. During the strong baroclinic tides, Ri near the bottom decreased from ~10^{-2} to ~10^{-3} (Figure 4.6 c).

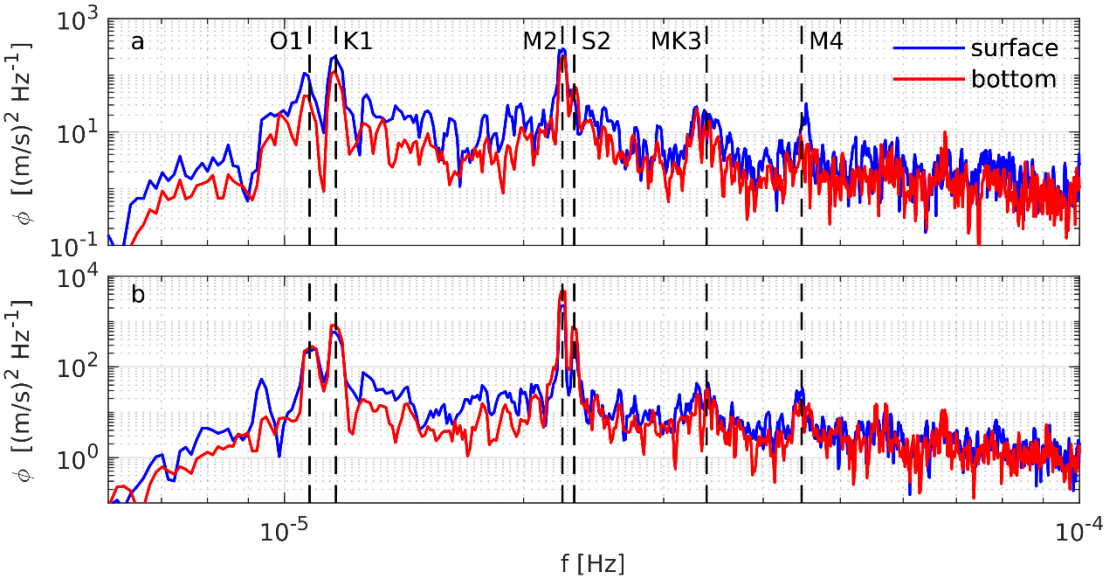

Figure 4.7 Power spectra density of (a) cross-shore baroclinic velocities and (b) along-shore baroclinic velocities near the surface (blue line) and near the bottom (red line). Near surface baroclinic velocities were averaged over 16.5 to 20.5 MAB. Near bottom baroclinic velocities were averaged over 1 to 5 MAB. Black dashed lines denote the frequency of tidal constituents. From left to right, O1 (25.82 hr), K1 (23.93 hr), M2 (12.42 hr), S2 (12.00 hr), MK3 (8.18 hr), and M4 (6.21 hr).

4.4. Discussion and conclusions

In this study, we characterize the dynamics of baroclinic tides in the NAG using observational data. Analysis on the measured current velocity is discussed in the next subsection.

4.4.1. Baroclinic currents

During the study period from 22-29 January, 2013, the mean baroclinic current speed (0.1 m/s) are comparable to the mean barotropic current speed of 0.2 m/s. This appears to be consistent with the results reported by Garrett and Kunze (2007). Peak baroclinic velocities were observed near the surface and bottom. During the deployment from 19 January to 19 April, 2013, power spectra show the baroclinic current energy mainly concentrated on four tidal frequencies (O1, K1, M2, S2), with small energy peaks at MK3 and M4 tidal frequency (Figure 4.7). For near surface baroclinic velocity (averaged over 16.5-20.5 MAB) and near bottom baroclinic velocity (averaged over 1-5 MAB), harmonic analysis shows the four major tidal constituents (O1, K1, M2, S2) accounted for 88 % and 94 % of baroclinic tidal energy, respectively. Relative contributions of the four major tidal constituents on baroclinic tides are summarized in Table 4.1. We then estimated tidal ellipses for the most significant semi-diurnal and diurnal tidal constituents (M2 and K1) to study the vertical structures of horizontal currents.

Table 4.1 Relative contributions of the four principal tidal constituents on baroclinic and barotropic tidal current energy (for details, see Codiga, 2011). The four major tidal constituents (O1, K1, M2, S2) accounted for 88 % of baroclinic tidal energy near the surface, 94 % of baroclinic tidal energy near the bottom, and 97 % of barotropic tidal energy.

Tidal constituents	Period (hr)	Fractions of baroclinic tidal energy near the surface (%)	Fractions of baroclinic tidal energy near the bottom (%)	Fractions of barotropic tidal energy (%)
M2	12.42	55.55	63.99	75.36
S2	12.00	7.84	9.78	13.20
K1	23.93	16.36	14.19	6.40
O1	25.82	8.59	5.81	2.25

The M2 and K1 baroclinic tidal ellipses (blue ellipses in Figure 4.8) showed similar vertical structures. For both the M2 and the K1 tides, the major axis of the tidal ellipses reached the minimum in the middle of the water column at ~11 MAB, and increased gradually towards the surface and bottom. Near bottom tidal ellipses were almost rectilinear. At 1 MAB, the major axis of the M2 and the K1 tidal ellipses reached the maximum value of 0.1 and 0.04 m/s, respectively. In the upper half of the water column (10-20 MAB), similar initial phases (denoted by straight lines in Figure 4.8) were observed between the barotropic and the baroclinie tides, while in the lower half of the water column (1-10 MAB), the initial phases of the barotropic and the baroclinic tides were almost 180° out of phase. Such baroclinic velocity structures were also reported by

Cao et al. (2015) in the northern South China Sea and by Eich et al. (2004) in the Mamala Bay, Hawaii.

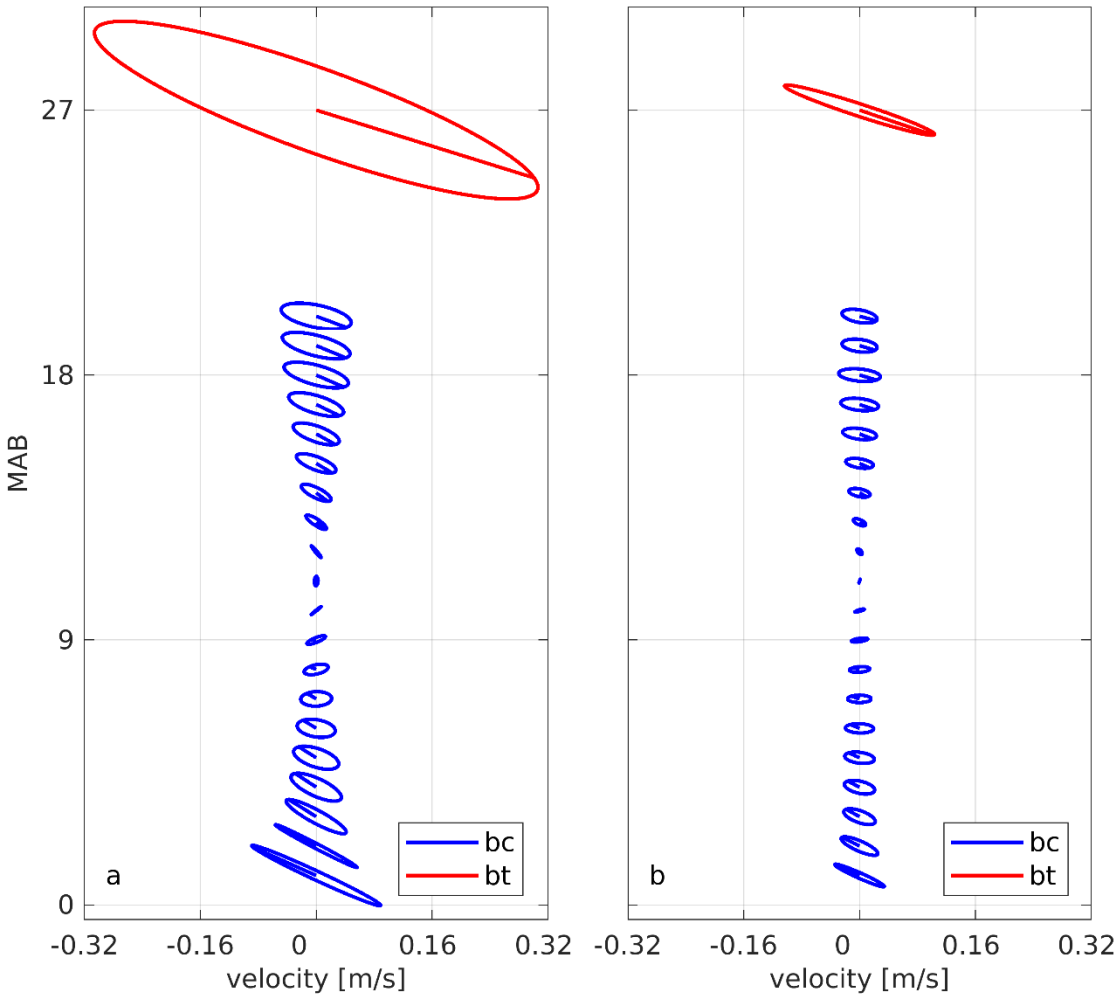

Figure 4.8 Barotropic (red) and baroclinic (blue) tidal eclipses for the M2 tide (a) and the K1 tide (b). Straight lines denote the initial phase of tidal ellipses.

The M2 tides were stronger than the K1 tides in both barotropic and baroclinic currents. The major axis of the M2 barotropic tide is 0.3 m/s, triple the value of 0.1 m/s for the K1 tide. Harmonic analysis on the 3-month velocity measurements shows the M2 tides accounted for 75.4 % of barotropic tidal energy, ten times larger than the contributions (6.4 %) for the K1 tides (Table 4.1). For baroclinic tides, the major axis of the M2 tidal ellipses were larger than that of the K1 tidal ellipses over the entire water water column (Figure 4.8). Harmonic analysis shows the energy fraction of the M2 tides was two or three times larger than the contributions of the K1 tides (Table 4.1).

4.4.2. Implications of baroclinic tides on the ecosystem

It is expected that physical processes associated with the baroclinic tides (e.g. isotherm displacements, turbulent mixing) are likely to affect marine ecosystem. During the study period from 22–29 January, 2013, the maximum ζ induced by baroclinic tides were ~8 m, 30 % of the nominal water depth of 27 m in the mooring site. Such oscillations seem to have impacts on the vertical distributions of chemical parameters in the ocean. Based on the measurements in the northern South China Sea, Pai et al. (2016) reported a close match between oxygen concentrations and isotherm displacements due to baroclinic tides.

Baroclinic tides are important energy source for turbulent mixing in the continental shelf (Steele et al. 2009). During the study periods, the mean Ri was smaller than 0.25 in the entire water column, implying flow instability. Turbulent mixing associated with the baroclinic tides appears to impact phytoplankton communities and fish activities, as

suggested by Sharples et al. (2009). In addition to biological effects, baroclinic tides seem to be an important mechanism for sediment transport in the bottom boundary layer (Heathershaw et al., 1987), or even determining the shape of continental shelf (Cacchione et al., 2002). Thus, it would be interesting to further examine the ecological response of the NAG to baroclinic tides.

5. CONCLUSIONS

In this dissertation, we examined the hydrodynamics induced by winter Shamals (chapter 2), tides (chapter 3), and baroclinic tides (chapter 4) based on field measurements in the NAG. The major findings of each study are summarized below.

In Chapter 2, we characterized the variabilities of surface meteorological and oceanographic parameters in the NAG during winter Shamals. Averages over the four encountered winter Shamals show an increase in surface wind stress from 0.03 to 0.15 N/m^2, and a decrease in humidity from 65.0 to 52.2 %. Based on examination of individual heat flux components, the latent heat flux shows the largest variability, from 56.8 to 188.1 W/m^2. The changes in surface meteorological conditions during winter Shamals were found to influence hydrodynamics in the NAG, as exemplified by an average increase in surface wave height from 0.58 to 0.82 m, an increase in surface wave period from 3.6 to 4.2 s, and a triple increase in TKE dissipation rate from $3.6x10^{-7}$ to $1.1x10^{-6}$ W/kg. In this study, we applied three parameterization methods for TKE dissipation rates based on breaking surface wave, wind shear layer, and convections. During steady Shamal winds periods (occurrence of steady wind stress and heat loss), the parametrized TKE dissipation rates based on surface wave breaking, wind shear production, and surface buoyancy flux were approximately 85 %, 41 % and 14 % of the measured TKE dissipation rates, respectively. This suggests mixing during winter Shamals events, at least in our case (~9 m beneath the surface), was induced mainly by breaking surface wave and wind stress.

In Chapter 3, we examined the variabilities of current velocities and turbulent mixing in the NAG based on field experiments. Measurements during 14-28 July 2017 show that vertical velocities near the bottom were primarily induced by tides, with downwelling (upwelling) occurring during flood (ebb) tides. Analysis of velocity profiles shows positive vertical velocity gradient during ebb tides, indicating horizontal convergence. TKE dissipation rates show quarter-diurnal patterns at the bottom, corresponding to the semi-diurnal tidal currents. Turbulent diffusivity (K_ρ) and gradient Richardson number (Ri) were well-correlated near the bottom, with a correlation coefficient of -0.87. Here we parametrized K_ρ as a function of Ri using the power function forms introduced by Peters et al. (1988), expressed as $K_\rho = 10^{-5} Ri^{-1\pm0.03}$. Averages over the neap tides (16-19 July, 2017) and the spring tides (23-26 July, 2017) show that the horizontal and vertical speeds increased from 0.18 to 0.26 m/s and from 2.7 to 3.8 mm/s, respectively. Stronger near bottom turbulent mixing was observed during the spring tides than the neap tides, as exemplified by the increase in TKE dissipation rates from $2.2\text{x}10^{-7}$ to $5.6\text{x}10^{-7}$ W/kg, and the decrease in buoyancy frequency squared from $2.1\text{x}10^{-5}$ to $5.5\text{x}10^{-6}$ s^{-2}.

In Chapter 4, we investigated the dynamics of baroclinic tides in the NAG based on observational data. Measurements between 22-29 January, 2013 show: (1) isopycnal displacements in the interior of the water column, with a maximum of up to 8 m; (2) higher variabilities and amplitudes in the along-shore baroclinic currents than in the cross-shore baroclinic currents, implying approximate along-shore propagations of baroclinic tides; (3) a 3-hour delay between along-shore baroclinic velocity and pressure

anomaly driven by the baroclinic tides; (4) horizontal kinematic energy of the baroclinic tides reached peak values near the surface and bottom, with a minimum value occurring at ~11 meter above the bottom; (5) the average gradient Richardson number was less than 0.25 in the whole water column, implying shear instability. Further data analysis of measured current velocity shows that the baroclinic tidal currents were mainly governed by four tidal constituents (M2, S2, K1, and O1), with M2 and K1 being the most significant semi-diurnal and diurnal tidal constituents.

REFERENCES

Abarbanel, H. D., Holm, D. D., Marsden, J. E., & Ratiu, T. (1984). Richardson number criterion for the nonlinear stability of three-dimensional stratified flow. *Physical Review Letters*, 52(26), 2352.

Abdi Vishkaee, F., Flamant, C. Cuesta, J. Flamant, & Khalesifard, H. R. (2011), Multiplatform observations of dust vertical distribution during transport over northwest Iran in the summertime, *Journal of Geophysical Research: Atmospheres*, 116(D5).

Abdi Vishkaee, F., Flamant, C., Cuesta, J., Oolman, L., Flamant, P., & Khalesifard, H. R. (2012). Dust transport over Iraq and northwest Iran associated with winter Shamal: A case study. *Journal of Geophysical Research: Atmospheres*, 117(D3).

Aboobacker, V. M., Vethamony, P., & Rashmi, R. (2011). "Shamal" swells in the Arabian sea and their influence along the west coast of India. *Geophysical Research Letters*, 38(3).

Almazroui, M., Nazrul Islam, M., Athar, H., Jones, P. D., & Rahman, M. A. (2012). Recent climate change in the Arabian Peninsula: annual rainfall and temperature analysis of Saudi Arabia for 1978–2009. *International Journal of Climatology*, 32(6), 953-966.

Al-Muzaini, S., & Jacob, P. G. (1996). Marine plants of the arabian gulf. *Environment International*, 22(3), 369-376.

Al Senafi, F., & Anis, A. (2015). Shamals and climate variability in the northern Arabian/Persian Gulf from 1973 to 2012. *International Journal of Climatology*, 35(15), 4509-4528.

Anis, A., & Moum, J. N. (1992). The superadiabatic surface layer of the ocean during convection. *Journal of Physical Oceanography*, 22(10), 1221-1227.

Anis, A., & Singhal, G. (2006). Mixing in the surface boundary layer of a tropical freshwater reservoir. *Journal of Marine Systems*, 63(3), 225-243.

Azizpour, J., Siadatmousavi, S. M., & Chegini, V. (2016). Measurement of tidal and residual currents in the Strait of Hormuz. *Estuarine, Coastal and Shelf Science*, 178, 101-109.

Cacchione, D. A., Pratson, L. F., & Ogston, A. S. (2002). The shaping of continental slopes by internal tides. *Science*, 296(5568), 724-727.

Cao, A. Z., Li, B. T., & Lv, X. Q. (2015). Extraction of internal tidal currents and reconstruction of full-depth tidal currents from mooring observations. *Journal of Atmospheric and Oceanic Technology*, 32(7), 1414-1424.

Cavalcante, G. H., Feary, D. A., & Burt, J. A. (2016). The influence of extreme winds on coastal oceanography and its implications for coral population connectivity in the southern Arabian Gulf. *Marine Pollution Bulletin*, 105(2), 489-497.

Chao, S.-Y., Kao, T. W., & Al-Hajri, K. R. (1992). A numerical investigation of circulation in the Arabian Gulf. *Journal of Geophysical Research: Oceans*, 97(C7), 11219-11236.

Cheng, Z., & Mitsuyasu, H. (1992). Laboratory studies on the surface drift current induced by wind and swell. *Journal of Fluid Mechanics*, 243, 247-259.

Chriss, T. M., & Caldwell, D. R. (1982). Evidence for the influence of form drag on bottom boundary layer flow. *Journal of Geophysical Research: Oceans*, 87(C6), 4148-4154.

Codiga, D.L., 2011. Unified tidal analysis and prediction using the UTide Matlab functions. *Technical Report 2011-01*. Graduate School of Oceanography, University of Rhode Island, Narragansett, RI.

Dorrestein, R. (1979). On the vertical buoyancy flux below the sea surface as induced by atmospheric factors. *Journal of Physical Oceanography*, 9(1), 229-231.

Eich, M. L., Merrifield, M. A., & Alford, M. H. (2004). Structure and variability of semidiurnal internal tides in Mamala Bay, Hawaii. *Journal of Geophysical Research: Oceans*, 109(C5).

El-Sabh, M. I., & Murty, T. S. (1989). Storm surges in the Arabian Gulf. *Natural Hazards*, 1(4), 371-385.

Fairall, C. W., Bradley, E. F., Hare, J. E., Grachev, A. A., & Edson, J. B. (2003). Bulk parameterization of air–sea fluxes: updates and verification for the COARE algorithm. *Journal of Climate*, 16(4), 571-591.

Forryan, A., Martin, A. P., Srokosz, M. A., Popova, E. E., Painter, S. C., & Renner, A. H. (2013). A new observationally motivated Richardson number based mixing parametrization for oceanic mesoscale flow. *Journal of Geophysical Research: Oceans*, 118(3), 1405-1419.

Galperin, B., Sukoriansky, S., & Anderson, P. S. (2007). On the critical Richardson number in stably stratified turbulence. *Atmospheric Science Letters*, 8(3), 65-69.

Garrett, C., & Kunze, E. (2007). Internal tide generation in the deep ocean. *Annual Review of Fluid Mechanics*, 39, 57-87.

Gross, T. F., & Nowell, A. R. (1983). Mean flow and turbulence scaling in a tidal boundary layer. *Continental Shelf Research*, 2(2-3), 109-126.

Grubbs, F. E. (1969). Procedures for detecting outlying observations in samples. *Technometrics*, 11(1), 1-21.

Heathershaw, A. D., New, A. L., & Edwards, P. D. (1987). Internal tides and sediment transport at the shelf break in the Celtic Sea. *Continental Shelf Research*, 7(5), 485-517.

Howard, L. N. (1961). Note on a paper of John W. Miles. *Journal of Fluid Mechanics*, 10(4), 509-512.

Hsu, C. T., Wu, H. Y., Hsu, E. Y., & Street, R. L. (1982). Momentum and energy transfer in wind generation of waves. *Journal of Physical Oceanography*, 12(9), 929-951.

Huang, R. X., & Jin, X. (2006). Gravitational potential energy balance for the thermal circulation in a model ocean. *Journal of Physical Oceanography*, 36(7), 1420-1429.

Husar, R. B., Prospero, J. M., & Stowe, L. L. (1997). Characterization of tropospheric aerosols over the oceans with the NOAA advanced very high resolution radiometer

optical thickness operational product. *Journal of Geophysical Research: Atmospheres*, 102(D14), 16889-16909.

John, V. C. (1992). Harmonic tidal current constituents of the western Arabian Gulf from moored current measurements. *Coastal engineering*, 17(1-2), 145-151.

Kang, D., & Fringer, O. (2012). Energetics of barotropic and baroclinic tides in the Monterey Bay area. *Journal of Physical Oceanography*, 42(2), 272-290.

Kelly, S. M., & Nash, J. D. (2010). Internal-tide generation and destruction by shoaling internal tides. *Geophysical Research Letters*, 37(23).

Kolmogorov, A. N. (1968). Local structure of turbulence in an incompressible viscous fluid at very high Reynolds numbers. *Physics-Uspekhi*, 10(6), 734-746.

Lalli, C., & Parsons, T. R. (1993). *Biological oceanography: an introduction*. Oxford: Pergamon Press.

Large, W. G., McWilliams, J. C., & Doney, S. C. (1994). Oceanic vertical mixing: A review and a model with a nonlocal boundary layer parameterization. *Reviews of Geophysics*, 32(4), 363-403.

Leichter, J. J., Stewart, H. L., & Miller, S. L. (2003). Episodic nutrient transport to Florida coral reefs. *Limnology and Oceanography*, 48(4), 1394-1407.

Li, M., & Zhong, L. (2009). Flood–ebb and spring–neap variations of mixing, stratification and circulation in Chesapeake Bay. *Continental Shelf Research*, 29(1), 4-14.

Lien, R.-C., & D'Asaro, E. A. (2006). Measurement of turbulent kinetic energy dissipation rate with a Lagrangian float. *Journal of Atmospheric and Oceanic Technology*, 23(7), 964-976.

MacCready, P., & Geyer, W. R. (2010). Advances in estuarine physics. *Annual Review of Marine Science*, 2, 35-58.

Marcella, M. P., & Eltahir, E. A. B. (2008). The hydroclimatology of Kuwait: Explaining the variability of rainfall at seasonal and interannual time scales. *Journal of Hydrometeorology*, 9(5), 1095-1105.

Miles, J. W. (1961). On the stability of heterogeneous shear flows. *Journal of Fluid Mechanics*, 10(4), 496-508.

Moradi, M., & Kabiri, K. (2012). Red tide detection in the Strait of Hormuz (east of the Persian Gulf) using MODIS fluorescence data. *International Journal of Remote Sensing*, 33(4), 1015-1028.

Munk, W., & Wunsch, C. (1998). Abyssal recipes II: Energetics of tidal and wind mixing. *Deep Sea Research Part I: Oceanographic Research Papers*, 45(12), 1977-2010.

Nash, J. D., Alford, M. H., & Kunze, E. (2005). Estimating internal wave energy fluxes in the ocean. *Journal of Atmospheric and Oceanic Technology*, 22(10), 1551-1570.

Nash, J. D., Kelly, S. M., Shroyer, E. L., Moum, J. N., & Duda, T. F. (2012). The unpredictable nature of internal tides on continental shelves. *Journal of Physical Oceanography*, 42(11), 1981-2000.

Nash, J. D., Kunze, E., Lee, C. M., & Sanford, T. B. (2006). Structure of the baroclinic tide generated at Kaena Ridge, Hawaii. *Journal of Physical Oceanography*, 36(6), 1123-1135.

Neelamani, S., Al-Salem, K., & Rakha, K. (2007). Extreme waves for Kuwaiti territorial waters. *Ocean Engineering*, 34(10), 1496-1504.

Nezlin, N. P., Polikarpov, I. G., Al-Yamani, F. Y., Subba Rao, D. V., & Ignatov, A. M. (2010). Satellite monitoring of climatic factors regulating phytoplankton variability in the Arabian (Persian) Gulf. *Journal of Marine Systems*, 82(1), 47-60.

Osborn, T. R. (1980). Estimates of the local rate of vertical diffusion from dissipation measurements. *Journal of Physical Oceanography*, 10(1), 83-89.

Pai, S. C., Wei, C. L., Lin, S., Wen, L. S., & Tseng, C. M. (2016). Observation of internal tide-induced nutrient upwelling in Hungtsai Trough, a submarine canyon in the northern South China Sea. *Continental Shelf Research*, 120, 59-67.

Peters, H., Gregg, M. C., & Toole, J. M. (1988). On the parameterization of equatorial turbulence. *Journal of Geophysical Research: Oceans*, 93(C2), 1199-1218.

Pond, S., & Pickard, G. L. (1983). *Introductory dynamical oceanography*. Oxford: Pergamon Press.

Privett, D. W. (1959). Monthly charts of evaporation from the N. Indian Ocean (including the Red Sea and the Persian Gulf). *Quarterly Journal of the Royal Meteorological Society*, 85(366), 424-428.

Proctor, R., Flather, R. A., & Elliott, A. J. (1994). Modelling tides and surface drift in the Arabian Gulf—application to the Gulf oil spill. *Continental Shelf Research*, 14(5), 531-545.

Rao, P. G., Hatwar, H. R., Al-Sulaiti, M. H., & Al-Mulla, A. H. (2003). Summer shamals over the Arabian Gulf. *Weather*, 58(12), 471-478.

Rayson, M. D., Ivey, G. N., Jones, N. L., Meuleners, M. J., & Wake, G. W. (2011). Internal tide dynamics in a topographically complex region: Browse Basin, Australian North West Shelf. *Journal of Geophysical Research: Oceans*, 116(C1).

Reynolds, R. M. (1993). Physical oceanography of the Gulf, Strait of Hormuz, and the Gulf of Oman—results from the Mt Mitchell expedition. *Marine Pollution Bulletin*, 27, 35-59.

Richlen, M. L., Morton, S. L., Jamali, E. A., Rajan, A., & Anderson, D. M. (2010). The catastrophic 2008–2009 red tide in the Arabian gulf region, with observations on the identification and phylogeny of the fish-killing dinoflagellate cochlodinium polykrikoides. *Harmful Algae*, 9(2), 163-172.

Rippeth, T. P., Fisher, N. R., & Simpson, J. H. (2001). The cycle of turbulent dissipation in the presence of tidal straining. *Journal of Physical Oceanography*, 31(8), 2458-2471.

Rosner, B. (1983). Percentage points for a generalized ESD many-outlier procedure. *Technometrics*, 25(2), 165-172.

Sato, M., Klymak, J. M., Kunze, E., Dewey, R., & Dower, J. F. (2014). Turbulence and internal waves in Patricia Bay, Saanich Inlet, British Columbia. *Continental Shelf Research*, 85, 153-167.

Schneider, T. (2001). Analysis of incomplete climate data: estimation of mean values and covariance matrices and imputation of missing values. *Journal of Climate*, 14(5), 853-871.

Scully, M. E., & Friedrichs, C. T. (2007). Sediment pumping by tidal asymmetry in a partially mixed estuary. *Journal of Geophysical Research: Oceans*, 112(C7).

Shao, H. J., Tseng, R. S., Lien, R. C., Chang, Y. C., & Chen, J. M. (2018). Turbulent mixing on sloping bottom of an energetic tidal channel. *Continental Shelf Research*, 166, 44-53.

Sharples, J. (2007). Potential impacts of the spring-neap tidal cycle on shelf sea primary production. *Journal of Plankton Research*, 30(2), 183-197.

Sharples, J., Moore, C. M., Hickman, A. E., Holligan, P. M., Tweddle, J. F., Palmer, M. R., & Simpson, J. H. (2009). Internal tidal mixing as a control on continental margin ecosystems. *Geophysical Research Letters*, 36(23).

Sharples, J., Moore, M. C., Rippeth, T. P., Holligan, P. M., Hydes, D. J., Fisher, N. R., & Simpson, J. H. (2001). Phytoplankton distribution and survival in the thermocline. *Limnology and Oceanography*, 46(3), 486-496.

Sheppard, C. R. (1993). Physical environment of the Gulf relevant to marine pollution: an overview. *Marine Pollution Bulletin*, 27, 3-8.

Shi, W., Wang, M., & Jiang, L. (2011). Spring-neap tidal effects on satellite ocean color observations in the Bohai Sea, Yellow Sea, and East China Sea. *Journal of Geophysical Research: Oceans*, 116(C12).

Shih, L. H., Koseff, J. R., Ivey, G. N., & Ferziger, J. H. (2005). Parameterization of turbulent fluxes and scales using homogeneous sheared stably stratified turbulence simulations. *Journal of Fluid Mechanics*, 525, 193-214.

Shroyer, E. L., Moum, J. N., & Nash, J. D. (2010). Energy transformations and dissipation of nonlinear internal waves over New Jersey's continental shelf. *Nonlinear processes in Geophysics*, 17(4), 345-360.

Simpson, J. H., & Sharples, J. (2012). *Introduction to the physical and biological oceanography of shelf seas.* Cambridge: Cambridge University Press.

Steele, J. H., Thorpe, S. A., & Turekian, K. K. (2009). Elements of physical oceanography: a derivative of the encyclopedia of ocean sciences. San Diego: Academic Press.

Swift, S. A., & Bower, A. S. (2003). Formation and circulation of dense water in the Persian/Arabian Gulf. *Journal of Geophysical Research: Oceans*, 108(C1), 4-1.

Taylor, G.I., 1919. Tidal friction in the Irish Sea. *Philosophical Transactions of the Royal Society of London*, 230, 1-93.

Terray, E. A., Donelan, M. A., Agrawal, Y. C., Drennan, W. M., Kahma, K. K., Williams, A. J., ... & Kitaigorodskii, S. A. (1996). Estimates of kinetic energy dissipation under breaking waves. *Journal of Physical Oceanography*, 26(5), 792-807.

Thomson, D. J. (1982). Spectrum estimation and harmonic analysis. *Proceedings of the IEEE*, 70(9), 1055-1096.

Thoppil, P. G., & Hogan, P. J. (2010). Persian Gulf response to a wintertime shamal wind event. *Deep Sea Research Part I: Oceanographic Research Papers*, 57(8), 946-955.

Thorpe, S. A. (2007). *An introduction to ocean turbulence*. Cambridge: Cambridge University Press.

Trowbridge, J., & Elgar, S. (2001). Turbulence measurements in the surf zone. *Journal of Physical Oceanography*, 31(8), 2403-2417.

Vinod Kumar, K., Seemanth, M., Vethamony, P., & Aboobacker, V. M. (2014). On the spatial structure and time evolution of shamal winds over the Arabian Sea – a case study through numerical modelling. *International Journal of Climatology*, 34(6), 2122-2128.

Webb, A. J., & Pond, S. (1986). A modal decomposition of the internal tide in a deep, strongly stratified inlet: Knight Inlet, British Columbia. *Journal of Geophysical Research: Oceans*, 91(C8), 9721-9738.

Weisberg, R. H., Halpern, D., Tang, T. Y., & Hwang, S. M. (1987). M2 tidal currents in the eastern equatorial Pacific Ocean. *Journal of Geophysical Research: Oceans*, 92(C4), 3821-3826.

Woodson, C. B. (2018). The fate and impact of internal waves in nearshore ecosystems. *Annual Review of Marine Science*, 10, 421-441.

Wu, J. (1983). Sea-surface drift currents induced by wind and waves. *Journal of Physical Oceanography*, 13(8), 1441-1451.

Zhao, J., & Ghedira, H. (2014). Monitoring red tide with satellite imagery and numerical models: A case study in the Arabian Gulf. *Marine Pollution Bulletin*, 79(1), 305-313.

Zhao, J., Temimi, M., Al Azhar, M., & Ghedira, H. (2015). Satellite-based tracking of oil pollution in the Arabian Gulf and the sea of Oman. *Canadian Journal of Remote Sensing*, 41(2), 113-125.